

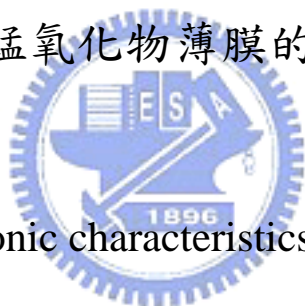
國立交通大學

電子物理系

博士論文

基板穩定之六方與正交結構

多鐵性稀土元素錳氧化物薄膜的磁與電子特性研究



Magnetic and electronic characteristics of substrate-stabilized

hexagonal and orthorhombic structured

multiferroic rare earth manganese oxide thin films

研究生：謝志昌

指導教授：莊振益 教授

中華民國九十七年七月

基板穩定之六方與正交結構

多鐵性稀土元素錳氧化物薄膜的磁與電子特性研究

Magnetic and electronic characteristics of substrate-stabilized

hexagonal and orthorhombic structured

multiferroic rare earth manganese oxide thin films

研究生：謝志昌

Student : Chih-Chang Hsieh

指導教授：莊振益教授

Advisor : Prof. Jenh-Yih Juang

國立交通大學



A Dissertation

Submitted to Department of Electrophysics

College of Science

National Chiao Tung University

in Partial Fulfillment of the Requirements

for the Degree of

Doctor of Philosophy

in

Electrophysics

July 2008

Hsinchu, Taiwan, Republic of China

中華民國九十七年七月

六方與正交結構多鐵性稀土元素錳氧化物薄膜 之磁性與電子結構特性研究

研究生：謝志昌

指導教授：莊振益教授

國立交通大學

電子物理系



本論文將介紹如何分別製備具有六方與正交結構之多鐵性稀土元素錳氧化物的粉末、靶材、與薄膜樣品。同時針對不同結構的樣品進行電子結構與磁性特徵的量測。

首先我們利用固態燒結法可以製備出具有六方結構的稀土元素錳氧化物（離子半徑較小之稀土元素），接著利用摻雜鈣離子或鋇離子取代稀土元素的方式，試圖直接從材料內部施加應力，以穩定其正交結構。我們發現藉由摻雜鈣超過 30%，就可以完成結構轉換。藉由摻雜造成了錳氧的結構從 MnO_5 轉換到 MnO_6 ，同時摻雜之後錳離子的價數從 +3 變成了 +3/+4 的混合價數。因為混合價數的雙交換機制，原本的反鐵磁特性被鐵磁性行為所取代。但是我們發現摻雜鋇離子並沒有造成類似的結構的轉變，而且造成了磁性特徵的消失。

我們同時利用外部施加應力的方式製備六方與正交結構的薄膜。六方結構的薄膜可以藉由 YSZ(111) 的基板製備或是其他具有表面三角形結構同時晶格常數又不會差異太大的基板。我們利用 X-ray 繞射儀探討脈衝雷射蒸鍍法製備的單一軸向六方結構鈮錳氧薄膜，我們可以看到薄膜具備六重對稱特性同時基板與薄膜的對稱性亦與我們的估計相符。

在另一方面正交結構的薄膜亦可利用選擇適當的匹配基板製備。經過預先的比較計算在這裡我們分別選擇了三種基板鈦酸鋇(110)、鋁酸鋇(110)、與鈦酸鋇(100)，我們可以在這三種基板上分別製備具有單一軸向的 a 軸、b 軸、與 c 軸薄膜。藉由 X-ray

繞射儀的判斷我們可以發現薄膜分別具備二重、二重、與四重對稱性。藉由這些判定我們可以了解薄膜的軸向性。同時我們發現 LAO(110) 是我們在探討這類薄膜時最佳的利器，因為可以利用此類基板製備出軸向分離的薄膜，對於我們探討這些軸向異性的材料具有相當大的幫助。我們可以在成長於鋁氧基板上的鈮錳氧與鈹錳氧薄膜看到反鐵磁相轉變溫度與第二次磁性相轉變。兩種材料在三個軸向上都可以看到反鐵磁的相轉變，但是第二次相轉變只會發生在 a 軸(只在鈮錳氧看到) 與 c 軸(鈮錳氧與鈹錳氧都可看到)。雖然他們的結構特徵非常的相近，但是在這一系列的化合物一點點的差異性就會改變錳氧間的鍵角與距離，也因為這些微的差異性造成材料間不同的性質。

最後我們利用線性偏振的同步輻射光譜探討不同結構間的軸向異性行為。在六方晶系與正交結構的鈮錳氧材料，錳光譜與氧光譜分別展現了 MnO_5 與 MnO_6 正三價電子結構的差異性。在氧光譜中可以清楚看出能階因晶場與姜-泰勒效應所造成的分裂：在六方結構中能階分裂為三個，在正交結構中分裂成四個。我們利用軸向異性的光譜特徵與磁電耦合的理論預測低溫可能造成的光譜變化行為。利用這些方法我們可以製備出一系列稀土元素錳氧化物薄膜，同時利用這些薄膜可以進行相關的量測確認磁電耦合的多鐵機制是否存在，並嘗試找出較明顯的磁電極化行為。

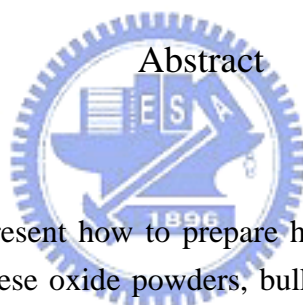


Magnetic and electronic characteristics of substrate-stabilized
hexagonal and orthorhombic structured
multiferroic rare earth manganese oxide thin films

Student: Chih-Chang Hsieh

Advisor: Prof. Jenh-Yih Juang

Department of Electrophysics
National Chiao Tung University



In this dissertation, we present how to prepare hexagonal and orthorhombic structured multiferroic rare earth manganese oxide powders, bulks, and thin films. We also probed the anisotropies in the magnetic behavior and electronic structure of these materials.

Firstly, we prepare hexagonal RMnO_3 (R: rare earth and Y) compounds with smaller rare earth ions. We tried to stabilize the orthorhombic structure by replacing the R-site ions with Ca^{2+} or Sr^{2+} . This method could provide inner strain force and the material from the thermodynamically stable hexagonal structure to orthorhombic perovskite structure. We find that the entire structure transforms into orthorhombic by doping Ca^{2+} up to 30%. In the doping process, the MnO_5 structure is no longer stable and starts to convert into MnO_6 structure, which in turn substantially modifies the magnetoelectric properties and electronic structures of the material. The trivalent manganese converts into +3/+4 mixed valence and induces the double exchange mechanism. Consequently, the antiferromagnetism is replaced by ferromagnetic interaction and revealed traditional spin glass behaviors. The Sr^{2+} doped sample remains as hexagonal structure and magnetic characteristic was significantly suppressed.

The external strain force originated from the epitaxial relation between the substrate and thin films during deposition can also serve as an excellent method in obtaining samples with

desired crystal structures. We calculated the in-plane mismatch and used the YSZ(111) substrate in preparing hexagonal thin films. The sample revealed six-fold symmetry and in-plane arrangement has corresponded nicely to our estimation.

On the other hand, we deposited thin film on SrTiO₃(110), LaAlO₃(110), and SrTiO₃(100) substrates and obtained a-, b-, and c-axis thin film of orthorhombic structure. With the X-ray diffraction characterizations, we see the thin films are having 2-fold, 2-fold, and 4-fold symmetry, depending on the substrate chosen. In particular, we find that the *a*-axis and *b*-axis films are having distinguishable crystalline axis, while there exists a twin growth behavior in the *c*-axis film. Owing to the relatively smaller in-plane mismatch, the LaAlO₃ (110) is proved to be the best substrate in stabilizing orthorhombic RMnO₃ for smaller ionic size of R. The films with specific growth directions allow us to directly probe the anisotropies existent in magnetism, polarization, and bonding relations. We observed the antiferromagnetic ordering and spin reordering transition in both YMnO₃ and HoMnO₃ thin films grown on LaAlO₃ (110) substrates. The antiferromagnetic ordering can be probed with applied field parallel to each crystallographic axis. However, the spin reordering was only observable for field applied parallel to a-axis (only observed in YMnO₃) and c-axis (observed in YMnO₃ and HoMnO₃). Although the crystal structure of these two films is nearly the same, RMnO₃ compound is sensitive to the Mn-O bonding distance and Mn-O-Mn bond angle, thus might explain the different behaviors exhibited by the two neighboring compounds.

Finally, we used the linear polarized x-ray to probe the anisotropic bonding relation in both of these two crystal structure. In the hexagonal and orthorhombic YMnO₃ thin films, Mn L edge and O K edge x-ray absorption spectra exhibited the MnO₅ and MnO₆ structure with trivalent manganese ions in respective crystal structure. We attribute the energy splitting in the O K edge spectra to the effect of crystal field and Jahn-Teller effect. There are three splitting energy levels in hexagonal structure and 4 splitting energy levels in orthorhombic structure. We also utilize the anisotropic spectra and the magnetoelectric theory in E-type magnetic orders to estimate the possible spectra in the lock-in state. By extending these methods, we should be able to prepare a series of rare earth manganese thin films that are potentially able to realize the magnetoelectric state expected in the E-type magnetic structure for more dramatic magnetism-induced polarizations.

致 謝

在漫長的研究生涯中完成了這本論文，在這裡要感謝固態實驗室的指導老師吳光雄教授、林俊源教授、溫增明教授、郭義雄教授的悉心指導使我在實驗研究及學術的探討上有更深一層的了解。更感謝我的指導老師莊振益教授，在我研究中遇到困難時認真的指導我正確的觀念，並導引並修正我的研究核心不至於走過多的冤妄路。

在實驗時與閒暇之餘，更要感謝實驗室夥伴們的幫助。實驗室學長：世溥、中裕、慧愷、旭禎、世烽、博瑛、小志在實驗上的指導，讓我對實驗的流程與儀器的架設更為了解；同學星哥、璨耀、維仁陪我度過煩悶的生活；同時也感謝許多學弟妹們宗漢、訓全、政義、家弘、家恬、珈芸、凱婷……等等在實驗事務上的幫忙。要感謝的人實在是太多了，讓我不免俗的說一聲感謝大家吧！有你們的陪伴讓我等生活更加的充實，在科學研究的生活中有充足的生活糧食與豐富的資源。

最後感謝家人所給予的支持與鼓勵，讓我感受到精神上的支持並得以完成學業。

Contents

Abstract (in Chinese)	i	
Abstract (in English)	iii	
Acknowledgement	v	
Contents	vi	
List of Tables	viii	
List of Figures	ix	
Chapter 1	Introduction	1
1.1	Introduction to multiferroics	1
1.2	Origin of the multiferroelectricity	2
1.3	Classification of multiferroics	4
1.4	Multiferroic RMnO_3	6
	1.4.1 Hexagonal phase	8
	1.4.2 Orthorhombic phase	10
	1.4.2.1 Spiral magnetism	10
	1.4.2.2 Collinear magnetism	13
1.5	Motivation	15
1.6	Outline	16
	References	19
Chapter 2	Basic physical properties of RMnO_3 manganites	23
2.1	Superexchange	23
2.2	Double exchange	24
2.3	Crystal field and Jahn-Teller effect	26
2.4	Crystal and magnetic structure	29
	2.4.1 Crystal structure	29
	2.4.2 Magnetic structure	31
	References	33
Chapter 3	Structural transformation with the doped ionic size effect	35
3.1	Introduction	35
3.2	Experiment	36
3.3	Results and discussions	37
3.4	Summary	48
	References	50
Chapter 4	Structure stabilization and magnetic behaviors of hexagonal YMnO_3 thin films	53
4.1	Introduction	54
4.2	Experiment	55
4.3	Results and discussions	57
4.4	Summary	63
	References	64

Contents

Chapter 5	Anisotropic magnetic behavior in substrate-stabilized orthorhombic YMnO_3 thin films	65
5.1	Introduction	65
5.2	Experiment	69
5.3	Results and discussions	70
5.4	Summary	85
	References	86
Chapter 6	Anisotropic electronic structure in both hexagonal and orthorhombic structured YMnO_3 thin films	88
6.1	Introduction	89
6.2	Experiment	93
6.3	Results and discussions	94
	6.3.1 Electronic structure of the MnO_5 bipyramids in hexagonal YMnO_3 thin films	94
	6.3.2 MnO_6 octahedral electronic structure in orthorhombic YMnO_3 thin films	96
6.4	Summary	102
	References	104
Chapter 7	Summary and future work	106
7.1	Summary	106
7.2	Future work	108
	Biographical notes	110



List of Tables

Table 1.1	Classification of ferroelectrics	6
Table 1.2	Crystallographic, polarization, and magnetic properties of RMnO_3 compounds for $\text{R} = \text{Y}$ and Eu to Lu	18
Table 3.1	The fitted lattice constant of $\text{Y}_{1-x}\text{A}_x\text{MnO}_3$ ($\text{A} = \text{Ca}, \text{Sr}; x = 0, 0.1, 0.3, 0.5$) serial powder	38
Table 4.1	The in-plane mismatch of hexagonal YMnO_3 and several substrates	55
Table 5.1	The fitting parameters and in-plane mismatch calculations between <i>o</i> -YMO thin films and substrates used in this study.	72



List of Figures

Fig. 1.1	Illustration of the ABO_3 perovskite with ideal cubic and distorted tetragonal structures	3
Fig. 1.2	The relation between multiferroic and magnetoelectric materials	4
Fig. 1.3	Evolution of the lattice structure in $ReMnO_3$ as a function of the size of the rare earth	7
Fig. 1.4	The crystal structure of hexagonal $YMnO_3$ in the paraelectric and ferroelectric phases	8
Fig. 1.5	KNB model in helical spin structure induced magnetoelectric polarization	10
Fig. 1.6	The relation between spiral spin orders and ferroelectric polarization in an applied field	12
Fig. 1.7	The variation of in-plane Mn-O-Mn bond angle below the lock-in transition temperature	14
Fig. 2.1	The illustrators of superexchange interaction	23
Fig. 2.2	The illustrators of double exchange interaction	25
Fig. 2.3	Illustration of the energy level split by crystal field and Jahn Teller distortion	27
Fig. 2.4	The equivalent-density surface of electronic distribution of d orbital	28
Fig. 2.5	The crystal structure of ideal cubic perovskite and real orthorhombic perovskite in $LaMnO_3$	30
Fig. 2.6	The usual magnetic structure in rare earth manganite compounds	31
Fig. 3.1	The XRD patterns for a series $YMnO_3$ doped with Ca and Sr.	37
Fig. 3.2	The Mn L edge XANES spectra for MnO (standard powder), MnO_2 (standard powder), $Y_{1-x}A_xMnO_3$ ($A = Ca, Sr$; $x = 0, 0.1, 0.3, 0.5$) polycrystalline samples, and Mn_2O_3 (standard powder)	41
Fig. 3.3	The O K edge XANES spectra of $Y_{1-x}Sr_xMnO_3$ series, intrinsic $YMnO_3$, and $Y_{1-x}Ca_xMnO_3$ series (for $x = 0, 0.1, 0.3, 0.5$)	42
Fig. 3.4	Temperature dependent susceptibility for serial powders measured by ZFC and FC method with an applied field 100 Oe, (a) intrinsic $YMnO_3$ polycrystalline powders, (b) $Y_{1-x}Ca_xMnO_3$ ($x = 0, 0.1, 0.3, 0.5$) polycrystalline powders (c) $Y_{1-x}Sr_xMnO_3$ ($x = 0, 0.1, 0.3, 0.5$) polycrystalline powders.	45
Fig. 3.5	Field dependent magnetization ($M-H$) curves taken at three different temperatures. The data were collected at 30K, 50K, and 80K respectively.	47

List of Figures

Fig. 4.1	The illustration of pulsed laser vacuum deposition system	56
Fig. 4.2	The XRD θ - 2θ patterns of hexagonal YMnO ₃ thin films grown on YSZ(111) substrates	58
Fig. 4.3	In-plane arrangements of YSZ(111) substrates and hexagonal YMnO ₃ (00 ℓ) thin film	59
Fig. 4.4	The XRD Φ -scan patterns show both off-normal YSZ(220) and <i>h</i> -YMO(112) peak with <i>h</i> -YMO(00 ℓ)/YSZ(111) thin films deposited at 880 °C	60
Fig. 4.5	Temperature dependent susceptibility of the <i>h</i> -YMO(00 ℓ)/YSZ(111) thin films.	61
Fig. 4.6	The field dependent magnetization behavior of the <i>h</i> -YMO(00 ℓ)/YSZ(111) thin films	62
Fig. 5.1	The relation between magnetic and ferroelectric order for <i>E</i> -type commensurate structure (HoMnO ₃) and the sinusoidal incommensurate order (YMnO ₃)	68
Fig. 5.2	The XRD θ - 2θ patterns of <i>o</i> -YMO thin films grown on STO(001), STO(110), and LAO(110) substrates, respectively.	71
Fig. 5.3	The schematics of the in-plane arrangements between the <i>o</i> -YMO thin films and substrates.	73
Fig. 5.4	The XRD Φ -scan patterns of <i>o</i> -YMO thin films deposited at 880 °C on different substrates.	74
Fig. 5.5	Temperature dependent magnetization along respective crystallographic orientations of <i>o</i> -YMO(00 ℓ)/STO(001), <i>o</i> -YMO(020)/LAO(110), and <i>o</i> -YMO/STO(110) thin films.	77
Fig. 5.6	Temperature dependent magnetization along respective crystallographic orientations of <i>o</i> -HMO(020)/LAO(110) thin films.	83
Fig. 5.7	Magnetic phase diagram for RMnO ₃ as a function of the ionic radius of rare earth	84

List of Figures

Fig. 6.1	Schematic orbital splitting for the majority d states of Mn^{3+} ion within orthorhombic and hexagonal crystal field	89
Fig. 6.2	Transition temperatures versus R^{3+} -ion radius (IR) in the perovskite $RMnO_3$ family.	91
Fig. 6.3	The Mn L edge XANES spectra for $LaMnO_3(001)/STO(001)$ and h - $YMO(00\ell)/YSZ(111)$ thin films	95
Fig. 6.4	The O K edge XANES spectra for h - $YMO(00\ell)/YSZ(111)$ thin film	96
Fig. 6.5	Schematic drawing of the crystal structure and the $3d$ orbitals in the MnO_6 octahedrons for orthorhombic $RMnO_3$	97
Fig. 6.6	The Mn L edge XANES spectra for standard powders (MnO , Mn_2O_3 , and MnO_2), $LaMnO_3(001)/STO(001)$, and o - $YMO(020)/LAO(110)$ thin films	98
Fig. 6.7	Schematic orbital splitting for the majority d states of Mn^{3+} ion within $RMnO_3$	99
Fig. 6.8	The O K edge XANES spectra for o - $YMO(00\ell)/LAO(110)$ thin film	100
Fig. 6.9	The illustrations of crystal structure, spin orders, and orbital orders of $LaMnO_3$ and $HoMnO_3$.	102
Fig. 7.1	Summary of the in-plane mismatch between the orthorhombic $RMnO_3$ with $Pbnm$ space group setting and the two commonly used perovskite substrates.	108

Chapter 1

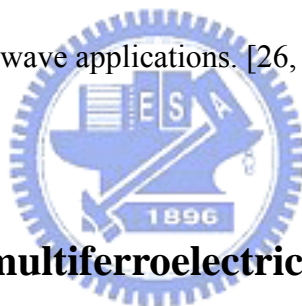
Introduction

1.1 Introduction to multiferroics

Multiferroics are materials which exhibit simultaneously long range magnetic and electric orders like ferroelectric, antiferromagnetic (AFM), and ferroelastic behaviors. More interestingly, in this kind of materials, the phase transition of one kind of order could result in another kind of order and hence manifesting itself with strong coupling between the order parameters [12-17]. Namely, the magnetic orders could be changed by an applied electric field and the electric properties could also be affected in the magnetic field when the material is in the multiferroic state. The rich physical characteristics exhibited by these materials not only present great challenges to scientists interested in understanding the prevailing underlying physics but also promise potential in various kinds of novel applications.

For instance, the multiferroic bilayer structures had been demonstrated to be very competitive in application of magnetic sensors. With the effect exerted by the probing magnetic field, the magnetic phase composite was strained and induced a proportional charge in the piezoelectric phase. This sensor shows much more sensitivity than the superconducting quantum Interference Device (SQUID), which has been often used to probing the ultra small field in the laboratory. Unlike the low temperature environment required by operating SQUID, the magnetic sensor can even be more advantageous with the possibility of operating at in ambient environment. The sensitivity of the magnetic

sensor can also be of potential use in magnetic data reading like giant magnetoresistance (GMR) or tunneling magnetoresistance (TMR). For the ultra low field sensitivity in the order of $10^{-12}\sim 10^{-15}$ T, the application of the multiferroic devices in hard disk data reader head could be much more superior as compared to the GMR and CMR sensors. Although the areal density in hard disk with GMR device can reached up to 8Gb/in^2 , [25] the magnetic recording might be further increased up to 1Tb/in^2 by using the bilayer multiferroic device schemes. [26-28] Besides, the multiferroic device could be also used in magnetoelectric (ME) gyrotors for its giant manetoelastic behavior, [26, 27] and this has been widely used in entertainment business like optical image stabilizer in digital camera, television game platforms in joystick (Wii), GPS assisted system in car driving, and etc. Moreover, the mutiferroic devices can also be prepared as tunable device, resonators, and filters in microwave applications. [26, 27]



1.2 Origin of the multiferroelectricity

Although the multiferroics can be used in many applications, it is a pity that there are only few materials naturally own the multiferroicity. In 1894, P. Curie predicted the existence of coupling between the electric and magnetic fields in materials when performing the theoretical derivation of Electromagnetism [29, 30]. Dzyaloshinskii predicted the magnetoelectric coupling in Cr_2O_3 in 1959 [31], and the experimental evidence was observed by Astrov in the Cr_2O_3 a year later in 1960 [32]. The difficulty of finding multiferroicity manifested in real materials was owing to the mutually exclusive requirements for the required orders to take place. For instance, the so-called d^0 -ness required for ferroelectricity (FE) and the unpaired d-electrons necessary for providing magnetic moments for ferromagnetism (FM) or antiferromagnetism (AFM) apparently

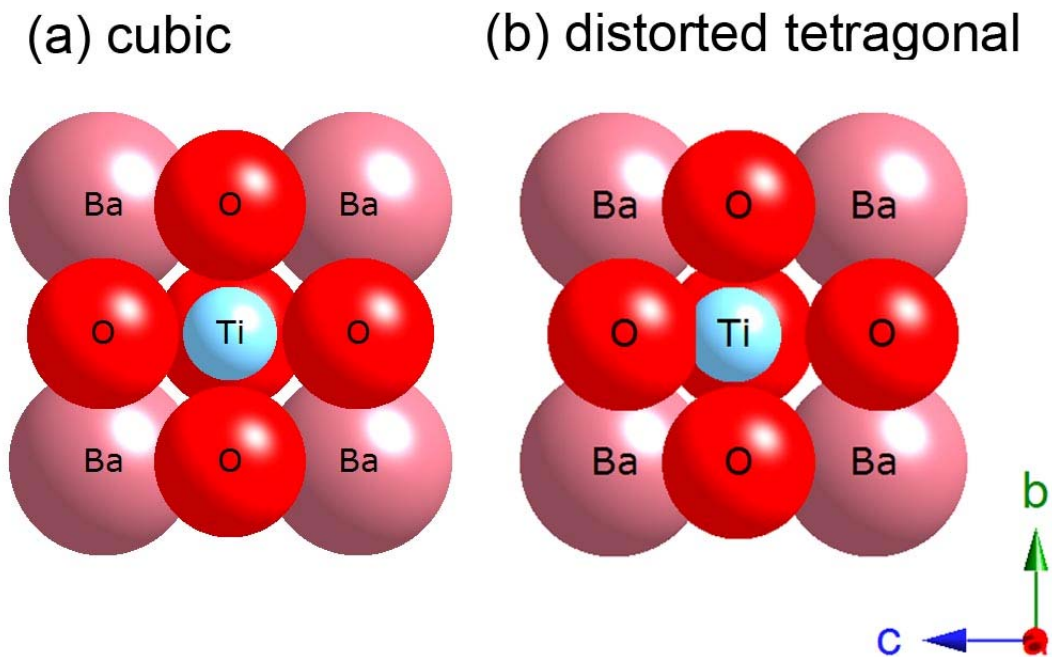


Fig. 1.1 Illustration of the ABO_3 perovskite structures with
 (a) ideal cubic symmetry for paraelectric $BaTiO_3$ and
 (b) distorted tetragonal for ferroelectric $BaTiO_3$

are counteractive to each other. By considering the perovskite oxides with the ABO_3 structure with ideal cubic symmetry (Ba and Ti was set to A-site and B-site ions), illustrated in Fig. 1.1 (a) which is typical for the traditional FE materials like tetragonal $BaTiO_3$, the hybridization between empty d orbital in TiO_6 octahedrons for the B-site and fully occupied p orbital in oxygen ions, which in turn would induce the off-center displacements of B-site ions in ABO_3 structures and hence the ferroelectricity [33]. On the other hand, it is well known that half occupied d-orbital electron spins dominate the magnetic behaviors of most of the transition metal oxides. Consequently, the existence of both ferroelectric and magnetic orders in a material imposed a difficult task on B site transition metal ions. Both ferromagnetic and ferroelectric materials require strict limits in exhibiting their special characteristics which happen to play the pivotal roles in digital age with data recording today. The status of polarization or magnetization could produce two states and be assigned to 0 and 1. Each state could be switched with an applied field

and used as non-volatile memory in hard disk or flash disk. Thus despite of the rarity of multiferroic materials as described illustrated in Fig. 1.2 schematically by W. Erenstein [20], the efforts of investigating the existent systems and to explore the new possibilities accordingly are quickly amounted worldwide. Only a few materials own both electric and magnetic orders which is so-called multiferroic, and an even smaller number of them exhibit magnetoelectric characteristics (i.e. displaying strong coupling between the two order parameters). Although the transformation between electricity and magnetism is well known by the Maxwell's descriptions and used in daily works, it is still exciting and need to be explored in controlling the magnetoelectric phase with both electric and magnetic force in the local structures.

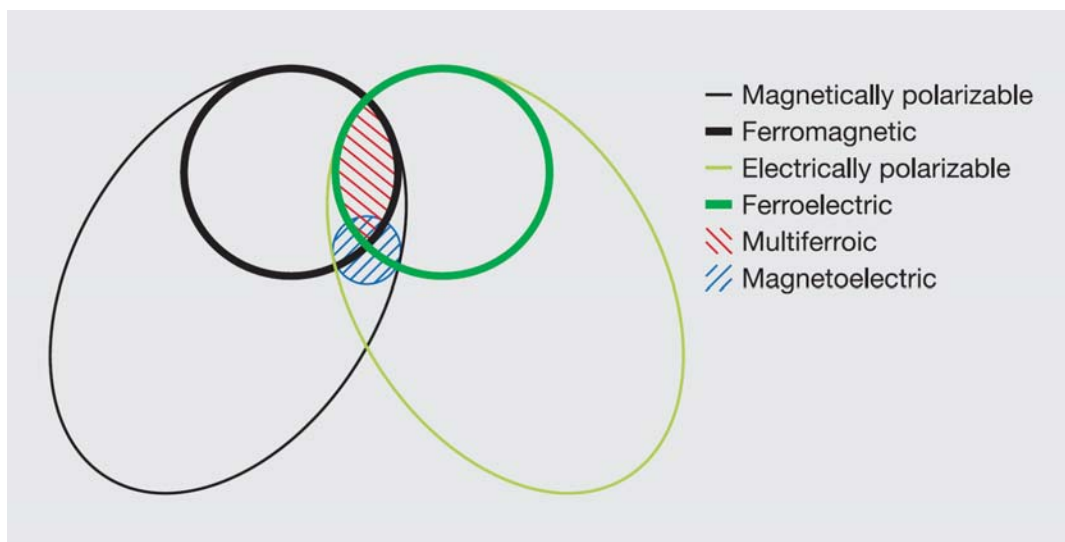


Fig. 1.2 The relation between multiferroic and magnetoelectric materials. [20]

1.3 Classification of multiferroics

Although it was not easy in finding multiferroic materials, many have started to investigate these issues recently. According to the classification proposed in the early report of W. Priller et al. (2005) [18], there are several kinds of multiferroic materials as

listed below.

1. Bi-based compounds (lone pair s electrons)
2. ReMnO_3 compounds (Re = Y, Ho, Er, Tm, Yb, and Lu)
3. ReMn_2O_5 compounds (Re = Y, Tb, Dy, and Ho)
4. Artificial multiferroic materials (multilayers and nanocomposites films)

More recently, there have been many more multiferroic materials discovered such as LuFe_2O_4 , CoCr_2O_4 [24] and some systems with reduced dimensions. Another way of describing these materials is to base on the behavior of coexistent magnetism and ferroelectricity. The traditional ferroelectrics (like BaTiO_3) exhibit tremendous enhancement of polarization with an applied electric field [34], due to the alignment of the permanent dipoles originated from the off-center distortion of B-site ions which is caused by the covalent bonding between $3d^0$ transition metal and oxygen. This is termed as the so-called “proper” ferroelectrics. Some kinds of multiferroics have higher Curie temperature like BiFeO_3 ($T_c = 1103\text{K}$), the ferroelectricity was owing to $6s^2$ lone pair and the hybridization between Bi 6p and O 2p orbital along the [111] direction in the rhombohedral distorted perovskite structure [35]. S. W. Cheong has further summarized the classification of “proper” and “improper” [36] ferroelectrics in Table 1.1 by the mechanism of ferroelectricity. [24]. In the proper ferroelectrics, the main driving force toward to the polar state was associated with the electronic pairing. In contrast, the polarization of improper ferroelectricity involves a more complex lattice distortion or other accidental by-product of some other ordering, especially for those induced by magnetic ordering.

Classification of ferroelectrics		
	Mechanism of inversion symmetry breaking	Materials
Proper	Covalent bonding between $3d^0$ transition metal (Ti) and oxygen	BaTiO ₃
	Polarization of $6s^2$ lone pair of Bi or Pb	BiMnO ₃ , BiFeO ₃ , Pb(Fe _{2/3} W _{1/3})O ₃
Improper	Structural transition	K ₂ SeO ₄ , Cs ₂ CdI ₄
	'Geometric ferroelectrics'	hexagonal RMnO ₃
	Charge ordering	LuFe ₂ O ₄
	'Electronic ferroelectrics'	
	Magnetic ordering	Orthorhombic RMnO ₃ ,
	'Magnetic ferroelectrics'	RMn ₂ O ₅ , CoCr ₂ O ₄

Table 1.1 Classification of ferroelectrics. [24]

1.4 Multiferroic RMnO₃

Perhaps, the most intriguing multiferroic system is the special series of compounds made of rare-earth manganites RMnO₃ (R = rare earth with smaller ionic size and Y). As indicated in Table 1.1 RMnO₃ has two kinds of ferroelectric behavior. The R³⁺ ions of the rare earth element have closely similar chemical characteristics for the outermost electrons with the same $5s^25p^6$ electronic configurations. For the rare earth elements (from La to Lu), on the other hand, the ionic size decreases from 1.22 Å to 0.94 Å with the increasing number of electrons residing in the 4f shell, the so-called lanthanum contraction [34]. With the variation of the ionic size, there is a structural transition in the series of the RMnO₃ compounds. As shown in Fig. 1.3 [18], the RMnO₃ perovskite oxides with R= La to Dy have stable orthorhombic structure in *Pnma* space group and these kinds of compounds fall into "Group I" in RMnO₃ [37]. These materials reveal rich physical properties such as the colossal magnetoresistance (CMR) displayed in

$\text{La}_{1-x}\text{Ca}_x\text{MnO}_3$ and a large number of related doped manganites. On the other side, the “Group II” compounds with the decreasing ionic size (for $R = \text{Ho}, \text{Lu}, \text{Y}, \text{Sc}, \text{In}$) have stable hexagonal structure with $P6_3cm$ space group thermodynamically. The critical point of the structure transition appears to locate near YMnO_3 ($\text{Y}^{3+} = 1.06\text{\AA}$) and HoMnO_3 ($\text{Ho}^{3+} = 1.05\text{\AA}$). As a result, the crystal structure of Group II compounds has been managed to transform from hexagonal to orthorhombic via high temperature, high pressure process [38, 39], soft chemistry procedures [2, 40], and the perovskite substrate stabilized thin films [41-46]. Conversely, recent reports have also described that thin films of the Group I manganites such as DyMnO_3 , TbMnO_3 , GdMnO_3 , and EuMnO_3 with hexagonal structure could be obtained by epitaxial strain stabilization with the YSZ(111) substrates and revealed complex ferroelectric orders at low temperature [6, 7, 47, 48]. It is, thus, of great interest in exploring how the structural transition in RMnO_3 and controlling the crystalline structure will affect the manifestations of multiferroicity in the same material? The representative properties of RMnO_3 (for $R = \text{Y}$ and Eu to Lu) with

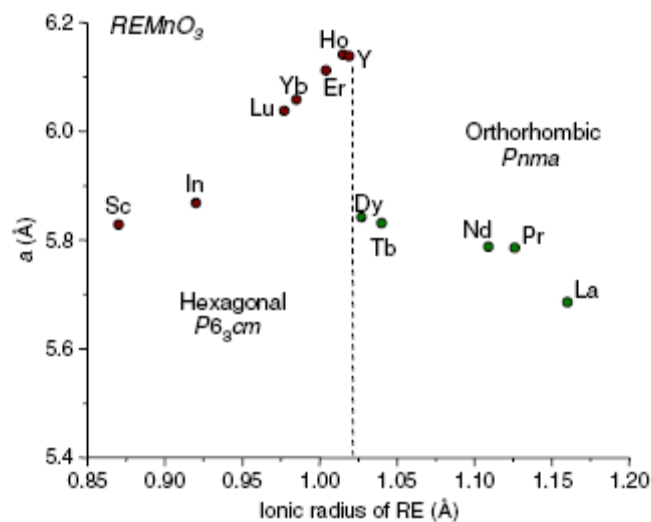


Fig. 1.3 Evolution of the lattice structure in REMnO_3 as a function of the size of the rare earth (RE). [18]

both hexagonal and orthorhombic structure reported to date are collected in Table 1.2 [1-11].

1.4.1 Hexagonal phase

The hexagonal YMnO_3 manganites exhibit ferroelectric transition at high temperature $\sim 910\text{K}$ [1] while become A-type antiferromagnetic below the Néel temperature ($T_N \sim 70\text{ K}$ in single crystalline samples) [49, 50]. The paraelectric (PE) phase above 910K has the hexagonal structure with $P6_3/mmc$ space group symmetry, and the ferroelectric (FE) phase has the hexagonal structure in $P6_3cm$ symmetry. By comparing these two phases, one finds a displacement of Y^{3+} ions occurring along c -axis

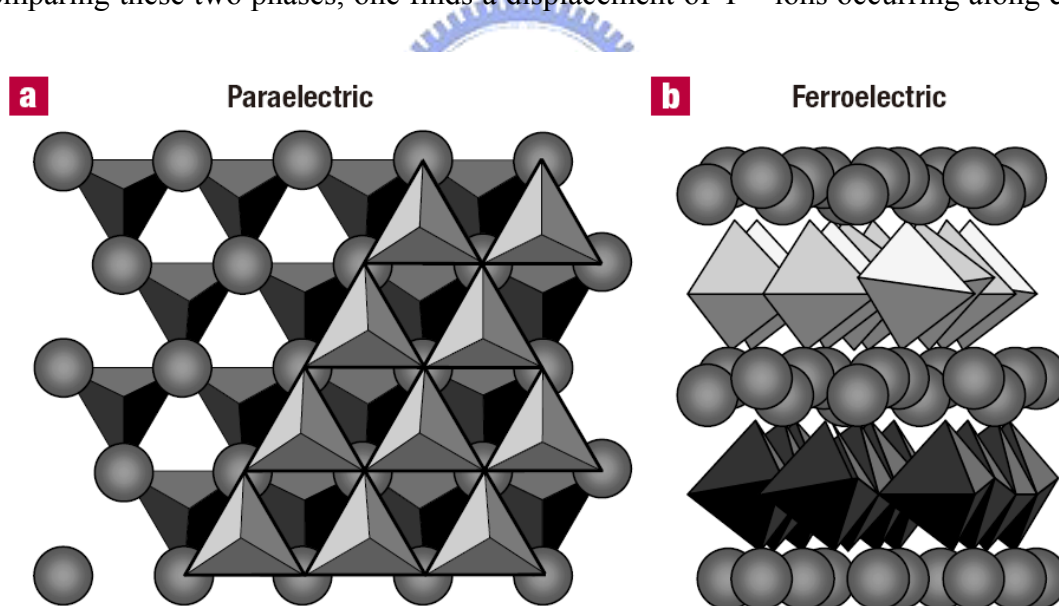


Fig. 1.4 These figures illustrate the crystal structure of YMnO_3 in the paraelectric and ferroelectric phases. The trigonal bipyramids depict MnO_5 polyhedra and the spheres represent Y ions. (a) The stacking of two consecutive MnO_5 layers and the sandwiched Y layer looking down the c axis in the paraelectric phase.(b) A view of the ferroelectric phase from perpendicular to the c axis, showing the layered nature of YMnO_3 . [23]

when undergoing PE-FE transition (Fig. 1.4) [23]. The characteristics for another compound HoMnO_3 are very similar to YMnO_3 . Wherein the ferroelectricity is caused by the displacements of Ho^{3+} , and the antiferromagnetic (AFM) phase transition occurs at about 75 K for Mn^{3+} with an additional AFM ordering occurs at temperature below 5K for Ho^{3+} [51, 52].

Owing to the huge difference between the FE Curie temperature (600 ~ 1000K) [1] and AFM Neél temperature (70 ~ 100K) [52], the magnetoelectric coupling between the two order parameters in the hexagonal manganites has been originally regarded as diminishingly small. On the other hand, for the orthorhombic manganites only magnetic orders were observed, albeit it may also be strongly affected by the variation of the rare earth's ionic size and may even induce cooperative Jahn-Teller distortion in the MnO_6 octahedrons. Until 2002, M. Fiebig et al. [53] reported the observation of coupled magnetic and electric domains in YMnO_3 by imaging the respective domains with optical second harmonic generation. Later on, they also discovered the magnetoelectric effect in HoMnO_3 by using magneto-optical techniques [51]. Soon after Fiebig's observations, it has been pointed out that, as the Mn-O bond angle deviates more from 180° with decreasing ionic size of the rare-earth ions, the modified AFM magnetic structure can induce FE order and hence provide strongly coupled ferroicities. For HoMnO_3 , the antiferromagnetic ordering of the Ho^{3+} has displayed further coupling with an applied electric field below the Neel temperature of Mn^{3+} spin orders. This declares the electric field controlled magnetic phase. Owing to the absence of the spin electrons in rare earth's 4f orbital, the ability of manipulating the magnetoelectric control at low temperatures is lacking for YMnO_3 [51, 53].

1.4.2 Orthorhombic phase

1.4.2.1 Spiral Magnetism

On the orthorhombic side of the perovskite manganites, TbMnO_3 was the first to bring about unprecedented attention for its spontaneous electrical polarization reported by Kimura et al. [14, 22]. The phenomenon was immediately coined with the so-called improper magnetic ferroelectrics (IMF). It was revealed that, in TbMnO_3 , an AFM ordering of Mn^{3+} occurs with a propagated wave vector $(0, q_{Mn}, 0)$ below 41K (T_N) along b-axis. In this state, the magnetic ordering is incommensurate with lattice order and the propagation wave vector of the magnetic order is temperature dependent. With the

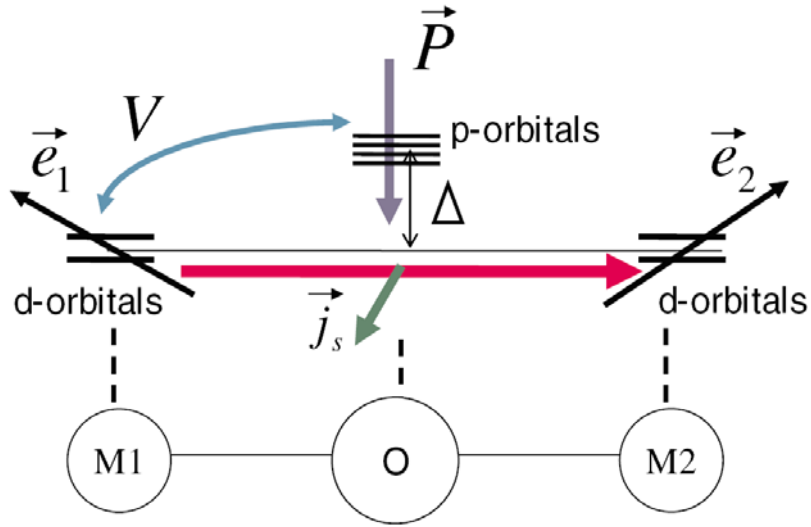


Fig. 1.5 The cluster model with two transition metal ions M1, M2 with the oxygen atom O between them. The arising spin current \vec{j}_s was induced by the noncollinear spin directions between M1 and M2. ($\vec{j}_s \propto \vec{e}_1 \times \vec{e}_2$) The direction of the electric polarization \vec{P} is given by $\vec{P} \propto \vec{e}_{12} \times \vec{j}_s$ here \vec{e}_{12} is the unit vector connecting M1 and M2 which was also the direction of propagation vector. [21]

decreasing temperature, the value of q_{Mn} increases and is locked into a constant of 0.28 below 28 K (T_L , lock-in transition temperature) [4]. This particular spin order transition was later revised by Kajimoto and was described as an incommensurate to spin spiral AFM transition. It is this spin spiral mechanism that gives rise to spontaneous polarization along the a- and c-axis and the magnetocapacitance behaviors observed in $TbMnO_3$ and $DyMnO_3$ by Kimura et al. [4]. Theoretical studies had further indicated that the noncollinear spin orders are playing important roles in controlling ferroelectric phase, and vice versa.

The theory of magnetoelectric effect was developed by Landau and Dzyaloshinskii in describing the electric polarization induced by the magnetic field [21, 54, 55]. Katsura, Nagosa, and Balatsky (KNB) [21] developed a theory in considering the spin-orbital interaction, and showed the spin spiral structure was directly originated from the spin current and magnetoelectric effect. Fig. 1.5 illustrates the relations between the interactions among M_1 -O- M_2 (M_1 , and M_2 are the magnetic ions, O is the oxygen ion) and the induced spin current \vec{j}_s . By considering the double exchange and superexchange interaction, the expression was derived below:

$$\vec{P} \sim \frac{e}{V} \vec{e}_{12} \times \vec{j}_s \dots\dots\dots (1)$$

This could be explained the origin in spiral magnets like $TbMnO_3$ and could estimate the value of polarization. In the later, other equivalent model based on Dzyaloshinskii-Moriya interaction predicts the similar results and shows spin spiral structure may induce the electric polarization. S. W. Cheong and M. Mostovoy further simplified the expression like the form of equation (2)

$$\vec{P} // (\vec{e}_1 \times \vec{e}_2) \times \vec{e}_{12} \dots\dots\dots (2)$$

to observe the polarization directly. [24]. In their description, the magnetoelectric effect is mainly originated from the symmetries of polarization and magnetization. Thus, for spontaneous polarization to occur, these two orders can only be non-collinear. Within the context of these scenarios, the polarization will not occur in the incommensurate phase because the collinear neighboring spins will result in zero cross product. Nevertheless, in helical spin array non-zero polarization is expected. Maxim Mostovoy explained the appearance of magnetocapacitance by using the Ginzburg-Landau thermodynamic potential and set up the magnetic easy axis along the x-axis ($a_x < a_y < a_z$) [19]. As is depicted in Fig. 1.6, spins spiraled on the x-y plane result in a spontaneous polarization \mathbf{P}_y , consistent with what were observed in TbMnO_3 in that the magnetic moments spiral on the a-b plane with a wave vector propagated along the b-axis and a resultant polarization in the a- or c-axis. Moreover, the polarization was found to be markedly suppressed by an applied field. The reason for this polarization suppression is that the x-y

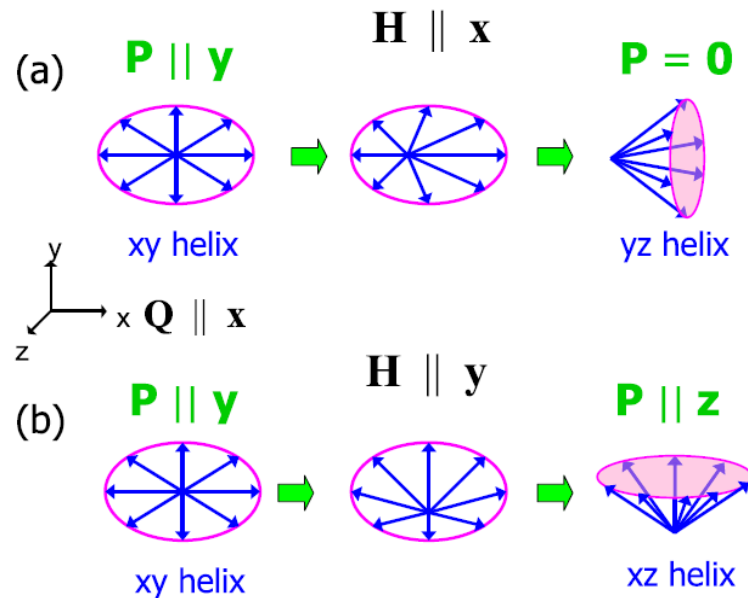
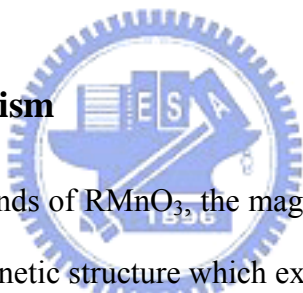


Fig. 1.6 Magnetic field behavior of electric polarization for the model of Ginzburg-Landau thermodynamic potential. In zero field spins rotate in the x-y plane and $\mathbf{P} \parallel \mathbf{y}$. Magnetic field in the x direction suppresses the polarization, while H_y orients \mathbf{P} in the z direction. [19]

helix will be broken and replaced by y-z conical helix when a field is applied along the x-axis (Fig. 1.6(a)). The new rotation axis transformed to parallel x-axis and the cross product of spin vector and propagation vector becomes zero. On the contrary, with the field applying parallel to the y-axis, polarization will be induced and parallel to z-axis. However, it is noted that usually a strong magnetic field is needed to change the spin symmetry of AFM state. Thus, the microscopic magnetoelectric behavior could be controlled only with relatively high fields. Similar feature was observed in other noncollinear multiferroics and some of them revealed reversible and memorial effect [56]. The applied field induced polarization could also be five times (DyMnO_3 : $\sim 2700 \mu\text{C}/\text{m}^2$ with an applied field 2T) larger than the spontaneous magnetoelectric effect [4, 57].

1.4.2.2 Collinear Magnetism



For the Group II compounds of RMnO_3 , the magnetic orders have been identified to turn into the E-type AFM magnetic structure which exhibits collinear spins [2, 3, 5, 8, 39, 58]. Within the context of the abovementioned magnetism-induced FE, the collinear AFM shouldn't be able to result in the complex magnetoelectric polarization described above. In 2004, Lorenz et al. reported the anomaly dielectric behavior in YMnO_3 and HoMnO_3 materials [16]. The results have led to the scientists to reconsider the role of collinear AFM in magnetoelectric effect. Sergienko et al. [22] by considering mechanisms other than spin-orbit interaction have estimated the polarization of the E-type RMnO_3 can have up to “2” orders of magnitude enhancement over that of the spiral phase RMnO_3 . The polarization in this case is induced along the *a*-axis in *Pbnm* space group setting. In their calculation, the polarization was estimated about 0.5~12 $\mu\text{C}/\text{cm}^2$ which is compatible with the hexagonal RMnO_3 (see in Table 1.2). As depicted in

Fig. 1.7, in this scenario the ferroelectricity is originated from the oxygen displacement perpendicular to the Mn-Mn bond resulted from the competition between electron hopping and elastic energy within the framework of the double exchange model [22]. For HoMnO_3 with E-type AFM, the Mn-O-Mn bond angle is close to 144° (ϕ_0). Since deviation of the bond angle ϕ_0 from 180° will cost hopping energy while it may reduce the elastic energy by having a smaller ϕ_0 . This calculation, though was put forth for the E-type AFM system, is also useable for noncollinear TbMnO_3 compounds. Picozzi et al. [59, 60] redo the calculation with first principle calculation and find that the magnetoelectric polarization is induced along mainly c-axis (consistent with the previous report [22]) and partially a-axis. The crystalline axis was set in $Pnma$ space group which

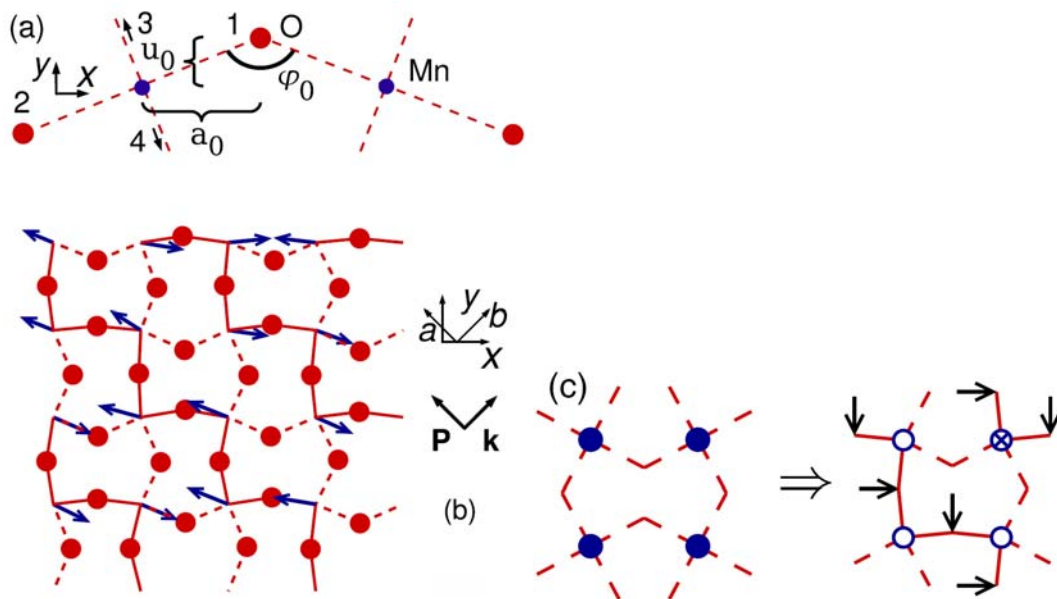


Fig. 1.7 (a) The starting configuration of a Mn-O-Mn bond. Numbers 1–4 enumerate the O atoms surrounding one Mn. (b) An MC snapshot of the IMF E -phase at $T = 0.01$. The ferromagnetic zigzag chain links are shown as solid lines. The displacements of the oxygen atoms are exaggerated. (c) Left: The local arrangement of the Mn-O bonds with disordered Mn spins (full circles). Right: Oxygen displacements (arrows) within the chains of opposite Mn spins (open and crossed circles) in the E -phase. [22]

could be also transferred to *Pbnm* space group setting. The polarization was induced by the quantum mechanism in spin-orbital interaction, and the crystal and electronic structure both needed to be considered in magnetoelectric behaviors. The first principle calculation also gave more exact estimation on the strength of the polarization caused by collinear AFM and other mechanisms.

1.5 Motivation

As has been mentioned in length, multiferroic materials have rich physical properties arising from the complicated and yet subtle interactions among the charge, spin, and orbital degree of freedoms of the carriers and the lattice. Especially, the ultimate routes of obtaining effective magnetoelectric coupling between spin and polarization are still needed to be clarified. The rare-earth manganites (RMnO_3) in particular are the interesting playgrounds featuring simultaneously the magnetism and ferroelectricity with the Jahn-Teller distortion playing an important role in mingling all these ingredients to result in various emergent physical properties like the magnetoelectric behaviors. As shown in Fig. 1.3, YMnO_3 and HoMnO_3 are of particular interest because they locate right at the verge of the crystal transition point. In addition, they were also identified to have the collinear magnetic AFM structure for Mn^{3+} at low temperature [2, 3], that makes them ideal for testing the mechanism beyond the DM spin-orbital interaction. It is also interesting to note that YMnO_3 does not have the 4f spin electrons, making it unique in clarifying the prominent role played by the Mn^{3+} spin orders. Unfortunately, up to now suitable samples of orthorhombic RMnO_3 from the Group II manganites are still lacking for measuring the directly the actual orientations of the spin ordering and the polarization associated with its transition, which couldn't be decided exactly with polycrystalline ones.

Due to the inherent difficulties of obtaining the single crystalline orthorhombic Group II manganites, thin films seem to be the only choice for resolving these hindrances. Therefore, in this work, we will first concentrate on fabricating suitable thin film samples of the orthorhombic Group II manganites. Then we will show how these films help us in characterizing the magnetism, ferroelectricity, and electronic structure that would eventually demonstrate the effects of anisotropic bonding predicted by Picozzi et al. [59].

1.6 Outline

This dissertation consists of seven chapters. We simply guide the multiferroics and its magnetoelectric coupling and mechanism in chapter 1. In Chapter 2, we will describe the basic physical properties of RMnO_3 manganites and origin of the magnetic behaviors. The relative magnetic and crystal structure in RMnO_3 compound will be also described here. In chapter 3, we will discuss the feasible routes of obtaining the orthorhombic crystal structure from the thermodynamically stable hexagonal RMnO_3 phases by substrate stabilization. We will also describe the relation between ionic size, crystal, and electronic structure in structural stabilization. Ca and Sr were used to dope YMnO_3 to investigate the effect of ionic size on the electronic structures and associated magnetic properties. In chapter 4 and 5, we clarify the role of substrate in stabilizing thin film with both hexagonal and orthorhombic structures. The strain dominates the stabilization of metastable orthorhombic structure in Group II RMnO_3 compounds. In the temperature dependence of magnetization behavior, the YMnO_3 thin films revealed significant anisotropic behavior both in hexagonal and orthorhombic structures. The spin reordering behavior was only seen along a- and c-axis which was different from the E-type HoMnO_3 . In chapter 6, x-ray absorption spectra are used to unveil the anisotropic bonding behavior

along the primary crystalline axes. Because of the MnO_6 octahedron in orthorhombic structure and MnO_5 bipyramid in hexagonal structure, the spectra show entirely different bonding behavior. Finally, we give a conclusion and future work in chapter 7.



	EuMnO ₃	Gd MnO ₃	Tb MnO ₃	Dy MnO ₃	Y MnO ₃	Ho MnO ₃	Er MnO ₃	Tm MnO ₃	Yb MnO ₃	Lu MnO ₃
Ionic size (R ³⁺)	1.13 Å	1.11 Å	1.09 Å	1.07 Å	1.06 Å	1.05 Å	1.04 Å	??1.04 Å	1 Å	0.99 Å
Crystal	hexagonal	hexagonal	hexagonal	hexagonal	hexagonal	hexagonal	hexagonal	hexagonal	hexagonal	hexagonal
Space group	<i>P</i> _{6₃} <i>cm</i>	<i>P</i> _{6₃} <i>cm</i>	<i>P</i> _{6₃} <i>cm</i>	<i>P</i> _{6₃} <i>cm</i>	<i>P</i> _{6₃} <i>cm</i>	<i>P</i> _{6₃} <i>cm</i>	<i>P</i> _{6₃} <i>cm</i>	<i>P</i> _{6₃} <i>cm</i>	<i>P</i> _{6₃} <i>cm</i>	<i>P</i> _{6₃} <i>cm</i>
T _c			?	?	~910K	~870K	~830K	~621K	~990K	~570K
Spontaneous (μC/cm ²)			~7.5(35K)	9.8(25K)	5.5	5.6	5.6	0.1	5.6	
Polarization			//[0001]	//[0001]	//[0001]	//[0001]	//[0001]	?	//[0001]	?
Crystal	orthorhombic	orthorhombic	orthorhombic	orthorhombic	orthorhombic	orthorhombic	orthorhombic	orthorhombic	orthorhombic	orthorhombic
Space group	<i>P</i> <i>b</i> <i>n</i> <i>m</i>	<i>P</i> <i>b</i> <i>n</i> <i>m</i>	<i>P</i> <i>b</i> <i>n</i> <i>m</i>	<i>P</i> <i>b</i> <i>n</i> <i>m</i>	<i>P</i> <i>b</i> <i>n</i> <i>m</i>	<i>P</i> <i>b</i> <i>n</i> <i>m</i>	<i>P</i> <i>b</i> <i>n</i> <i>m</i>	<i>P</i> <i>b</i> <i>n</i> <i>m</i>	<i>P</i> <i>b</i> <i>n</i> <i>m</i>	<i>P</i> <i>b</i> <i>n</i> <i>m</i>
T _N	~51K	~43K	~41K	~39K	~42K	~42K	~42K	~40K	~43K	~40K
T _L	~46K	~23K	~28K	~18K	~28K	~26K	~28K	~31K	~36K	~36K
Lock in <i>q</i> _{Mn} vector	?	?	0.275	~0.39	0.435	0.5	0.433	0.5(9K?)	0.5(9K?)	0.5(8K)
Spontaneous (μC/m ²)	Field induced	Field induced	~420(//a)	~100(//a)	~250	~100	?	?	?	?
Polarization	(//b)	(//a)	a-, c-axis	a-, c-axis	(μC/m ²)	(μC/m ²)	(μC/cm ²)	(μC/cm ²)	(μC/cm ²)	(μC/cm ²)
					?	//a (?)				

Table 1.2 Crystallographic, polarization, and magnetic properties of RMnO₃ compounds for R = Y and Eu to Lu. [1-11].

References

- [1] N. Fujimura, T. Ishida, T. Yoshimura, T. Ito, *Applied Physics Letters*. 69 (1996) 1011-1013.
- [2] A. Munoz, J.A. Alonso, M.T. Casais, M.J. Martinez-Lope, J.L. Martinez, M.T. Fernandez-Diaz, *Journal of Physics-Condensed Matter*. 14 (2002) 3285-3294.
- [3] T. Kimura, S. Ishihara, H. Shintani, T. Arima, K.T. Takahashi, K. Ishizaka, Y. Tokura, *Physical Review B*. 68 (2003) 060403.
- [4] T. Kimura, G. Lawes, T. Goto, Y. Tokura, A.P. Ramirez, *Physical Review B*. 71 (2005) 224425.
- [5] Y.H. Huang, H. Fjellvag, M. Karppinen, B.C. Hauback, H. Yamauchi, J.B. Goodenough, *Chemistry of Materials*. 18 (2006) 2130-2134.
- [6] J.H. Lee, P. Murugavel, H. Ryu, D. Lee, J.Y. Jo, J.W. Kim, H.J. Kim, K.H. Kim, Y. Jo, M.H. Jung, Y.H. Oh, Y.W. Kim, J.G. Yoon, J.S. Chung, T.W. Noh, *Advanced Materials*. 18 (2006) 3125-3129.
- [7] J.H. Lee, P. Murugavel, D. Lee, T.W. Noh, Y. Jo, M.H. Jung, K.H. Jang, J.G. Park, *Applied Physics Letters*. 90 (2007) 012903.
- [8] M. Tachibana, T. Shimoyama, H. Kawaji, T. Atake, E. Takayama-Muromachi, *Physical Review B*. 75 (2007) 144425.
- [9] L.J. Wang, S.M. Feng, J.L. Zhu, R.C. Yu, C.Q. Jin, *Applied Physics Letters*. 91 (2007) 172502.
- [10] F. Ye, B. Lorenz, Q. Huang, Y.Q. Wang, Y.Y. Sun, C.W. Chu, J.A. Fernandez-Baca, P.C. Dai, H.A. Mook, *Physical Review B*. 76 (2007) 060402.
- [11] H. Okamoto, N. Imamura, B.C. Hauback, A. Karppinen, H. Yamauchi, H. Fjevag, *Solid State Communications*. 146 (2008) 152-156.
- [12] M. Fiebig, T. Lottermoser, D. Frohlich, A.V. Goitsev, R.V. Pisarev, *Nature*. 419 (2002) 818.

- [13] N. Hur, S. Park, P.A. Sharma, J.S. Ahn, S. Guha, S.W. Cheong, *Nature*. 429 (2004) 392.
- [14] T. Kimura, T. Goto, H. Shintani, K. Ishizaka, T. Arima, Y. Tokura, *Nature*. 426 (2003) 55-58.
- [15] B. Lorenz, Y.Q. Wang, C.W. Chu, *Physical Review B*. 76 (2007) 104405.
- [16] B. Lorenz, Y.Q. Wang, Y.Y. Sun, C.W. Chu, *Physical Review B*. 70 (2004) 212412.
- [17] T. Lottermoser, T. Lonkai, U. Amann, D. Hohlwein, J. Ihringer, M. Fiebig, *Nature*. 430 (2004) 541.
- [18] W. Prellier, M.P. Singh, P. Murugavel, *Journal of Physics-Condensed Matter*. 17 (2005) R803.
- [19] M. Mostovoy, *Physical Review Letters*. 96 (2006) 067601.
- [20] W. Eerenstein, N.D. Mathur, J.F. Scott, *Nature*. 442 (2006) 759-765.
- [21] H. Katsura, N. Nagaosa, A.V. Balatsky, *Physical Review Letters*. 95 (2005) 057205.
- [22] I.A. Sergienko, C. Sen, E. Dagotto, *Physical Review Letters*. 97 (2006) 227204.
- [23] B.B. Van Aken, T.T.M. Palstra, A. Filippetti, N.A. Spaldin, *Nature Materials*. 3 (2004) 164-170.
- [24] S.W. Cheong, M. Mostovoy, *Nature Materials*. 6 (2007) 13-20.
- [25] R.L. Comstock., *Introduction to magnetism and magnetic recording*, 1999.
- [26] M.I. Bichurin, D. Viehland, G. Srinivasan, *Journal of Electroceramics*. 19 (2007) 243-250.
- [27] C.W. Nan, M.I. Bichurin, S.X. Dong, D. Viehland, G. Srinivasan, *Journal of Applied Physics*. 103 (2008) 031101.
- [28] Y. Zhang, Z. Li, C.Y. Deng, J. Ma, Y.H. Lin, C.W. Nan, *Applied Physics Letters*. 92 (2008) 152510.
- [29] P. Curie, *J. Phys.* 3(Ser. III). 393 (1894) 415.
- [30] Editorial, *Nature Materials*. 6 (2007) 1.

- [31] I.E. Dzyaloshinskii, Sov. Phys. JETP. 10 (1959) 628-629.
- [32] D.N. Astrov, Sov. Phys. JETP. 11 (1960) 708–709
- [33] N.A. Hill, A. Filippetti, Journal of Magnetism and Magnetic Materials. 242 (2002) 976-979.
- [34] C. Kittel, Introduction to Solid State Physics - 7th ed., 1996.
- [35] J. Wang, J.B. Neaton, H. Zheng, V. Nagarajan, S.B. Ogale, B. Liu, D. Viehland, V. Vaithyanathan, D.G. Schlom, U.V. Waghmare, N.A. Spaldin, K.M. Rabe, M. Wuttig, R. Ramesh, Science. 299 (2003) 1719-1722.
- [36] A.P. Levanyuk, D.G. Sannikov, Sov. Phys. Usp. 17 (1974) 199-214.
- [37] J.S. Zhou, J.B. Goodenough, J.M. Gallardo-Amores, E. Moran, M.A. Alario-Franco, R. Caudillo, Physical Review B. 74 (2006) 014422.
- [38] M.N. Iliev, M.V. Abrashev, H.G. Lee, V.N. Popov, Y.Y. Sun, C. Thomsen, R.L. Meng, C.W. Chu, Physical Review B. 57 (1998) 2872-2877.
- [39] J.S. Zhou, J.B. Goodenough, Physical Review Letters. 96 (2006) 247202.
- [40] J.A. Alonso, M.J. Martinez-Lope, M.T. Casais, M.T. Fernandez-Diaz, Inorganic Chemistry. 39 (2000) 917-923.
- [41] T.H. Lin, C.C. Hsieh, H.C. Shih, C.W. Luo, T.M. Uen, K.H. Wu, J.Y. Juang, J.Y. Lin, C.H. Hsu, S.J. Liu, Applied Physics Letters. 92 (2008) 132503.
- [42] P.A. Salvador, T.D. Doan, B. Mercey, B. Raveau, Chemistry of Materials. 10 (1998) 2592.
- [43] X. Marti, F. Sanchez, J. Fontcuberta, M.V. Garcia-Cuenca, C. Ferrater, M. Varela, Journal of Applied Physics. 99 (2006) 08p302.
- [44] X. Marti, V. Skumryev, V. Laukhin, F. Sanchez, M.V. Garcia-Cuenca, C. Ferrater, M. Varela, J. Fontcuberta, Journal of Materials Research. 22 (2007) 2096.
- [45] C.C. Hsieh, T.H.S. Lin, H. C. , C.-H. Hsu, C.W. Luo, J.-Y.W. Lin, K. H., T.M. Uen, J.Y. Juang, submit to Journal of Applied Physics (2008).
- [46] H.C. Shih, T.H. Lin, C.C. Hsieh, C.W. Luo, J.-Y. Lin, J.L. Her, H.D. Yang, C.-H. Hsu, K.H. Wu, T.M. Uen, J.Y. Juang, submit to New Journal of Physics (2008).

- [47] D. Lee, J.H. Lee, S.Y. Jang, P. Murugavel, Y.D. Ko, J.S. Chung, *Journal of Crystal Growth*. 310 (2008) 829-835.
- [48] A.A. Bosak, C. Dubourdieu, J.P. Senateur, O.Y. Gorbenko, A.R. Kaul, *Journal of Materials Chemistry*. 12 (2002) 800-801.
- [49] M.N. Iliev, H.G. Lee, V.N. Popov, M.V. Abrashev, A. Hamed, R.L. Meng, C.W. Chu, *Physical Review B*. 56 (1997) 2488-2494.
- [50] T. Lonkai, D. Hohlwein, J. Ihringer, W. Prandl, *Applied Physics a-Materials Science & Processing*. 74 (2002) S843-S845.
- [51] T. Lottermoser, T. Lonkai, U. Amann, D. Hohlwein, J. Ihringer, M. Fiebig, *Nature*. 430 (2004) 541-544.
- [52] H. Sugie, N. Iwata, K. Kohn, *Journal of the Physical Society of Japan*. 71 (2002) 1558-1564.
- [53] M. Fiebig, T. Lottermoser, D. Frohlich, A.V. Goitsev, R.V. Pisarev, *Nature*. 419 (2002) 818-820.
- [54] L.D. Landau, E. Lifshitz, *Electrodynamics of Continuous Media* (Butterworth-Heinemann, Oxford), 2002.
- [55] I.E. Dzyaloshinskii, *Sov. Phys. JETP*. 10 (1960) 628.
- [56] N. Hur, S. Park, P.A. Sharma, J.S. Ahn, S. Guha, S.W. Cheong, *Nature*. 429 (2004) 392-395.
- [57] N. Aliouane, D.N. Argyriou, J. Stremper, I. Zegkinoglou, S. Landsgesell, M.V. Zimmermann, *Physical Review B*. 73 (2006) 020102.
- [58] B.B. van Aken, A. Meetsma, T.T.M. Palstra, *Acta Crystallographica Section E-Structure Reports Online*. 57 (2001) I101-I103.
- [59] S. Picozzi, K. Yamauchi, G. Bihlmayer, S. Blugel, *Physical Review B*. 74 (2006) 094402.
- [60] S. Picozzi, K. Yamauchi, B. Sanyal, I.A. Sergienko, E. Dagotto, *Physical Review Letters*. 99 (2007) 227201.

Chapter 2

Basic physical properties of RMnO_3 manganites

2.1 Superexchange

The indirect interaction describes the virtual hopping of electrons between the oxygen ions and neighboring metal ions. Fig. 2.1 illustrates the spin superexchange interaction

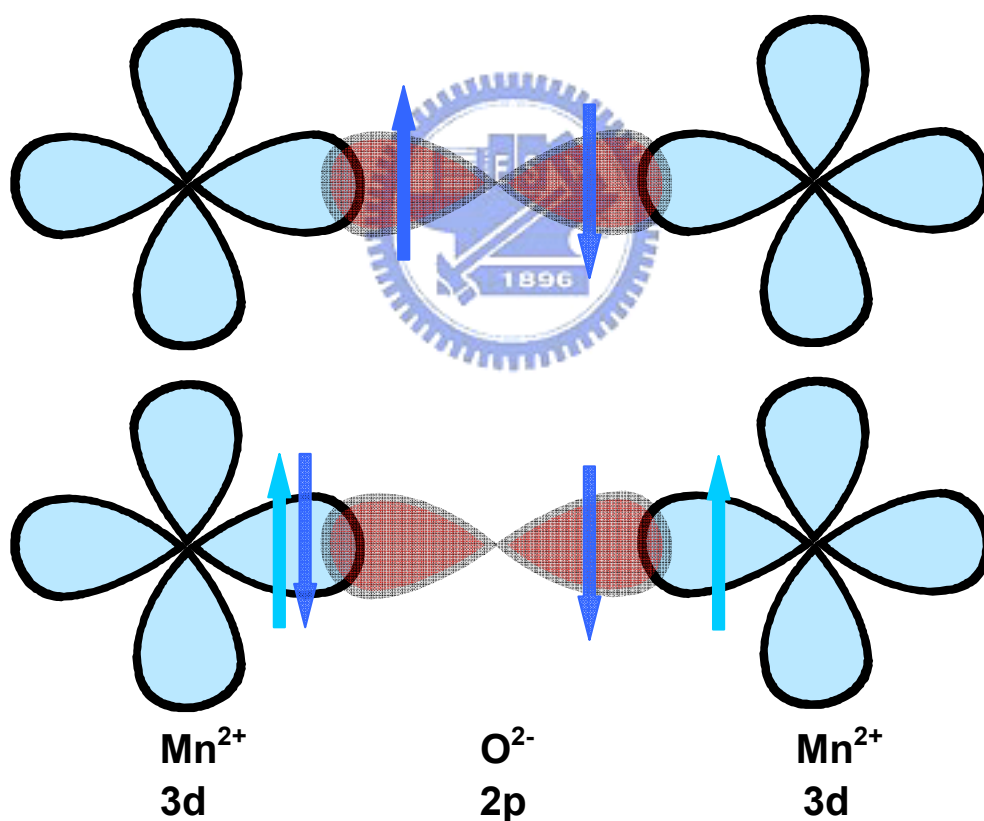



Fig. 2.1 Top: The wave function of O^{2-} 2p and Mn^{2+} 3d overlapping in the superexchange interactions. Bottom: The excited state in the superexchange interaction. [reproduced with Reference [1]]

taking place along the Mn-O-Mn chain of the MnO_6 octahedron crystal structure [1]. The 3d orbital of Mn^{2+} couples with the p-orbital of O^{2-} . The overlap of the wave functions of the p- and d-orbitals leads to the so-called p-d rehybridization. The electrons locate at the left-hand-side of the oxygen p-orbital could mediate to the neighboring manganese. According to the Pauli's exclusion principle, the electrons in manganese must be antiparallel to the mediating one. The O^{1-} becomes the excited state with an unpaired electron, which can be, in turn, paired with the other neighboring manganese. These two neighboring manganese ions are thus effectively coupled by virtue of the bridging of the oxygen ions and result in an antiferromagnetic ordering.

2.2 Double exchange



Intrinsic perovskite manganese LaMnO_3 is a well known parent manganite compound exhibiting A-type AFM originated from the orbital ordering ($3x^2-r^2$, $3y^2-r^2$) staggered behavior with $T_N = 140\text{K}$ [2]. $\text{La}_{1-x}\text{A}_x\text{MnO}_3$ ($\text{A} = \text{Ca}, \text{Sr}, \text{Ba}, \text{Ce}, \text{Sn}, \text{and etc.}$) are having the mixed valence state in manganese ions by replacing La^{3+} with the "A" ions. These doped LaMnO_3 have been shown to exhibit ferromagnetic behavior accompanied by the metal-insulator transition around the Curie temperature. This characteristic was explained by the double exchange mechanism proposed by Clarence Zener [3]. With the crystal field the degeneracy of the d-orbital of the transition metal manganese is lifted and splits into a doublet e_g ($d_{x^2-y^2}$ and $d_{3z^2-r^2}$) and a triplet t_{2g} (d_{xy} , d_{yz} , and d_{zx}) state. As a result, the Mn^{3+} and Mn^{4+} ions will have the ground state configuration of $t_{2g}^3e_g^1$ and $t_{2g}^3e_g^0$, respectively, as illustrated schematically in Fig. 2.2(b). For instance, in Ca-doped LaMnO_3 , the manganese becomes Mn^{3+} and Mn^{4+} mixed valence and results in finite conductivity originated from the hopping e_g electrons between neighboring Mn^{3+} and Mn^{4+}

ions. The hopping process is also illustrated in Fig. 2.2. On the top row of Fig. 2.2(a), the initial state can be expressed as $(\text{Mn}^{3+}-\text{O}^{2-}-\text{Mn}^{4+})$. On the bottom of Fig. 2.2(a), the left-hand-side electron in manganese hops to the right-hand-side next neighboring manganese and the state configuration is now expressed as $(\text{Mn}^{4+}-\text{O}^{2-}-\text{Mn}^{3+})$. There may be also metastable states, such as $(\text{Mn}^{3+}-\text{O}^{1-}-\text{Mn}^{3+})$ between these two processes. All the processes must also obey the Hund's rule, thus, the lowest energy state is achieved with all the spins in parallel between the neighboring transition metal ions, leading to the ferromagnetic state in Zener's report. This indirect electronic mediated magnetic ordering

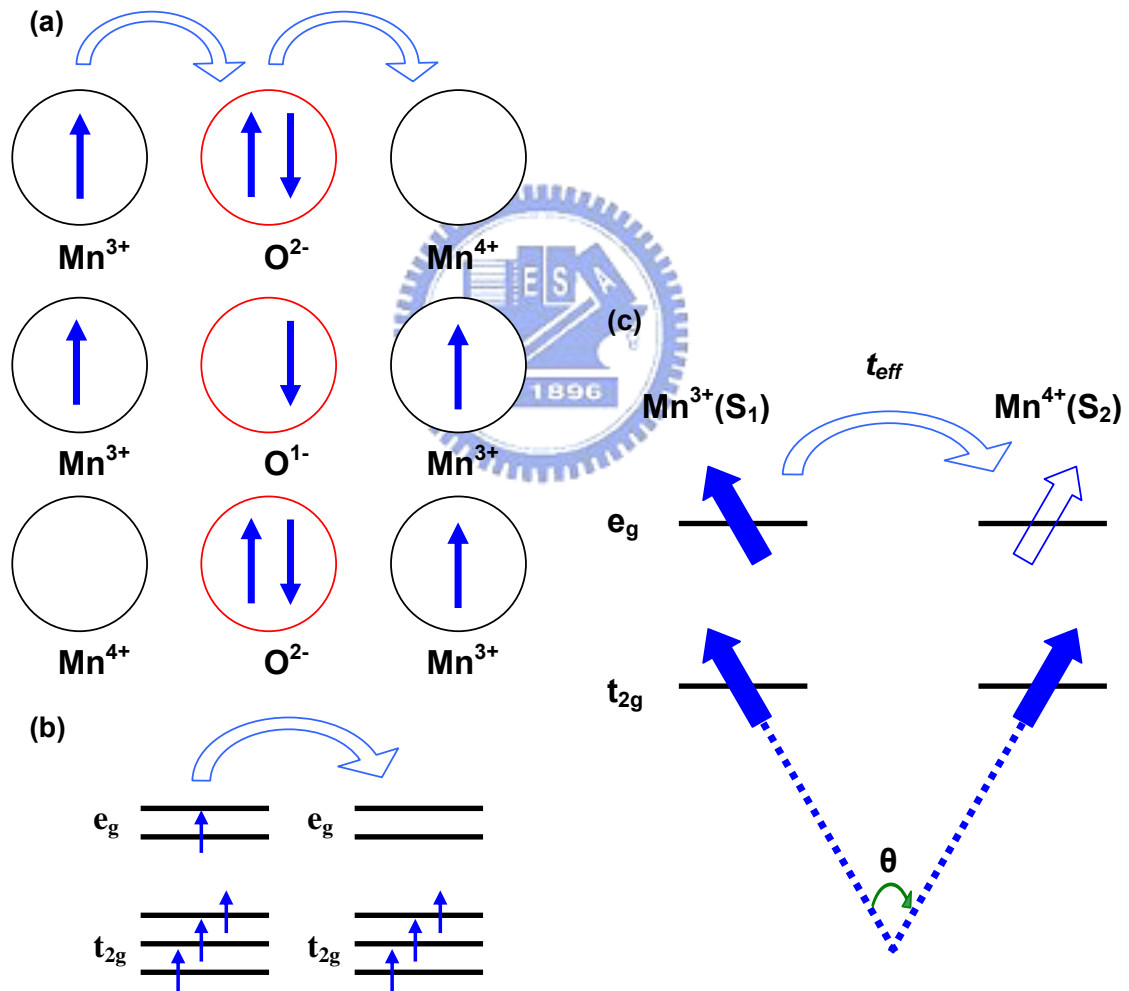


Fig. 2.2 (a) and (b) depict the hopping processes of the double exchange. (c) Effective hopping between the two noncollinear spins. [reproduced with redereence [3-5]]

process has been termed as the double exchange mechanism. Later, P. W. Anderson and H. Hasegawa further considered the real hopping integral might be obtained in double exchange [4, 5]. In Fig. 2.2(c), the effective hopping between two neighboring transition metal ions is defined as $t_{eff} = t \cdot \cos(\frac{\theta}{2})$ where θ was the angle between the two spin orientations. The Pauli's exclusion principle requires that the e_g and t_{2g} electrons possess the same spin state and the angle could also be simply described as t_{2g} electronic spins. For the antiparallel spin situation, $\theta = 180^\circ$ the system is antiferromagnetic, the effective hopping will be zero and electrons cannot hop in this situation. In contrast, hopping will be the largest when $\theta = 0^\circ$.

2.3 Crystal field and Jahn-Teller effect

As mentioned above, in transition metal compounds, there exists five-fold degeneracy in the 3d orbitals. Fig. 2.3 shows the electronic structure and the most prominent atomic arrangement of a representative ideal cubic perovskite (e.g. LaMnO_3). The Mn ion locates at the center of the MnO_6 octahedron and is surrounded by six oxygen anions. Ideally, the bond length of the six Mn-O bonds is equivalent. Nevertheless, the 3d shell experiences strong inhomogeneous field originated from the neighboring ions. As a result, the five fold degeneracy is lifted and splits into e_g and t_{2g} orbitals. The respective electronic distribution of the d -orbitals are schematically illustrated in Fig 2.4 [6]. The t_{2g} orbitals (d_{xy} , d_{yz} , and d_{zx}) will be hybridized by the oxygen p orbital and form the π -bond while the e_g orbitals ($d_{x^2-y^2}$ and $d_{3z^2-r^2}$) will hybridize with the oxygen p-orbital to form the σ bond. The energy splitting between the t_{2g} and e_g states has been usually set to be $10Dq$. The energy conservation law suggests that the energy of the e_g orbital is raised up

by $6Dq$ and that of the t_{2g} orbital will be lowered by $4Dq$ when the crystal field interaction is considered [5, 7].

For Mn^{3+} , there are four 3d electrons. Three electrons occupy each triplet t_{2g} orbital and the final electron occupies the e_g orbital. In real case, the spatial symmetry of the ideal cubic perovskite is broken by doping. Replacing the La-ions by ions with different ionic size and electronic valences induces a noncubic potential and distorts the crystal lattice. Further energy splitting is induced by the distortion of MnO_6 and such a spontaneous displacement is the so-called Jahn-Teller effect. Fig. 2.3 shows two

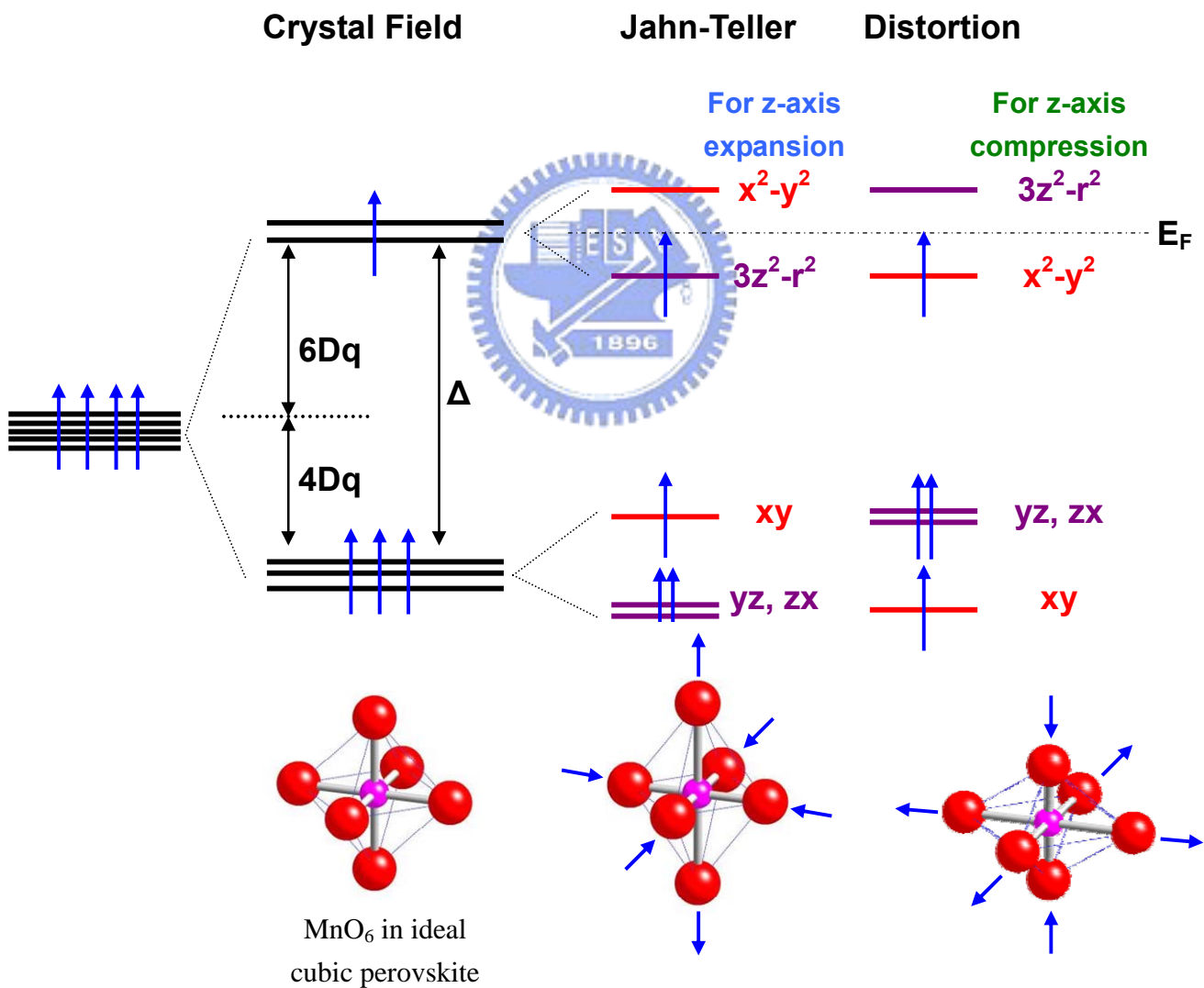


Fig. 2.3 Illustration of the energy level split by crystal field and Jahn Teller distortion. Pink and red ball denoted the Mn and O ions respectively. [reproduced with redereence [5-7]]

distortion modes of the MnO_6 octahedrons. By taking into account the Jahn-distortion, e_g and t_{2g} energy levels are split when the bond length of the Mn-O bonds is no longer equivalent. If the octahedron is expanded along the z-axis, the e_g orbitals are split into the higher $d_{x^2-y^2}$ and the lower $d_{3z^2-r^2}$ levels and the t_{2g} orbitals are split into the higher d_{xy} and the lower energy level for d_{yz} and d_{zx} . The energy splitting distribution is also shown in Fig. 2.3 for the situation when the z-axis is under compression. The basic forms of Jahn-Teller distortion in influencing electron phonon coupling has been

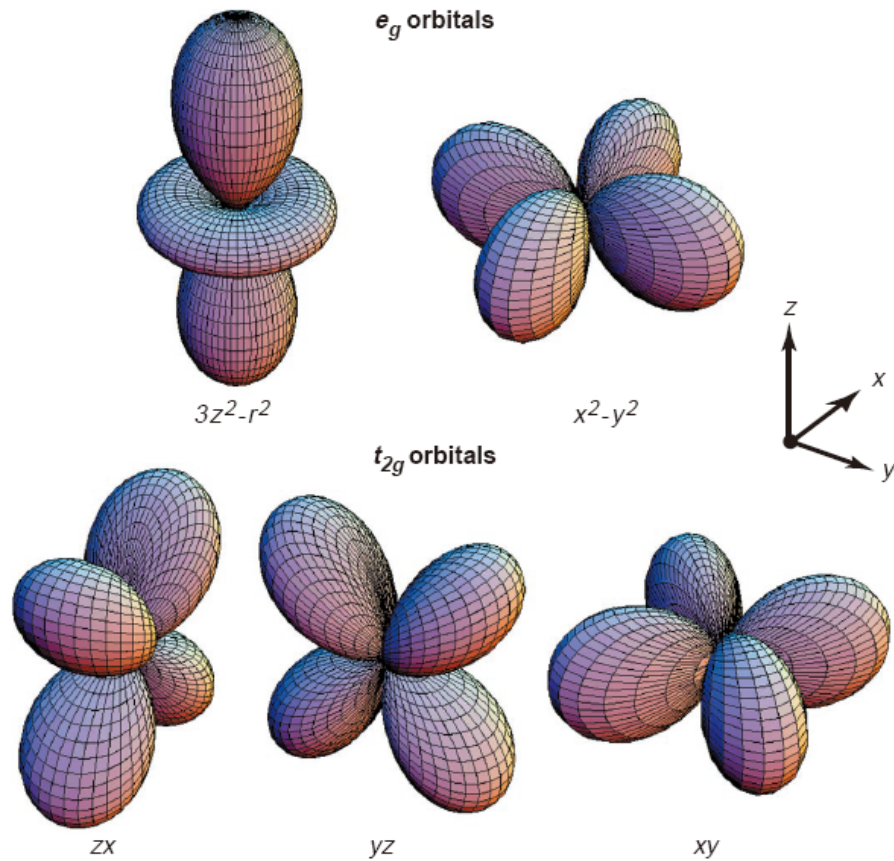


Fig. 2.4 The equivalent-density surface of electronic distribution of d orbital. With the crystal field splitting, the degenerate was separated to doublet e_g ($3z^2-r^2$ and x^2-y^2) and triplet t_{2g} (xy , yz , and xz) orbital. [17]

formulated by Kanamori [5, 8, 9]. There are different kinds of distortion and are usually classified as 3 different modes Q_1 , Q_2 , and Q_3 . Q_1 mode means that the x-, y-, z-axis are

stretching or contracting as a whole and is usually called as the breathing mode. Q_2 mode describes the x-axis expansion and y-axis compression or vice versa. Q_3 mode describes the z-axis compression accompanied with expansion in x-y plane or z-axis expansion accompanied with compression in x-y plane. The Q_3 mode usually involves the Q_2 mode.

2.4 Crystal and magnetic structure

2.4.1 Crystal structure

The serial compounds of RMnO_3 (for La to Eu) with orthorhombic structure have the same space group setting $Pbnm(62)$. Figure 2.5(a) shows the ideal cubic perovskite structure of LaMnO_3 with a MnO_6 octahedron specifically identified [9]. Figure 2.5(b) shows the similar crystal structure of the perovskite LaMnO_3 which has been slightly distorted by the Jahn Teller distortions. The lattice constants have also been correspondently modified by the compressive and expansive strain leading to the variations in the Mn-O bond length and Mn-O-Mn bond angles. There is a trend showing the decrease in bond angle with the decreasing ionic size. To quantify the distortion with the competition between the A-site atom and Mn element, the tolerance factor t has been defined as: $t = \frac{(d_{A-O})}{\sqrt{2}(d_{Mn-O})}$, where d_{A-O} is the bond length of the A-site element and oxygen and d_{Mn-O} is the bond length between Mn and oxygen [10]. For $t = 1$, it means the cubic perovskite with the Mn-O-Mn bond angle towards 180° and Mn-O bond length being isotropically equivalent.

There also has been another space group setting $Pnma$ frequently used to describe the crystal symmetry of these compounds. These two space groups can be easily converted to each other with the relation [11].

Pbnm	Pnma
a	a'
b	b'
c	c'

In this work, we use *Pbnm* space group setting in that the c-axis lattice constant is the longest lattice constant of the crystal structure.

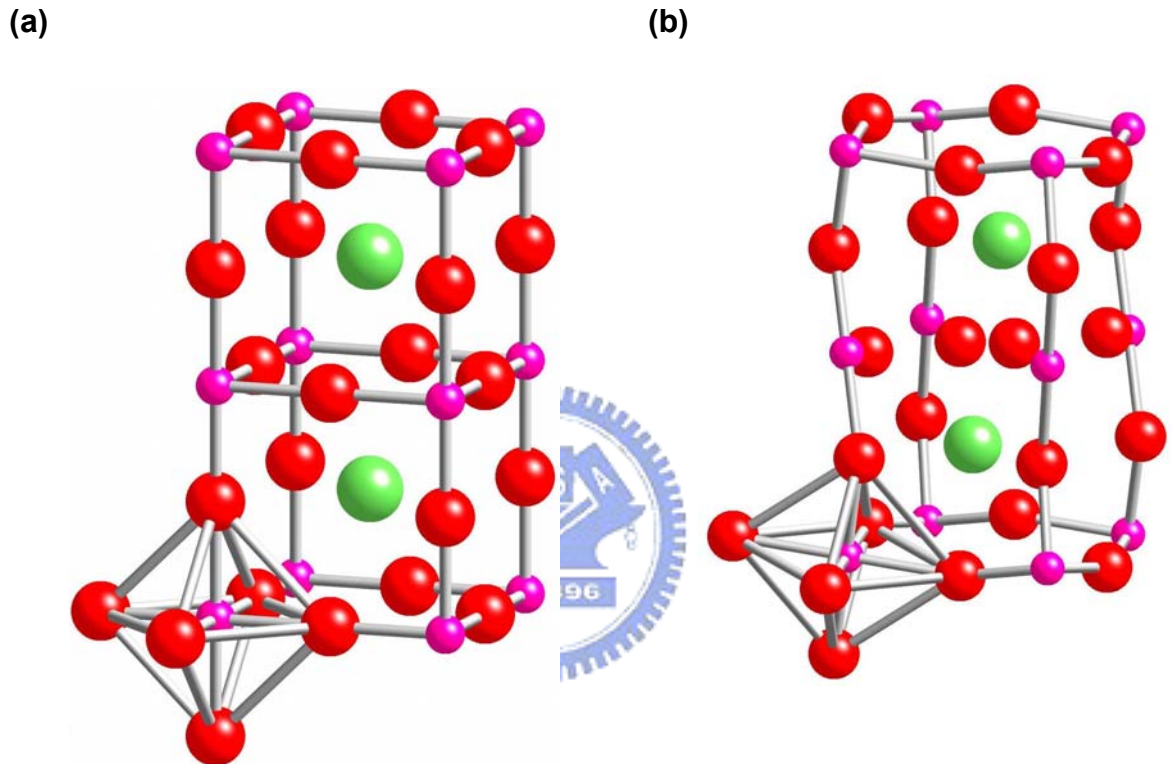


Fig. 2.5 The crystal structure of (a) ideal cubic perovskite LaMnO_3 and (b) real orthorhombic perovskite LaMnO_3 . Green, pink, and red ball denoted the La, Mn, O atoms in the crystal structure respectively. The MnO_6 octahedron was distorted by Jahn-Teller effect with combination complicated in-plane and c-axis distortion. The apical Mn-O-Mn chain in MnO_6 wouldn't parallel to c-axis.

2.4.2 Magnetic structure

In an early report, Wollan and Koehler determined the magnetic structure of the $\text{La}_{1-x}\text{Ca}_x\text{MnO}_3$ system with neutron powder diffraction [12, 13]. In Fig. 2.6(a), the circles are the Mn ions and the sign of the notation indicates the orientation of the z-axis spin projection. For example, the A-type magnetic structure has the spins ordering ferromagnetically in plane and the interplanar coupling reveals an antiparallel antiferromagnetic ordering. The macroscopic bulk characteristic will exhibit the A-type as an antiferromagnetic material in magnetization behavior. On the other hand, the B-type reveals the ferromagnetic behavior for their parallel spin orders no matter in the x-y plane

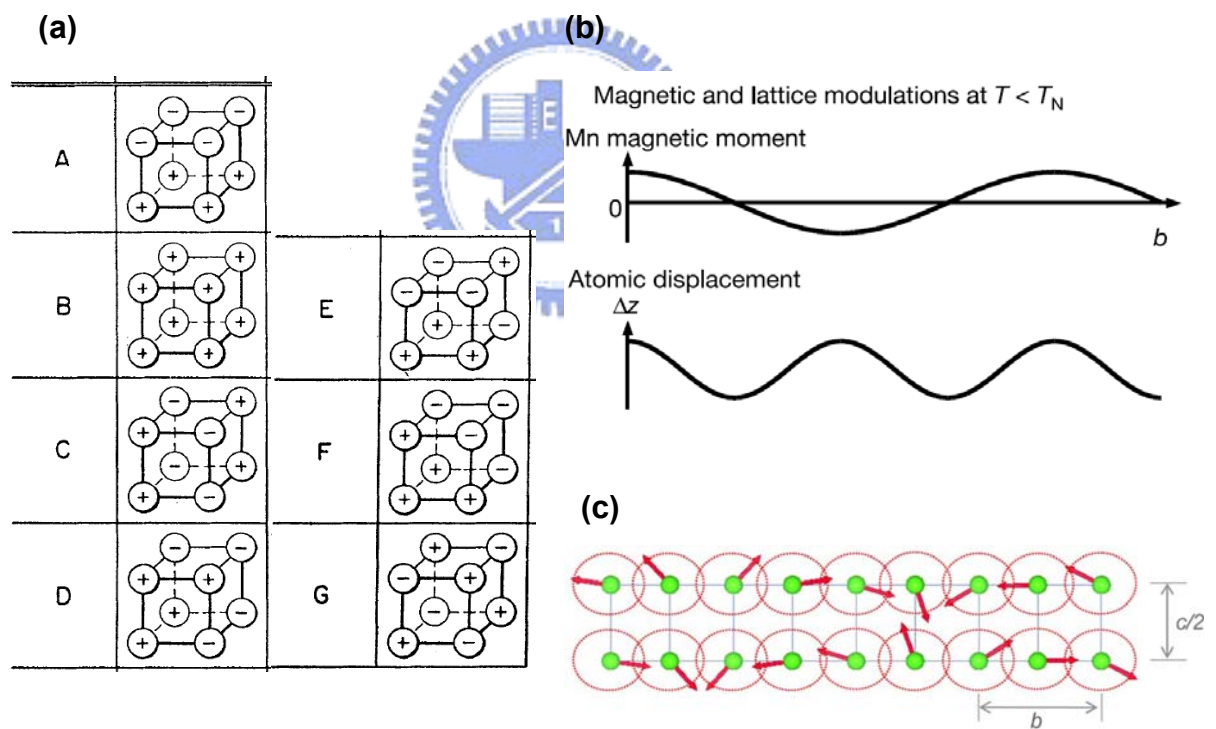


Fig. 2.6 (a) The classification of magnetic structure labeled by E. O. Wollan and W. C. Koehler.[13] (b) The illustration of comparing incommensurate spin orders and atomic orders in crystalline structure. [17] (c) The illustration of spin spiral AFM phase for TbMnO_3 . [18]

or along z-axis. An E-type magnetic order has a special spin arrangement and has been theoretically predicted to be capable of inducing strong magnetoelectric polarization [14, 15]. It is also vividly described as a “up-up-down-down” type magnetic spin ordering and usually observed in RNiO_3 (R= trivalent lanthanoids but without La) systems [16]. The E-type ordering has two up spins followed by two down spins along the principal axes of the cubic unit cell. This is different from another spin spiral phase that has induced most of the multiferroicities observed to date.

Fig. 2.6(b) shows the incommensurate spin spiral AFM magnetic orders in multiferroic TbMnO_3 [17, 18]. The term of incommensuration (ICM) means that the spin ordering periodicity is not compatible in a rational manner to the periodicity of the underlying crystal structure, as sketched schematically in Fig. 2.6(b). The ICM AFM ordering has been observed ubiquitously in the entire family of RMnO_3 (R = Y and rare earth Eu to Lu) compounds in their magnetic phase diagram. The spin density wave propagates along the b-axis with a propagation vector $(0, k_s, 0)$. The parameter k_s describes the periodic relation between the magnetic and crystal structure. For HoMnO_3 , the k_s parameter increases ($0.4 \leq k_s < 0.5$ for the incommensurate state) with Mn^{3+} spin orders below T_N and finally locked into $k_s = 0.5$ when transforming into the commensurate (CM) state and becomes temperature independent. The temperature at which the transition occurs is called the locked-in transition temperature (T_L).

Recently, with the improvement of the instrumentation and sample preparation techniques, the magnetic structure of TbMnO_3 was revised by Kajimoto [19]. In his report, TbMnO_3 was found to involve magnetic structures of ICM A-, G-, C-, and F-type below T_N , and the G-, C-, F-type were further enhanced in the CM state below T_L . The G-, C-, F-type suppressed the A-type AFM orders. The complex orders appear to be rather confusing, and was later re-assigned as a spiral phase by Kimura et al. [20]. The spiral

AFM mechanism has since then played a key role in magnetoelectric materials.

References

- [1] R.L. Comstock., Introduction to magnetism and magnetic recording, 1999.
- [2] M. Tachibana, T. Shimoyama, H. Kawaji, T. Atake, E. Takayama-Muromachi, Physical Review B. 75 (2007) 144425.
- [3] C. Zener, Physical Review. 82 (1951) 403.
- [4] P.W. Anderson, H. Hasegawa, Physical Review. 100 (1955) 675.
- [5] T. Chatterji, Colossal Magnetoresistive Manganites, 2004.
- [6] Y. Tokura, N. Nagaosa, Science. 288 (2000) 462-468.
- [7] C. Kittel, Introduction to Solid State Physics - 7th ed., 1996.
- [8] J. Kanamori, Journal of Applied Physics. 31 (1960) S14-S23.
- [9] S. Satpathy, Z.S. Popovic, F.R. Vukajlovic, Physical Review Letters. 76 (1996) 960-963.
- [10] E. Dagotto, T. Hotta, A. Moreo, Physics Reports-Review Section of Physics Letters. 344 (2001) 1-153.
- [11] International tables for crystallography, Dordrecht, Holland ;D. Reidel Pub. Co. ;c2004.Boston, U.S.A. :Sold and distributed in the U.S.A. and Canada by Kluwer Academic Publishers Group,Hingham, MA :, 2004.
- [12] E. Dagotto, Nanoscale Phase Separation and Colossal Magnetoresistance, 2002.
- [13] E.O. Wollan, W.C. Koehler, Physical Review. 100 (1955) 545.
- [14] I.A. Sergienko, C. Sen, E. Dagotto, Physical Review Letters. 97 (2006) 227204.
- [15] S. Picozzi, K. Yamauchi, B. Sanyal, I.A. Sergienko, E. Dagotto, Physical Review Letters. 99 (2007) 227201.

- [16] T. Kimura, S. Ishihara, H. Shintani, T. Arima, K.T. Takahashi, K. Ishizaka, Y. Tokura, *Physical Review B*. 68 (2003) 060403.
- [17] T. Kimura, T. Goto, H. Shintani, K. Ishizaka, T. Arima, Y. Tokura, *Nature*. 426 (2003) 55-58.
- [18] Y. Yamasaki, H. Sagayama, T. Goto, M. Matsuura, K. Hirota, T. Arima, Y. Tokura, *Physical Review Letters*. 98 (2007) 147204.
- [19] R. Kajimoto, H. Yoshizawa, H. Shintani, T. Kimura, Y. Tokura, *Physical Review B*. 70 (2004) 012401.
- [20] T. Kimura, G. Lawes, T. Goto, Y. Tokura, A.P. Ramirez, *Physical Review B*. 71 (2005) 224425.



Chapter 3

Structural transformation with the doped ionic size effect

3.1 Introduction

As discussed in chapter 1, the materials exhibiting multiferroic characteristics are usually classified into three types: (i) the Bi-based compound like BiFeO₃ or BiMnO₃, in that the lone pair of Bi 6s electrons are responsible for the ferroelectricity (FE) [1]; (ii) the ReMnO₃ perovskites (Re = Tb, Dy, Y, Ho, Er, Tm, Yb, Lu) [1-7]; and (iii) the ReMn₂O₅ double-layer perovskites (Re = Y, Tb, Dy, Ho) [1, 8]. Interestingly, many of the ReMnO₃ perovskites are also representative materials exhibiting the colossal magnetoresistance (CMR) [9, 10].

It has been established that, in this family, decreasing the ion size of the rare earth elements will gradually drive the structure of ReMnO₃ from orthorhombic into hexagonal. However, the ferroelectric Curie temperature of the hexagonal manganites usually is much higher than the magnetic ordering temperature and the linear magnetoelectric effect is usually not allowed by symmetry at zero-field [3]. Nevertheless, evidences of coupling between the c-axis polarization and in-plane staggered antiferromagnetic (AFM) magnetization have been demonstrated in HoMnO₃. [12, 13] In this respect, with the ionic size sitting right at the orthorhombic and hexagonal phase boundary of perovskite manganites, YMnO₃ (*h*-YMO) (with Y³⁺ (1.06Å)) is of particular interest. Indeed, extraordinary spin-phonon interaction was observed through the thermal conductivity measurements on this so-called geometrically frustrated FE system. [16] Since the ferroelectric polarization along the c-axis in *h*-YMO comes from the structure

distortion such as tilted MnO_5 and displacement of Y^{3+} ions [5], it is, thus, interesting to conduct a systematic study to see how the lattice distortion induced by ion size difference affects the relative ionic displacement and the associated modifications in the staggered frustrated magnetic moments and electronic structure. In this paper, we report the magnetic properties, O K-edge X-ray absorption near edge spectroscopy (XANES) and Mn L edge XANES on a series of doped multiferroic materials $\text{Y}_{1-x}\text{A}_x\text{MnO}_3$ ($\text{A} = \text{Ca}, \text{Sr}; x = 0, 0.1, 0.3, 0.5$) (YAMO) obtained by the solid-state reactions and discuss how the ionic size and doping level of A-element affect the magnetic properties and electronic structure of *h*-YMO.

3.2 Experiment

All the samples of $\text{Y}_{1-x}\text{A}_x\text{MnO}_3$ ($\text{A} = \text{Ca}, \text{Sr}; x = 0, 0.1, 0.3, 0.5$) were prepared by solid state reaction. Briefly, the nominal stoichiometry composition of Y_2O_3 (99.999%), MnCO_3 (99.95%), and CaCO_3 (99.95%) (or SrCO_3 (99.99%)) powders were ground and heated at 1300 °C. First, Y_2O_3 were preheated to 500°C for 5h to remove the adsorptive mist and the desired stoichiometric mixture of Y_2O_3 , MnCO_3 , CaCO_3 , and SrCO_3 were heated for 1300°C for 18h. The mixture was pressed and sintered at 1300 °C for 24 hours, then ground and pressed again for the subsequent sintering. After repeating the process for 3-4 times, it was pressed into disk for the final sintering carried out at 1300 °C for 24 hours. We compared the density of these bulks with that calculate from the ideal bulk that all form with unit cell without grain boundary of defeat. We broke these bulks, pressed and reheat until the density rate of the bulk had trends of slow down. This process usually cost two to three times. For future measurements referred below, parts of the bulk were ground to minute powders again. The crystalline structure, magnetization behaviors, and electronic structure of these samples were examined by x-ray

diffraction (XRD), Superconducting Quantum Interference Device (SQUID), and (XANES), respectively. The XANES spectra were collected by the fluorescence yield (FY) and total electron yield (TEY) mode with resolution of 0.15 eV.

3.3 Results AND Discussions

Figure 3.1 shows the XRD θ - 2θ scans of all the YAMO samples presented in this study. It is clear that the undoped YMnO_3 is of pure hexagonal structure. The Sr^{2+} -doped YMnO_3 also shows hexagonal structure for various doping levels, as well. Nevertheless, the structure of the $\text{Y}_{1-x}\text{Ca}_x\text{MnO}_3$ (YCMO) samples appears to change from the hexagonal structure for the undoped

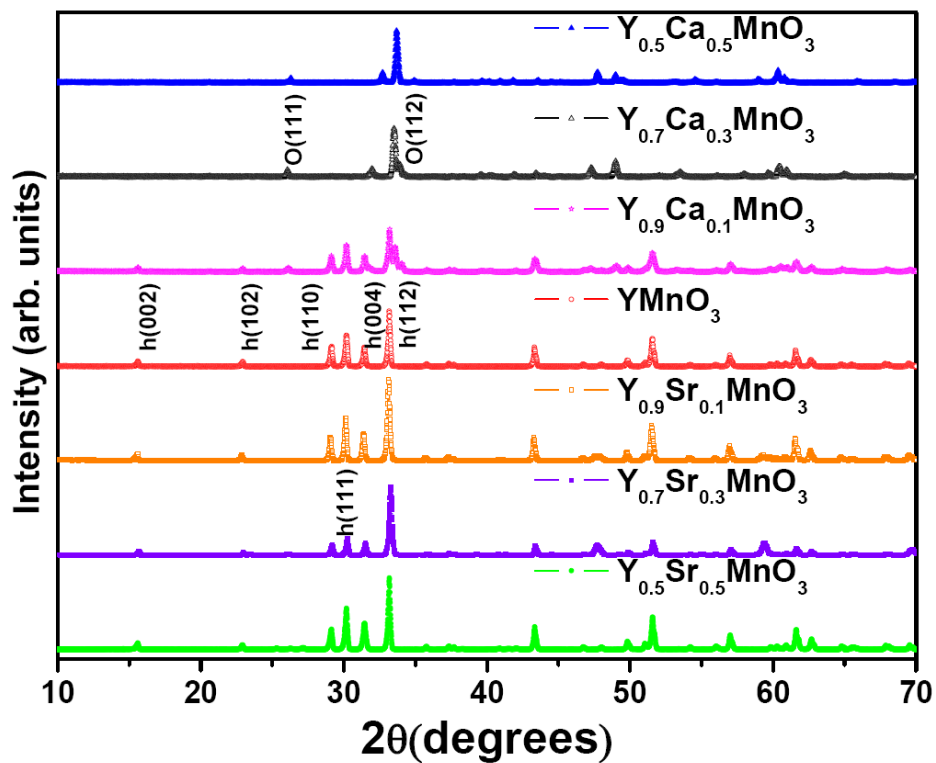


FIG. 3.1: The XRD patterns for a series YMnO_3 doped with Ca and Sr. Both pristine YMnO_3 and $\text{Y}_{1-x}\text{Sr}_x\text{MnO}_3$ samples show the same hexagonal crystal structure. The structure of $\text{Y}_{1-x}\text{Ca}_x\text{MnO}_3$ changes from hexagonal to orthorhombic with the increasing doping level of Ca^{2+} .

YMnO₃ and to a hexagonal-orthorhombic mixture for Y_{0.9}Ca_{0.1}MnO₃. When x = 0.3, the character of hexagonal structure becomes diminishingly insignificant and completely disappears when x = 0.5. This is quite surprising if one looks at the ionic size of Y³⁺, Ca²⁺, and Sr²⁺, which are 1.06 Å, 1.06 Å, and 1.27 Å, respectively. Thus one would expect a more dramatic effect from Sr-doping. If we further compare the stable crystal structure of YMnO₃, CaMnO₃, and, we can find that both YMnO₃ and SrMnO₃ have the hexagonal crystal structure, while CaMnO₃ is

Table 3.1 The fitted lattice constant of Y_{1-x}A_xMnO₃ (A = Ca, Sr; x= 0, 0.1, 0.3 , 0.5)serial powders

	Crystal Structure	Lattice Constant		
		a	b	c
YMnO ₃	hexagonal	6.13495		11.3846
Y _{0.9} Sr _{0.1} MnO ₃	hexagonal	6.13822		11.394
Y _{0.7} Sr _{0.3} MnO ₃	hexagonal	6.12742		11.3938
Y _{0.5} Sr _{0.5} MnO ₃	hexagonal	6.13482		11.386
SrMnO ₃ ^[a]	hexagonal	5.461		9.093
Y _{0.9} Ca _{0.1} MnO ₃	hexagonal	6.12658		11.3846
	with mixed orthorhombic	5.26903	5.61859	7.4056
Y _{0.7} Ca _{0.3} MnO ₃	orthorhombic	5.30054	5.61976	7.42975
Y _{0.5} Ca _{0.5} MnO ₃	orthorhombic	5.31172	5.55673	7.46505
CaMnO ₃ ^[b]	orthorhombic	5.2819	7.4547	5.2658
YMnO ₃ ^[c]	orthorhombic	5.2616	5.8444	7.3579

[a] The lattice constant of SrMnO₃. with hexagonal structure. [11]

[b] The lattice constant of CaMnO₃. with orthorhombic structure. [14]

[c] The lattice constant of YMnO₃. with orthorhombic structure. [15]

orthorhombic. It may explain why Sr-doping does not give rise to more significant effects on the crystal structure change, albeit of larger ionic size of Sr^{2+} . On the other hand, the fact that the $\text{Y}_{0.9}\text{Ca}_{0.1}\text{MnO}_3$ sample displays a mixture of hexagonal and orthorhombic phase structure indicates that either Ca does not dissolve into the *h*-YMO or the doping turns part of the *h*-YMO into *o*-YMO. Since the XRD shows all the peaks are corresponding to either *h*-YMO or *o*-YMO, it is more plausible to say the latter is being the case. In fact, Moure et al. reported that there is a structure transformation from *h*-YMO to *o*-YMO driven by Ca-doping when $x = 0.22$ [17]. This is also consistent with our results of $x = 0.3$ and $x = 0.5$, where the system has essentially turned into orthorhombic. Table 3.1 compares the calculated lattice parameters of our Ca-doped samples with that obtained by Laberty et al. [18] and Mathieu et al. [19]. In rare earth manganites, CaMnO_3 is a non-Jahn-Teller distorted compound with G-type AFM ordering. In principle, doping YMO with Ca^{2+} ions might ease the extent of lattice distortion caused by the Jahn-Teller effect. This is reflected in the lattice constants of orthorhombic YMnO_3 , Ca-doped YMnO_3 , and CaMnO_3 listed in Table 3.1 [14, 15, 18, 20].

Although we have indicated the reason that $\text{Y}_{1-x}\text{Sr}_x\text{MnO}_3$ remains hexagonal might be presumably due to both end compounds, YMnO_3 and SrMnO_3 , are having stable hexagonal crystal structure, there are still some subtle differences between them. SrMnO_3 belongs to space group $P6_3/mmc(194)$ and has a four layer ABAC stacking sequence of SrO_3 layer along the *c*-axis [11]. On the other hand, the space group of YMnO_3 is $P6_3cm(185)$ at room temperature and has a two layer AB stacking sequence along the *c*-axis. [21] As a result, the Mn-O-Mn bonding constructs the MnO_5 bipyramidal structure and the Mn ions lie on the *a*-*b* plane in hexagonal YMnO_3 , while in SrMnO_3 , the Mn-O bonding forms the MnO_6 octahedron typical for

perovskite manganites and the Mn ions lied on the stacked layers. Since the ionic size of Sr^{2+} is relatively larger than that of Y^{3+} and the crystal symmetries are not exactly the same, complete substitution appears not easy to accomplish. Nevertheless, the XRD results shown in Fig. 3.1 apparently does not display any noticeable effect from the Sr-doping even at the highest doping level of $x = 0.5$. In any case, we believe that independent checks should provide further evidence that might be helpful for drawing any conclusive remarks on these matters.

In order to check if the modification of the electronic state of Mn-ion by substituting Y with Ca and Sr is indeed relevant to the changes in crystal structure, we have performed extensive XANES measurements on all the samples. The Mn $L_{3,2}$ XANES of YMnO_3 , $\text{Y}_{1-x}\text{Ca}_x\text{MnO}_3$, and $\text{Y}_{1-x}\text{Sr}_x\text{MnO}_3$ ($x = 0.1, 0.3, 0.5$) are shown in Fig. 3.2, together with that obtained from standard manganese oxide powders with valence of Mn^{2+} (MnO), Mn^{3+} (Mn_2O_3), and Mn^{4+} (MnO_2). This practice has been widely used to characterize the light hole-doped YMnO_3 polycrystalline samples [6] as well as various manganites [7, 10]. As is evident from the results, the electronic structure $\text{Y}_{1-x}\text{Ca}_x\text{MnO}_3$ samples exhibit characteristics very similar to that of the Mn_2O_3 standard powders when $x = 0.1$, indicating that Mn ions are predominantly trivalent. But it becomes quite different when $x = 0.3$ and 0.5 . Namely, the main peak of Mn L_3 edge shifts to higher energy and exhibits characteristics similar to that of the $\text{La}_{1-x}\text{Ca}_x\text{MnO}_3$ system [10, 22]. In our case, the leading two peaks are separated by about 1.8 eV and 2.1 eV for $x = 0.3$ and $x = 0.5$, respectively. In any case, the spectra indicate that with Ca-doping the crystal structure of the parent YMO transforms from hexagonal to orthorhombic and is consistent with the XRD results shown in Fig. 3.1. In addition to indicating the conversion of MnO_5 bipyramids into MnO_6 octahedrons, the XANES spectra, being resembled to the hole-doped LaMnO_3 systems with similar MnO_6 octahedrons, also expound signatures of partially converting Mn^{3+}

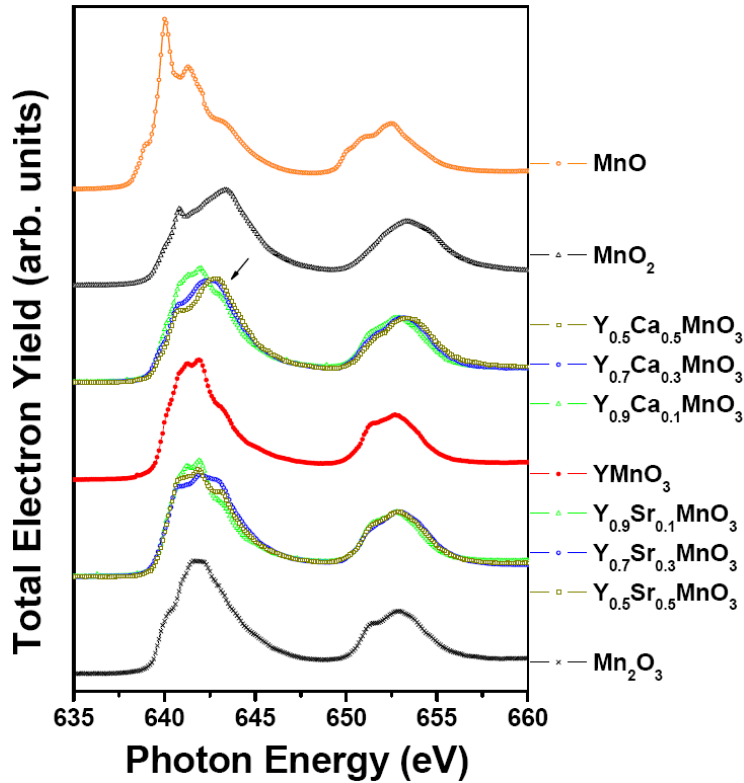


FIG. 3.2 The Mn L edge XANES spectra for MnO (standard powder), MnO₂ (standard powder), Y_{1-x}A_xMnO₃ (A = Ca, Sr ; x = 0, 0.1, 0.3, 0.5) polycrystalline samples, and Mn₂O₃ (standard powder). Data presented in order from top to bottom.

into Mn⁴⁺ for balancing the chemical neutrality when doping Ca²⁺ ions into YMnO₃ [10, 22-24].

On the other hand, the Mn-L₃ XANES spectra of Y_{1-x}Sr_xMnO₃ displays a shoulder (as indicated by the arrow on the spectra) at the right hand side of the first main peak, which increases with the increasing doping level of Sr and eventually develops into a minor characteristic peak at the expense of the spectral weight of the original minor peak by converting it into a clear shoulder. Although due to the marked ionic size difference Sr²⁺ should not be able to replacing Y³⁺ easily, nevertheless, we could still see the enhancement of Mn²⁺ states induced by Sr²⁺ doping in the XANES spectra of Y_{1-x}Sr_xMnO₃, except for x = 0.5 in that the spectrum seems to exhibit mixed features of hexagonal Mn³⁺/Mn⁴⁺ (MnO₅) and

orthorhombic Mn^{4+} (MnO_6). We note that there indeed exist few undefined weak peaks in the $x = 0.5$ diffraction spectrum of Fig. 3.1, indicating that the sample may consist of mixed phases.

Fig. 3.3 shows the O K edge total electron yield XANES spectra for undoped, Ca-doped, and Sr-doped samples discussed in Fig. 3.2. For YMnO_3 , Asokan et al. argued that the peaks appearing in the spectra can be assigned into four groups (A, B, C, D). In their classification, the first 3 peaks (A_1, A_2, A_3) were assigned as group A and the subsequent 2 peaks (B_1, B_2) were termed as group B. Group C consists of only a peak, and the final 2 peaks (D_1, D_2) are referred

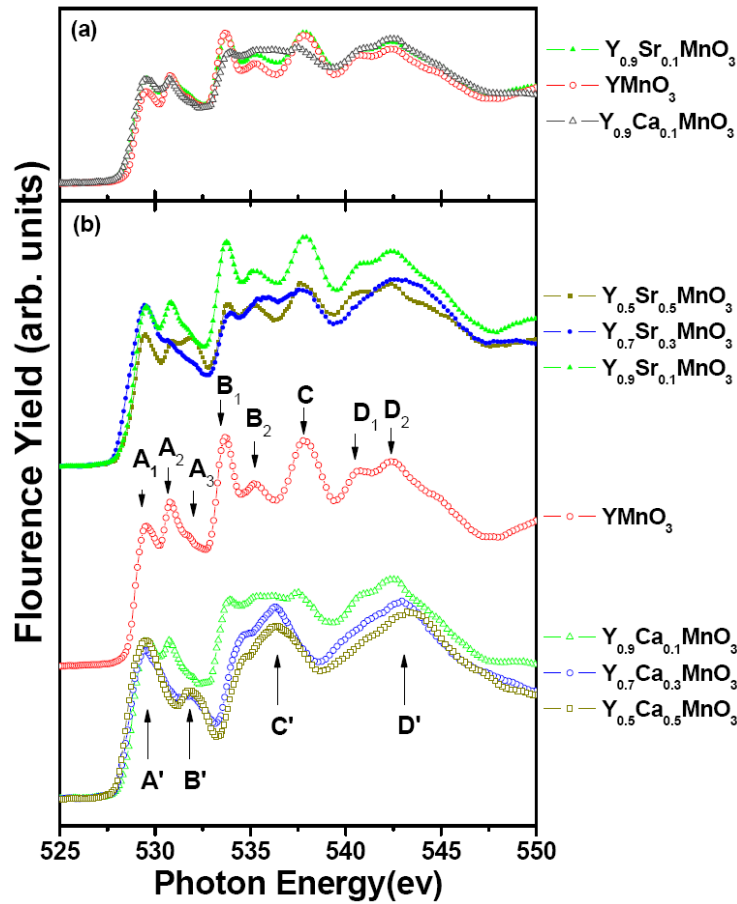


FIG. 3.3: (a) The O K edge XANES spectra in order of $\text{Y}_{0.9}\text{Sr}_{0.1}\text{MnO}_3$, YMnO_3 , and $\text{Y}_{0.9}\text{Ca}_{0.1}\text{MnO}_3$ used for compare the light doped difference. (b) The O K edge XANES spectra in order of $\text{Y}_{1-x}\text{Sr}_x\text{MnO}_3$ series, intrinsic YMnO_3 , and $\text{Y}_{1-x}\text{Ca}_x\text{MnO}_3$ series (for $x = 0.1, 0.3, 0.5$) from top to bottom.

as group D. These groups are associated with transitions between O 2p-Mn 3d states and correspond to the e_1 , e_2 , and a_1 bands, O 2p-Y 3d states (group C), and O 2p-Mn 4sp hybridization (group D) around 530~535, 538, and 543eV, respectively. Recently, the assignments were revised by Cho et al. [25] using the polarization dependent x-ray absorption spectroscopy on the hexagonal YMnO₃ single crystal to combine with the cluster model calculation including the configuration interaction. In their assignment, the first four leading features at the beginning O K-edge around 528~532 eV were attributed to $a_{1g}(z^2\uparrow)$, $e_{1g}(yz\downarrow/zx\downarrow)$, $e_{2g}(xy\downarrow/x^2-y^2\downarrow)$, and $a_{1g}(z^2\downarrow)$ ordered with the increasing energy. These bands were ascribed to Mn 3d-O 2p hybridized states in MnO₅ bipyramidal structure. The next three features around 532~539eV were attributed to the contribution of the Y 4d-O 2p hybridized states and they were assigned to a doublet e_g^π , singlet a_{1g} , and a doublet e_g^σ orbital. Finally, the features in the range of 539~548 eV were contributed by oxygen hybridized Mn 4sp/Y 5sp states. However, due to the modified distortion in MnO₅ bipyramids, some modifications in the electronic structures of the real materials are expected. The observation of the fine and distinguishable peaks A₁, A₂, and A₃ in undoped YMO being merged into two broad ones in Ca-doped YMO (A and B) and the peaks B1, B2, and C of the former being merged into broad one (C') in the latter, is exactly a manifestation of the hexagonal to orthorhombic structure change induced electronic modifications as has been ubiquitously seen in the LaMnO₃ series [6, 10, 22, 23].

In contrast, the XANES of the undoped YMnO₃ and Y_{0.9}Sr_{0.1}MnO₃ showed very similar features, except for a slightly broadened B₂, which is consistent with the fact that both samples are remaining hexagonal as shown in XRD results. It is clear that in this case the ground state configuration of the Mn³⁺ d⁴ orbital is $e_{1g}^2 e_{2g}^2$. With the Sr²⁺ substitution for Y³⁺, features of the mixed Mn³⁺/Mn⁴⁺ should be observed. Moreover, the effect should become more pronounced as

the doping level is increased, since the ground state configurations of $Mn^{4+} 3d^4$ are $e_{1g}^1 e_{2g}^2$ and $e_g^1 t_{2g}^2$ for MnO_5 and MnO_6 structure, respectively. Finally, there should also exist additional unoccupied state $e_{1g}\uparrow$ with increasing x giving rise to an increasing intensity of A_1 , a peak consists of contributions mainly from the unoccupied a_{1g} and e_{1g} bands. The intensity of peak B_1 , and C is suppressed and blurred with B_2 to form a broadened peak C' when Y^{3+} is replaced by Ca . It is interesting to note that in the spectrum of $Y_{0.7}Sr_{0.3}MnO_3$, the feature of the e_{2g} (A_2) state of MnO_5 diminishes without accompanying emergence of the t_{2g} (B) band featuring MnO_6 . This implies that substitution of Y^{3+} by Sr^{2+} may have demolished the e_{2g} state in hexagonal $Y_{0.7}Sr_{0.3}MnO_3$, albeit only minute differences in the lattice parameters were recorded in Table 3.1. Unfortunately, for $Y_{0.5}Sr_{0.5}MnO_3$ the tendency is not well followed presumably due to the formation of some second phases. Indeed, we note that the drastic enhancement in the intensity of peak A_3 , indicating the emergence of the t_{2g} bands associated with the MnO_6 perovskite structure as seen in Ca -doped $YMnO_3$. It appears that, in $Y_{1-x}Sr_xMnO_3$ series for $x=0.1$ and 0.3 , a mixed MnO_5/MnO_6 state originated from the hexagonal $YMnO_3$ and $SrMnO_3$ compounds. The current results further suggest that the electronic structure may have played a more important role than the ionic size effect in determining the crystal structure as has been argued by Agüero et al. [26]. The underlying mechanism for this peculiar behavior and the corresponding effect on ferroelectricity, however, requires further studies.

Next, we turn to the preliminary magnetic properties of the polycrystalline $Y_{1-x}A_xMnO_3$ samples by showing the temperature dependent susceptibility ($\chi(T)$) in Fig. 3.4. The $\chi(T)$ responses were measured by SQUID with an external field of 100 Oe. Fig. 3.4(a) shows the zero field cool (ZFC) and field cool (FC) $\chi(T)$ data of the undoped hexagonal $YMnO_3$ powder. It is clear that there are two magnetic phase transitions occurring around 74 K and 44 K, respectively.

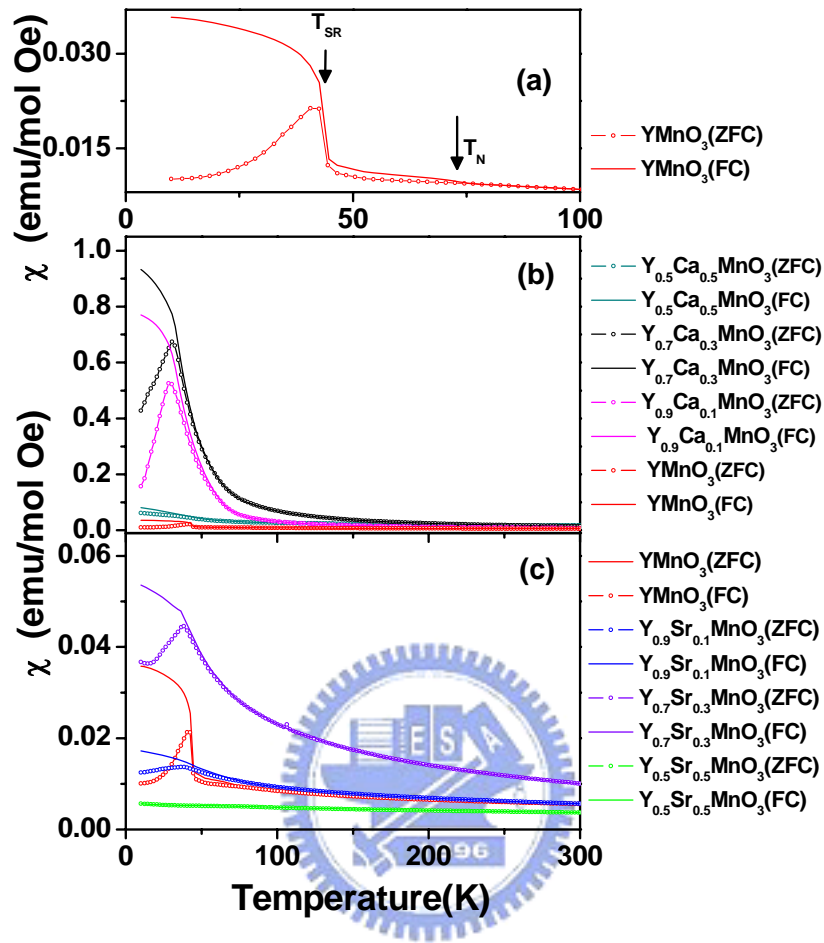


FIG. 3.4: Temperature dependence of susceptibility for serial powders measured by ZFC and FC method with an applied field 100 Oe, (a) intrinsic YMnO_3 polycrystalline powders, (b) $\text{Y}_{1-x}\text{Ca}_x\text{MnO}_3$ ($x = 0, 0.1, 0.3, 0.5$) polycrystalline powders (c) $\text{Y}_{1-x}\text{Sr}_x\text{MnO}_3$ ($x = 0, 0.1, 0.3, 0.5$) polycrystalline powders.

Furthermore, the 44 K transition shows an order of magnitude enhancement in the susceptibility and appears to exhibit a spin-glass-like behavior. We note that this observation probably is the first to show the two transitions simultaneously in polycrystalline samples with such distinct features. Previously, the majority of the $\chi(T)$ measurements performed on YMO single crystals usually displayed only an AFM transition around 70-80 K [[27] & refs.], while for polycrystalline powders or films only a so-called spin reorientation occurring around 40 K was

observed. As a result, the 40 K transition has been usually interpreted as the intrinsic AFM transition which is somehow suppressed by the crystal disorders. Veres et al. [28], though have also indicated in their temperature-dependent magnetization ($M(T)$) data a similar Neel temperature ($T_N = 70\text{K}$) and spin reordering temperature ($T_{SR} = 40\text{K}$), the definition was not as convincing as the present data. For instance, they defined T_N as the point where the ZFC $M(T)$ curve deviates from the FC one and interpreted the T_{SR} as might be induced by some traced orthorhombic phase that is not discernible in XRD results. On the other hand, Chen et al. [28, 29] attributed the 42 K magnetic transition in a Mn-rich YMnO_3 sample to the re-entrant spin glass transition caused by $\text{Mn}^{2+}/\text{Mn}^{3+}$ mixed states. However, since in our XANES spectra Mn L-edge for the YMnO_3 there was no signature of Mn^{2+} observed, other origins should be considered. In fact, as pointed out by Sharma et al. [16] for geometrically frustrated systems such as YMO the ground state magnetic structure remains as highly degenerated low lying states even below the Neel temperature. Thus, in single crystals the intrinsic spin reorientation of Mn moments occurring around 40 K is barely discernible in the $\chi(T)$ measurements. This degeneracy, however, might be easily lifted by the disorders existent in the polycrystalline powders or films, resulting in short range weak ferromagnetism and the spin-glass-like behaviors manifested in $\chi(T)$ measurements. In order to clarify that there indeed exists a weak ferromagnetism below the spin reorientation temperature, we show in Fig. 3.5 the field dependent magnetization ($M-H$) curves taken at three different temperatures. As seen in Fig. 3.5, an apparent hysteresis typical for weak ferromagnetism spin-glass system is evident at $T = 30\text{ K}$. In contrast, when the temperature is above 40 K, although the system is in AFM state, there is no hysteresis in $M-H$ curves observed.

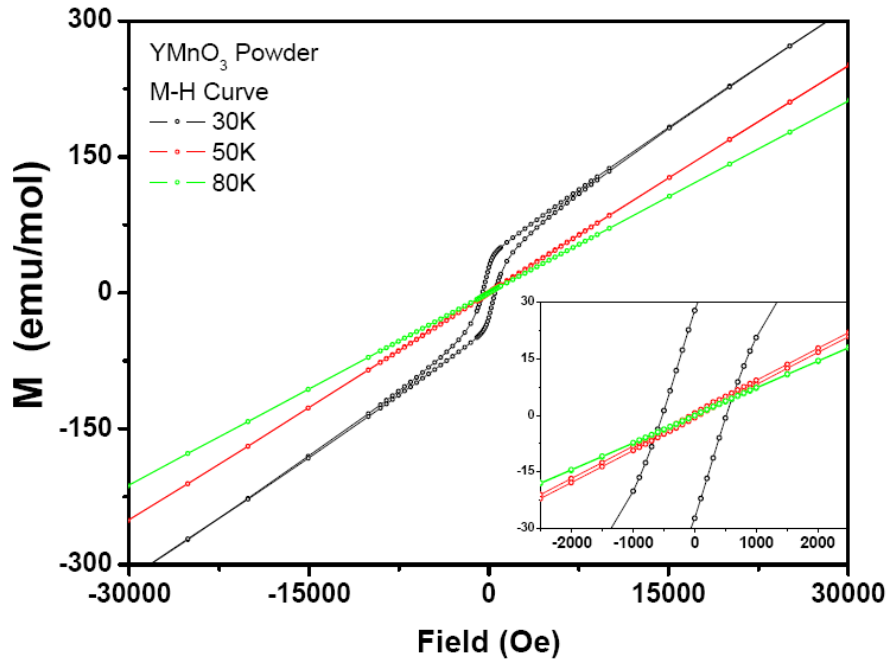


FIG. 3.5: Field dependent magnetization (M - H) curves taken at three different temperatures. The data were collected at 30K, 50K, and 80K respectively.

Fig. 3.4(b) and 3.4(c) displays the similar ZFC and FC $\chi(T)$ measurements performed respectively on the $Y_{1-x}Ca_xMnO_3$ and $Y_{1-x}Sr_xMnO_3$ samples investigated. In each panel, the results for undoped YMO shown in Fig. 3.4(a) are also displayed for comparison. It is clear that for $Y_{1-x}Ca_xMnO_3$, although the spin reorientation temperature was reduced from 40 K to about 30 K when $x = 0.1$ and $x = 0.3$, there is a marked enhancement (about 30 times) in the magnetic susceptibility. As has been discussed above, the orthorhombic structure emerges immediately after Ca-doping. Thus, this might be due to the enhanced double exchange by driving the crystal into the orthorhombic structure, which, in turn, might have enhanced the short range ferromagnetic (FM) ordering. In order to confirm the conjecture of AFM to FM interaction driving by crystal structure transformation, we fit the data to obtain that the Weiss temperature (T_W) is indeed varied from $T_W = -285$ K for $x = 0$, to $T_W = 27$ K and 54 K for $x = 0.1$ and $x = 0.3$,

respectively. We note that Iliev et al. [30] have indicated that there exists a transition from AFM superexchange to FM double exchange interaction for Ca doping concentration exceeds 8% in orthorhombic $YMnO_3$ prepared by high pressure, high temperature synthesis. For $x = 0.5$, the ZFC $\chi(T)$ becomes featureless, presumably due to disruption of any magnetic ordering. On the contrary, for the $Y_{1-x}Sr_xMnO_3$ samples, only the $x = 0.1$ sample shows a mild enhancement in susceptibility and the transition rapidly becomes smeared with increasing Sr doping. With 50% doping of Sr, the two magnetic transitions appear to disappear altogether. It is not clear at present why Sr-doping is so detrimental to the magnetic ordering of the system, despite that it apparently does not change the crystal structure significantly. In fact similar analyses on the Weiss temperature indicate that $T_w = -222$ K and -56 K for 10 % and 30 % Sr-doping, respectively, suggesting that Sr-doping not only does not activate the FM double exchange but also significantly suppressed the AFM superexchange interaction.



3.4 Summary

In summary, we have prepared a series of $Y_{1-x}A_xMnO_3$ ($A = Ca, Sr ; x = 0, 0.1, 0.3, 0.5$) samples to systematically investigate how the ionic size of the divalent dopants alters the interplays between the crystal structure, magnetic properties, and the electronic structures of the rare earth multiferroic manganites. The results indicate that, in undoped $YMnO_3$, in addition to the 70 K antiferromagnetic transition, a weak ferromagnetism manifested with typical spin-glass-like behaviors emerges around 40 K. This transition is believed to arise from the coupling between the crystal disorder and the intrinsic spin reorientation, which evidently lifts the degeneracy of the low lying states and forms short range ordered ferromagnetic clusters. Ca-doping apparently drives the hexagonal $YMnO_3$ into orthorhombic structure and activates

the ferromagnetic double exchange interaction to give rise a more than 30 times enhancement in the magnetic susceptibility as well as significant spin-glass-like transition around 30 K. On the other hand, Sr-doping does not drive the change in crystal structure of YMnO_3 . As a result, the disorder not only does not activate any ferromagnetic coupling but also weakens the superexchange interaction, resulting in a severely smeared spin reorientation transition. These observations are somewhat counter-intuition and thus intriguing, since the ionic size difference is much larger between Sr^{2+} and Y^{3+} as compared to that between Ca^{2+} and Y^{3+} ions.



References

- [1] W. Prellier, M.P. Singh, P. Murugavel, *Journal of Physics-Condensed Matter*. 17 (2005) R803-R832.
- [2] M. Fiebig, T. Lottermoser, D. Frohlich, A.V. Goitsev, R.V. Pisarev, *Nature*. 419 (2002) 818-820.
- [3] A.B. Souchkov, J.R. Simpson, M. Quijada, H. Ishibashi, N. Hur, J.S. Ahn, S.W. Cheong, A.J. Millis, H.D. Drew, *Physical Review Letters*. 91 (2003) 027203.
- [4] T. Lottermoser, T. Lonkai, U. Amann, D. Hohlwein, J. Ihringer, M. Fiebig, *Nature*. 430 (2004) 541-544.
- [5] B.B. Van Aken, T.T.M. Palstra, A. Filippetti, N.A. Spaldin, *Nature Materials*. 3 (2004) 164-170.
- [6] K. Asokan, C.L. Dong, C.W. Bao, H.M. Tsai, J.W. Chiou, C.L. Chang, W.F. Pong, P. Duran, C. Moure, O. Pena, *Solid State Communications*. 134 (2005) 821-826.
- [7] J.S. Kang, S.W. Han, J.G. Park, S.C. Wi, S.S. Lee, G. Kim, H.J. Song, H.J. Shin, W. Jo, B.I. Min, *Physical Review B*. 71 (2005) 092405.
- [8] N. Hur, S. Park, P.A. Sharma, J.S. Ahn, S. Guha, S.W. Cheong, *Nature*. 429 (2004) 392-395.
- [9] S.F. Chen, W.J. Chang, S.J. Liu, J.Y. Juang, J.Y. Lin, K.H. Wu, T.M. Uen, Y.S. Gou, *Physica B-Condensed Matter*. 336 (2003) 267-274.
- [10] W.J. Chang, J.Y. Tsai, H.T. Jeng, J.Y. Lin, K.Y.J. Zhang, H.L. Liu, J.M. Lee, J.M. Chen, K.H. Wu, T.M. Uen, Y.S. Gou, J.Y. Juang, *Physical Review B*. 72 (2005) 132410.
- [11] A. Daoud-Aladine, C. Martin, L.C. Chapon, M. Hervieu, K.S. Knight, M. Brunelli, P.G. Radaelli, *Physical Review B*. 75 (2007) 104417.
- [12] B. Lorenz, A.P. Litvinchuk, M.M. Gospodinov, C.W. Chu, *Physical Review Letters*. 92 (2004) 087204.

- [13] B. Lorenz, F. Yen, M.M. Gospodinov, C.W. Chu, *Physical Review B*. 71 (2005) 014438.
- [14] H. Taguchi, M. Sonoda, M. Nagao, *Journal of Solid State Chemistry*. 137 (1998) 82-86.
- [15] M.N. Iliev, M.V. Abrashev, H.G. Lee, V.N. Popov, Y.Y. Sun, C. Thomsen, R.L. Meng, C.W. Chu, *Physical Review B*. 57 (1998) 2872-2877.
- [16] P.A. Sharma, J.S. Ahn, N. Hur, S. Park, S.B. Kim, S. Lee, J.G. Park, S. Guha, S.W. Cheong, *Physical Review Letters*. 93 (2004) 177202.
- [17] C. Moure, M. Villegas, J.F. Fernandez, J. Tartaj, P. Duran, *Journal of Materials Science*. 34 (1999) 2565-2568.
- [18] C. Laberty, A. Navrotsky, C.N.R. Rao, P. Alphonse, *Journal of Solid State Chemistry*. 145 (1999) 77-87.
- [19] R. Mathieu, P. Nordblad, D.N.H. Nam, N.X. Phuc, N.V. Khiem, *Physical Review B*. 63 (2001) 174405.
- [20] H. Aliaga, M.T. Causa, M. Tovar, A. Butera, B. Alascio, D. Vega, G. Leyva, G. Polla, P. Konig, *Journal of Physics-Condensed Matter*. 15 (2003) 249-258.
- [21] T. Asaka, K. Nemoto, K. Kimoto, T. Arima, Y. Matsui, *Physical Review B*. 71 (2005) 014114.
- [22] K. Asokan, J.C. Jan, K.V.R. Rao, J.W. Chiou, H.M. Tsai, S. Mookerjee, W.F. Pong, M.H. Tsai, R. Kumar, S. Husain, J.P. Srivastava, *Journal of Physics-Condensed Matter*. 16 (2004) 3791-3799.
- [23] M. Abbate, F.M.F. de Groot, J.C. Fuggle, A. Fujimori, O. Strebel, F. Lopez, M. Domke, G. Kaindl, G.A. Sawatzky, M. Takano, Y. Takeda, H. Eisaki, S. Uchida, *Physical Review B*. 46 (1992) 4511.
- [24] H.J. Lee, G. Kim, J.S. Kang, B. Dabrowski, S.W. Han, S.S. Lee, C. Hwang, M.C. Jung, H.J. Shin, H.G. Lee, J.Y. Kim, B.I. Min, *Journal of Applied Physics*. 101 (2007) 09g523.

- [25] D.Y. Cho, J.Y. Kim, B.G. Park, K.J. Rho, J.H. Park, H.J. Noh, B.J. Kim, S.J. Oh, H.M. Park, J.S. Ahn, H. Ishibashi, S.W. Cheong, J.H. Lee, P. Murugavel, T.W. Noh, A. Tanaka, T. Jo, *Physical Review Letters*. 98 (2007) 217601.
- [26] O. Aguero, A.G. Leyva, P. Konig, D. Vega, G. Polla, H. Aliaga, M.T. Causa, *Physica B-Condensed Matter*. 320 (2002) 47-50.
- [27] Z.J. Huang, Y. Cao, Y.Y. Sun, Y.Y. Xue, C.W. Chu, *Physical Review B*. 56 (1997) 2623-2626.
- [28] A. Veres, J.G. Noudem, S. Fourrez, G. Bailleul, *Solid State Sciences*. 8 (2006) 137-141.
- [29] W.R. Chen, F.C. Zhang, J. Miao, B. Xu, X.L. Dong, L.X. Cao, X.G. Qiu, B.R. Zhao, P.C. Dai, *Applied Physics Letters*. 87 (2005) 042508.
- [30] M.N. Iliev, B. Lorenz, A.P. Litvinchuk, Y.Q. Wang, Y.Y. Sun, C.W. Chu, *Journal of Physics-Condensed Matter*. 17 (2005) 3333-3341.



Chapter 4

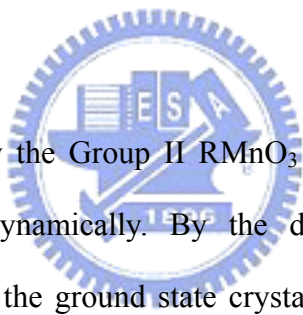
Structure stabilization and magnetic behaviors of hexagonal YMnO₃ thin films

In Chapter 3, we have discussed the effect of Ca²⁺ ion-doping in driving the hexagonal YMnO₃ into the metastable perovskite structure as well as the associated changes in the magnetic and electronic structures of the system. When the trivalent manganese is partially substituted by the quadrivalent manganese induced by divalent Ca-doping, since the ionic size of Mn⁴⁺ was smaller than Mn³⁺, the tolerance factor becomes larger and the orthorhombic crystal structure is stabilized. Within the framework of the double exchange model, the mixed-valence state of the manganese may lead to ferromagnetic and metallic phase, similar to the alkaline-earth metal doped LaMnO₃ colossal magnetoresistance manganites [1, 2]. The metallic behavior, however, will inevitably counteract the charge localization needed to induce electric polarization. As a result, although Ca-doped can stabilize the rare-earth manganites with the perovskite structure, the accompanied metallic characteristics may simultaneously destroy the electric dipole moment and lose the multiferroicity of interest.

In this chapter and the following Chapter 5, we will try to develop other viable processes for stabilizing crystal structure. Orthorhombic Group II RMnO₃ compounds have been usually obtained through high temperature, high pressure synthesis processes (30 kbar at 1010 °C for 3 h, or at 960 °C for 4 h) [4] and the critical environment is to provide the tremendous strain needed to give rise the required structural transition. The

strong epitaxial strain due to the lattice mismatch between film and substrate frequently obtained in thin film deposition process thus provides an alternative route of stabilizing desired crystal structure by choosing the proper substrates. In chapter 4, we will present the deposition process in preparing hexagonal structural thin films and investigate the anisotropic magnetic behaviors utilizing the well-oriented films obtained. In chapter 5, we will go a step further trying to stabilize the orthorhombic structure from a hexagonal parent compound by choosing suitable substrates for deposition. The correspondent electronic and magnetic properties of a same compound with different crystal structure will then be studied and compared in detail.

4.1 Introduction



It is interesting that why the Group II RMnO₃ compounds are favor to form the hexagonal structure thermodynamically. By the definition of the tolerance factor frequently used in discussing the ground state crystal structure of AMnO₃ compounds, when the tolerance factor $t = 1$, it means the system favors to form a closest pack cubic structure like SrTiO₃. With the variation of the ionic size, the crystal structure starts to deform into orthorhombic one for smaller A-site ions. This simultaneously leads to larger moving displacements for the A-site ions. As the ionic size of the A-site ions gets smaller and smaller, the perovskite-like structure can no longer be stabilized and the materials eventually transform into the hexagonal structure, like hexagonal YMnO₃ and HoMnO₃. The hexagonal YMnO₃ (h-YMO) has ferroelectric transition at high temperature (900 K) and antiferromagnetic ordering Neel temperature (~ 70 K). The ferroelectric polarization was about $5.6 \mu C/cm^2$, and it was induced by the Y³⁺ displacement in YO₈ structure along c-axis. As indicated in the previous chapter, there were evidences that there might

be some interesting coupling between the two order parameters. Thus it is interesting to conduct more detailed studies on this material. In this chapter we present results on the preparation of hexagonal thin films obtained by pulsed laser deposition (PLD). The relation between thin film and substrate and the anisotropic magnetic behaviors are discussed.

4.2 Experiment

In Table 4.1, we compare the lattice mismatch between various substrates and hexagonal YMnO₃. From the comparison, it seems that YSZ and MgO substrate are having the least mismatch in thin film deposition process. Depositing on YSZ substrate will have the tensile strain with the mismatch value ~2.7% while depositing on MgO substrate will result in the compressive strain with the mismatch value ~2.4%. We used the YSZ substrate for preparing better crystallized hexagonal YMnO₃ thin film here, and the YMnO₃ thin film will be used to characterize the electronic characteristics with the MnO₅ bipyramid and will be presented in Chapter 5.

Table 4.1 The lattice constant of hexagonal YMnO₃ and several substrates. The in-plane lattice constant was showed for YSZ(111), MgO(111), and Al₂O₃(001) plane in depositing hexagonal YMnO₃(001) thin film.

	lattice constant			
	a	b	c	in-plane lattice constant
Hexagonal YMnO ₃ ^[a]	6.139	6.139	11.407	6.139
YSZ substrate	5.147	5.147	5.147	6.304
MgO substrate	4.236	4.236	4.236	5.990
Al ₂ O ₃ substrate	4.759	4.759	12.992	4.759

[a] The lattice constant of hexagonal YMnO₃. [3]

The hexagonal YMnO_3 bulk presented in Chapter 3 was used as the target for depositing YMO films on YSZ(111) substrates by pulse laser deposition (PLD) technique [5]. Fig. 4.1 shows the schematic illustration of our pulsed laser deposition system. The vacuum chamber was evacuated to reach a base pressure below 1×10^{-6} torr with a turbomolecular pumping station. The incident laser beam with an incident angle of 45° was focused to a small spot size about $1.5 \times 1.5 \text{ mm}^2$ on the bulk. In order to tune the

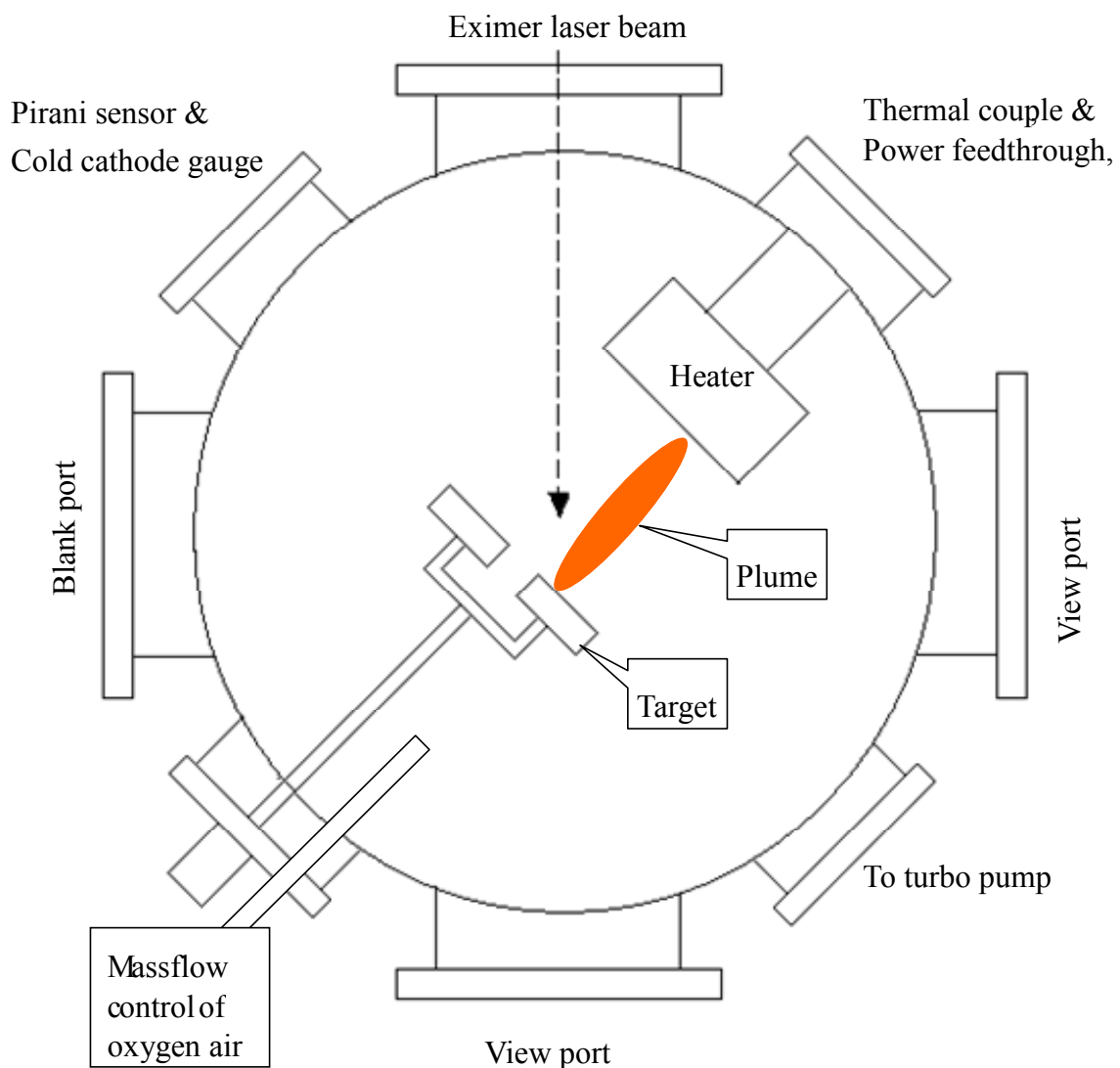


Fig. 4.1 The illustration of pulsed laser vacuum deposition system

optimum conditions, the KrF excimer laser with a wavelength of 248nm was operated at a repetition rate of 1~10 Hz with energy density ranging between 2-5 J/cm². The target was attached on a home-made brushless DC motor, and it was parallel to the substrate with a fixed distance ~5cm. The rotating target could avoid the digging craters on the bulk surface in the laser ablation process which may modify the composition in the ejected plume and hence that of the film. In order to prepare thin films with good crystalline quality, the substrate temperature (T_s) was varied from 700 °C to 880 °C (limited by the heater) with the oxygen partial pressure being controlled between background pressure (10^{-6} torr) and 0.3 torr during deposition. The film thickness was controlled between 180-250 nm.

The structures of the films were characterized by x-ray diffraction (XRD) θ - 2θ and Φ scans. The temperature dependent magnetic susceptibility ($\chi(T)$) along various principal crystalline axes was measured in a Quantum Design® superconducting quantum interference device (SQUID) with a small applied magnetic field to delineate the possible magnetism anisotropy in this material.

4.3 Results and Discussions

Fig. 4.2 showed the XRD θ - 2θ patterns of the YMO films deposited at different substrate temperatures (T_s) on single crystalline YSZ(111) substrates. The data clearly reveal that the hexagonal phase of YMO films is obtained when $T_s \geq 750$ °C. It is also evident that the crystalline quality is progressively improved with increasing T_s . The intensity of h-YMO(00 ℓ) peak was increased at higher temperature and reached the maximum when $T_s = 880$ °C. (The temperature of 880°C was restricted by the heater limit.) This deposition condition was set as the optimal condition in depositing *h*-YMO

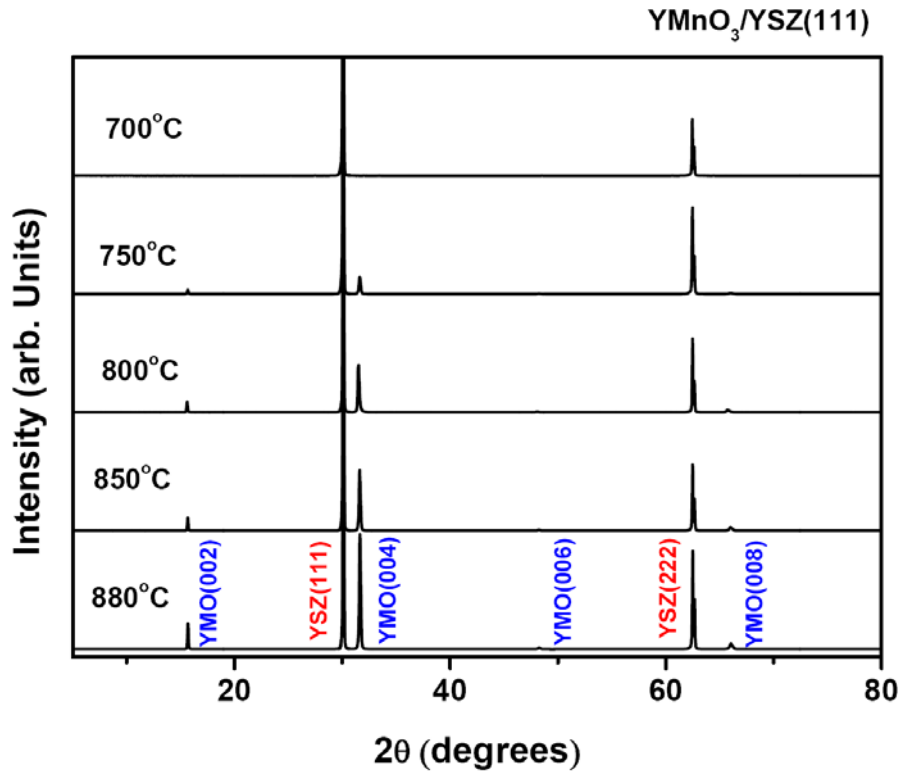


Fig. 4.2 The XRD θ - 2θ patterns of hexagonal YMnO_3 thin films grown on $\text{YSZ}(111)$ substrates as a function of the deposition temperature. All films were controlled to have the same thickness (180 nm) and an optimum oxygen partial pressure of 0.1 torr to delineate the relation between temperature and the degree of crystallization in the deposition process.

on YSZ substrate. Further experiments on the magnetic behavior and electronic structure to be presented in Chapter 5 are all obtained from films deposited at $T_s = 880^\circ\text{C}$.

In Fig. 4.3, a schematic drawing of the in-plane atomic arrangement between h - YMO thin film (right side) and YSZ substrates (left side) is shown. The YSZ substrate is vividly reflecting the yttrium stabilized zirconium oxide with the composition of 9 % Y and 91 % Zr. Y atoms and Zr atoms locate at the same site in the YSZ compositions. The Mn ions were hidden behind the Y or O ions and cannot be explicitly displayed in the figure. It is seen that the Y site in h - $\text{YMO}(001)$ plane is corresponding to the site symmetry of Y/Zr in the $\text{YSZ}(111)$ plane view. The figure shows the top view of YSZ

(111) plane and h -YMO(001) thin films, illustrating that $YSZ[\frac{2}{3}, \frac{-1}{3}, \frac{-1}{3}]$ is parallel to h -YMO[1,0,0]. The distance between the neighboring positive ions (Y or Zr) along $YSZ[\frac{2}{3}, \frac{-1}{3}, \frac{-1}{3}]$ is 6.304Å, and that between the neighboring positive ions (Y) along hexagonal YMO a -axis is 6.139Å. The lattice mismatch between the in-plane YSZ(111) and the a -axis of h -YMO is about 2.69% (tensile). On the other hand, as revealed in the

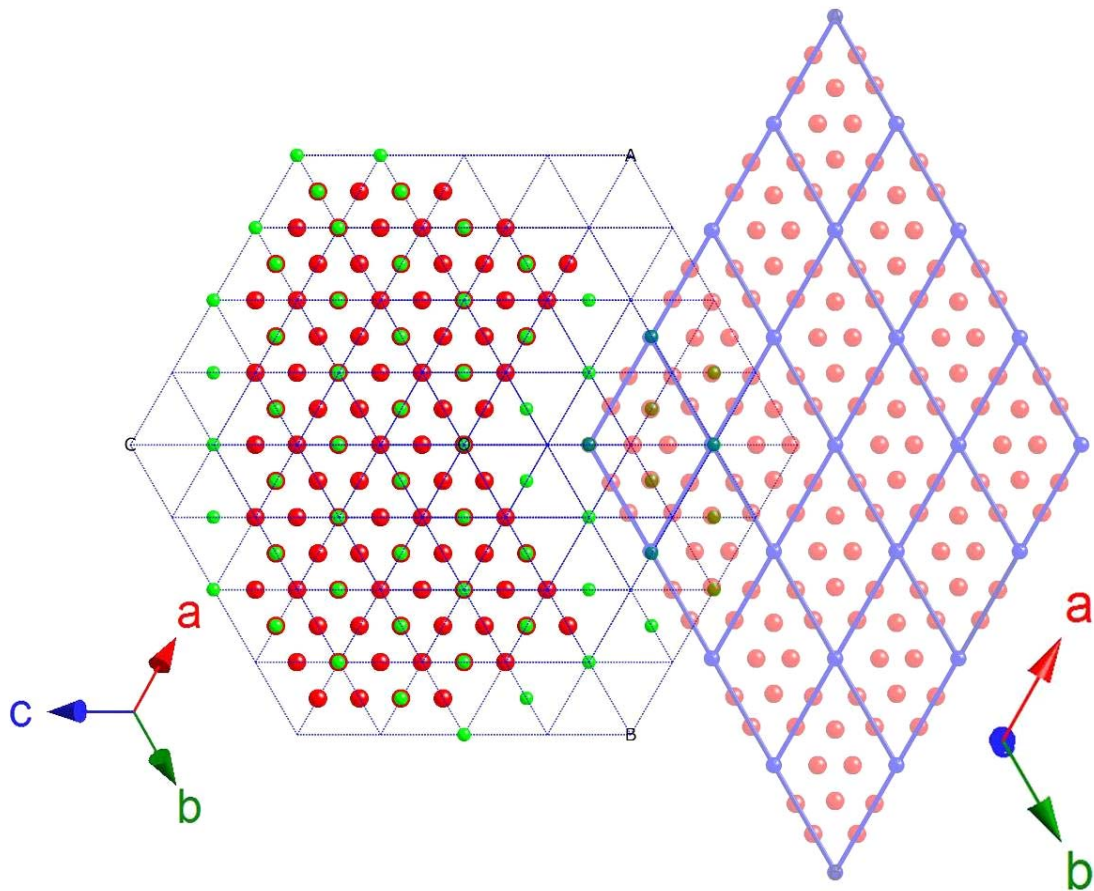


Fig. 4.3 The schematics showing the in-plane atomic arrangements between the h -YMO thin films and YSZ substrates. The left hand side shows the top view along the YSZ(111) plane. The green balls indicate the site of Y or Zr ions, and red ball indicate the site of oxygen ions. The right hand side shows the top view along h -YMO(001) plane, the transparent blue balls indicate the Y ions in h -YMO, and transparent red balls indicate the oxygen ions in h -YMO. The wide transparent blue lines describe the unit cell of h -YMO.

XRD Φ -scans shown in Fig. 4.4, a six-fold symmetry is observed. In addition the well-alignment between the film and substrate, it is also noted that the Φ -scans of the (112) peak of the h -YMO films located at . To estimate the strain effect, we fit several diffraction peaks from the h -YMO(00 ℓ)/YSZ(111) films by Φ -scans and obtained $a = 6.177\text{\AA}$ and $c = 11.347\text{\AA}$. The lattice constant a expands by about 0.68% and the full width half maximum (FWHM) of the rocking curve was about 0.54° which has a relative lower value than that of h -YMO/ $\text{Al}_2\text{O}_3(001)$ films (FWHM $\sim 1.14^\circ$), presumably due to the larger film/substrate mismatch. We note that previous works by C. F. Tsai and Y. U. Lee show that h -YMO(00 ℓ) films can also be obtained using MgO(001) and MgO(111) substrates.

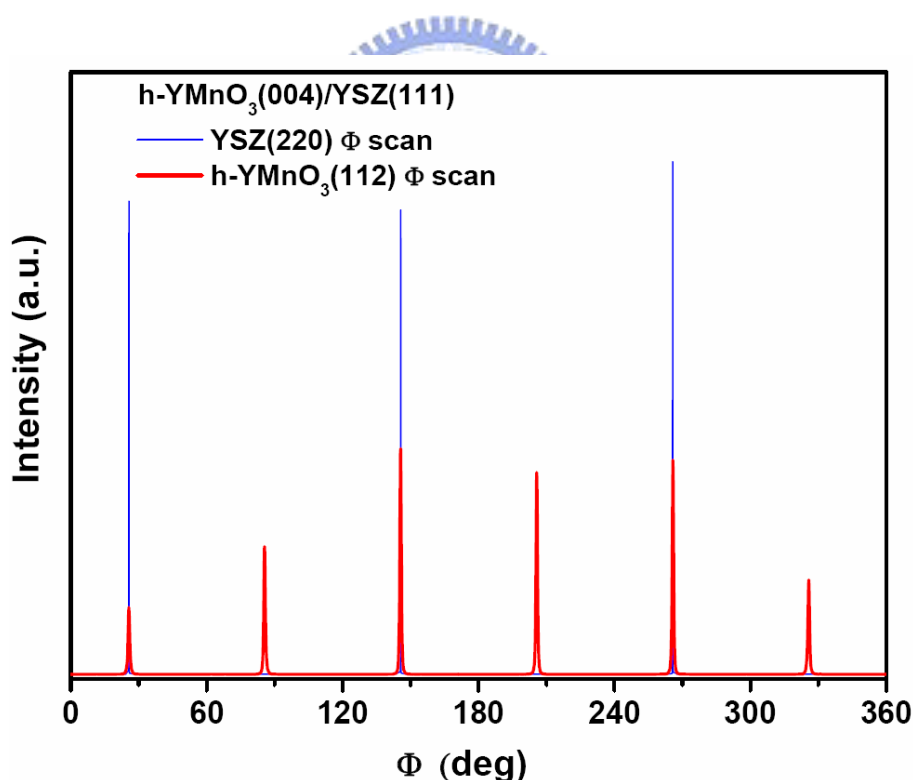


Fig. 4.4 The XRD Φ -scan patterns show both off-normal YSZ(220) and h -YMO(112) peak with h -YMO(00 ℓ)/YSZ(111) thin films deposited at 880°C . The results clearly display the intimate epitaxial relationship between film and substrate, as well as the distinct film orientation characteristics.

Finally, we present the preliminary magnetic behavior of the h -YMO(00 ℓ)/YSZ(111) thin films by showing the temperature dependent susceptibility $\chi(T)$ in Fig. 4.5. The $\chi(T)$

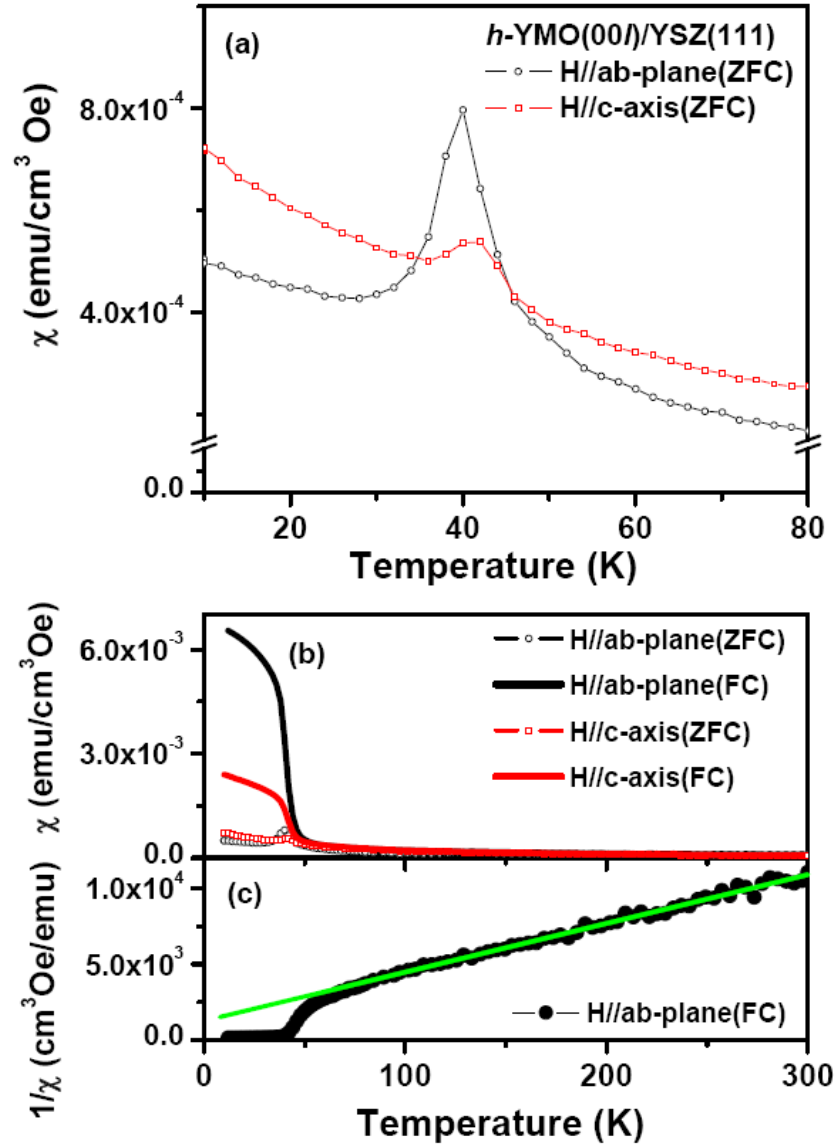


Fig. 4.5 Temperature dependent susceptibility showed the magnetic behavior of the h -YMO(00 ℓ)/YSZ(111) films. All the data was collected with an applied field 500 Oe. (a) Temperature dependent susceptibility curve with applied field parallel to c -axis and a - b plane of the films. It displayed the field-cooled (solid lines) and zero-field-cooled (line with symbols) susceptibility showed for 10~80K. (b) Similar to (a), temperature dependent susceptibility along c -axis and perpendicular c -axis of the films measured over the entire temperature range. (c) The figure showed the reciprocal susceptibility versus temperature which was measured with an applied field parallel to a - b plane.

measurements were performed in a QuantumDesign® SQUID magnetometer by applying a small external field (500 Oe) either parallel or perpendicular to the c-axis. Both the zero field cool (ZFC) and field cool (FC) schemes were measured. As has been discussed in Chapter 3, there are two magnetic phase transitions (around 74K and 44K, respectively) in the ZFC and FC $\chi(T)$'s that might be regarded as the intrinsic Néel temperature and a superspin-glass-like (SSG) transition associated with disorder-coupled spin reorientation behavior. However, as shown in Fig. 4.5(a) and 4.5(b), the $\chi(T)$ data plotted either in the temperature range of 10 ~ 80 K or in a wider range of 10 – 300 K, only the transition around 40 K is seen and the AFM ordering around 74 K appears to be completely suppressed. In Fig. 4.5(c), we plot the reciprocal susceptibility as a function of temperature. It is evident that the curve starts to deviate from the linear Curie-Weiss

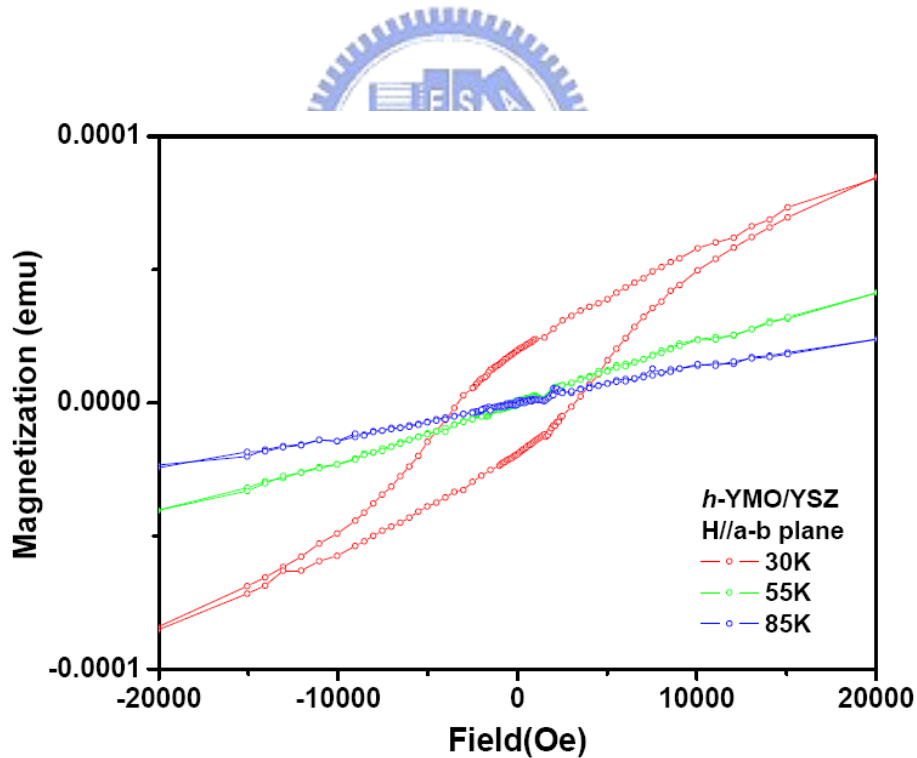
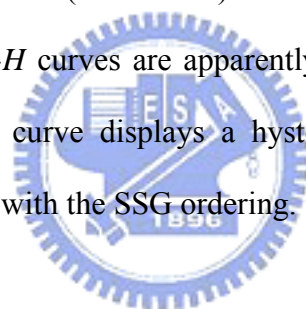


Fig. 4.6 The field dependent magnetization behavior of the h -YMO(00 ℓ)/YSZ(111) thin films measured at several temperatures. The external field was parallel to the a-b plane in the range of -2T~2T. Notice the hysteresis loop appears at 35 K indicating the existence of SSG characteristic.

behavior near 70K, indicating that there indeed an intrinsic AFM transition around 70 K. The $\chi(T)$ results also display that there exists significant magnetic anisotropy when measuring along different crystalline axes (c-axis and a - b plane). The difference between the FC and ZFC susceptibility near the transition appears to be larger when the field is applied in the a - b plane than along the c-axis. Since the AFM ordering of h -YMO is believed to originate primarily from the in-plane Mn-O-Mn superexchange with a weaker inter-planar Mn-O-O-Mn exchange interaction in the stacking triangular lattice [6], the larger difference between the ZFC and FC measurements in a-b plane may reflect a stronger effect on the superexchange interaction when the disorder-induced SSG mechanism sets in. To further delineate the scenario of SSG, we measured the field dependent magnetization behavior (M - H curve) with the applied field in the a - b plane in the range of $-7T \sim 7T$. The M - H curves are apparently linear at 300 K, 85 K and 55 K. However, at 35 K the M - H curve displays a hysteresis loop in consistent with the signature expected in systems with the SSG ordering.



4.4 Summary

The hexagonal $YMnO_3(00\ell)$ thin film was prepared on YSZ and Al_2O_3 substrates by the pulsed deposition process. The XRD results showed that the films are having epitaxial and highly oriented characteristics on YSZ(111) substrate as compared to that obtained on the $Al_2O_3(00\ell)$ substrates. The films were better crystallized at higher substrate temperatures in addition to being affected by the mismatch between thin film and substrate. The films all showed six-fold symmetry expected from a well in plane alignment hexagonal compound, as revealed by the XRD Φ -scan patterns. For the h -YMO(00ℓ)/YSZ(111) thin film, an AFM transition around 70K (T_N) is observed with

the magnetic superspin glass reordering at temperature $\sim 40\text{K}$. The susceptibility anisotropy suggests the system may have a larger superexchange interaction for the in-plane (a - b plane) triangular Mn^{3+} spin orders and a weaker inter-planar interaction for Mn^{3+} magnetic moments.

References

- [1] W.J. Chang, C.C. Hsieh, J.Y. Juang, K.H. Wu, T.M. Uen, Y.S. Gou, C.H. Hsu, J.Y. Lin, *Journal of Applied Physics*. 96 (2004) 4357.
- [2] S.F. Chen, W.J. Chang, S.J. Liu, J.Y. Juang, J.Y. Lin, K.H. Wu, T.M. Uen, Y.S. Gou, *Physica B-Condensed Matter*. 336 (2003) 267-274.
- [3] B.B. van Aken, A. Meetsma, T.T.M. Palstra, *Acta Crystallographica C*. 57 (2001) 230-232.
- [4] M.N. Iliev, M.V. Abrashev, H.G. Lee, V.N. Popov, Y.Y. Sun, C. Thomsen, R.L. Meng, C.W. Chu, *Physical Review B*. 57 (1998) 2872-2877.
- [5] K.H. Wu, J.Y. Juang, C.L. Lee, T.C. Lai, T.M. Uen, Y.S. Gou, S.L. Tu, S.J. Yang, S.E. Hsu, *Physica C*. 195 (1992) 241.
- [6] M. Fiebig, V.V. Pavlov, R.V. Pisarev, *Journal of the Optical Society of America B-Optical Physics*. 22 (2005) 96-118.

Chapter 5

Anisotropic magnetic behavior in substrate-stabilized orthorhombic YMnO_3 thin films

In previous chapter, we demonstrated the hexagonal YMnO_3 films grown on the YSZ(111) substrate and the associated magnetic behaviors. The in-plane mismatch may result in tremendous strain in the resultant thin films. Although, there are evidences both theoretically and experimentally indicating the possibility of obtaining marked magnetism-induced polarization in perovskite manganites with smaller rare earth ions, such as the Group II ReMnO_3 , with $R_{\text{Re}} < R_{\text{Y}}$ and R_{Ho} . However, since the perovskite structured orthorhombic phase is not the thermodynamically stable phase for the Group II ReMnO_3 compounds, discrepancies between the theoretic predictions and experiments are not fully clarified. Here, we report in this chapter how to utilize the epitaxial strain between film and substrate to obtain the perovskite YMnO_3 films with specifically oriented crystalline structures. In this case, the MnO_5 bipyramid, which is the most relevant basic unit for magnetism and polarization, is expected to transform into the MnO_6 octahedron. Thus, by stabilizing the orthorhombic structure with the in-plane strain force between perovskite substrates and RMnO_3 compounds, significant modifications on the electromagnetic properties of the system are anticipated.

5.1 Introduction

As discussed in chapter I, although quite a few materials have been identified to have multiferroic characteristics, perhaps, the most intriguing class is the family of the perovskite

manganites, $RMnO_3$ (R: rare earth and Y). For instance, series of orthorhombic phases with the $Pbnm$ space group have been prepared and studied [1-3]. By considering detailed structure the most relevant ingredient, the MnO_6 octahedron, as a function of ionic size of the rare earth elements, Goto et al. [2] demonstrated that, with the decreasing ionic size, the lattice constant is varied by Jahn-Teller distortion and the Mn-O-Mn bond angle decreases from 155° ($LaMnO_3$) to 140° ($LuMnO_3$) [3]. This, in turn, gives rise to an evolution in magnetic structure by changing the antiferromagnetic (AFM) order from A -type (Mn moments ferromagnetically coupled within a - b plane and the inter-planar coupling is AFM) to E -type. The path by which the magnetic structure varies with temperature turns out to play the key role of exhibiting the magnetism-induced “improper ferroelectricity”. In the A -type AFM regime, it has been demonstrated that the paramagnetic Mn moments first convert into an incommensurate (ICM) AFM structure below the Néel temperature (T_N) and then enter a reordered commensurate (CM) helical spin structure below a lock-in transition temperature (T_L) for $R = Eu, Gd, Tb, \text{ and } Dy$ [2]. The transition to the helical magnetic structure evidently breaks the spatial inversion symmetry thus allowing the ferroelectric polarization to accompany. This microscopic understanding explains not only the colossal magneto-capacitance concurring with the ICM to CM transition in $DyMnO_3$ [2] but also the intimate magneto-electric coupling in $TbMn_2O_5$ [5]. Subsequent theoretical studies by Katsura et al. [6, 7] pointed out that the electric polarization is primarily induced by the microscopic noncollinear magnetic structure via spin-orbital interaction. Mostovoy reached the similar conclusions using the Ginzburg-Landau phenomenological approach [8]. On the other hand, Sergienko et al. [9] argued that, for E -type o - $RMnO_3$ in addition to the electronic origin, the mechanism of magnetic ferroelectricity can also be originated from magneto-elastic interaction. By fixing the location Mn, they estimated the displacement of oxygen ions in MnO_6

octahedron due to competitions among the double exchange, superexchange, and Dzyaloshinskii-Moryia interactions. This so-called improper magnetic ferroelectrics (IMF), in fact, has suggested a surprisingly large (about two orders of magnitude) induced polarization [10].

It is clear that timely experimental confirmations are in order to clarify some of the discrepancies existing between various theories. Unfortunately, under ambient conditions, the crystal structure of $RMnO_3$ transforms from orthorhombic to hexagonal as the ionic size of the rare earth elements gradually decreases from Nd to Ho. Consequently, although the helical spin induced polarization has been evidenced to encompass the theoretical predictions as pointed out above, there are still significant discrepancies concerning the induced polarization between the experimental observations and theoretical predictions in the collinear *E*-type AFM systems [11-14]. For instance, Sergienko et al. [9] estimated a polarization of $\sim 6 \mu\text{C}/\text{cm}^2$ for *o*- HoMnO_3 (*o*-HMO) with *E*-type AFM ordering (which is compatible with traditional ferroelectric $RMnO_3$) [15], while only $9 \text{ nC}/\text{cm}^2$ was observed experimentally in high pressure-derived polycrystalline *o*-HMO [11]. With the *E*-type scenario, the zigzag chain was observed in *a*-*b* plane showed in Fig. 5.1 [11]. In the neutron scattering powder diffraction data, HoMnO_3 was regarded as an *E*-type magnetic structure and YMnO_3 was set to have a temperature independent sinusoidal magnetic structure in lock-in phase [16, 17]. The sinusoidal magnetic structure in YMnO_3 should induce antiferroelectric behavior shown in Fig. 5.1(b), and it is quite different from the *E*-type magnetic structure in HoMnO_3 . The sinusoidal magnetic structure was also predicted as zero induced polarization by Mostovoy [8]. It is interesting that the value of the induced polarization in YMnO_3 was triple bigger than HoMnO_3 in polycrystalline powders. However, there must be something wrong or incomplete data or theory. The discrepancies were ascribed to

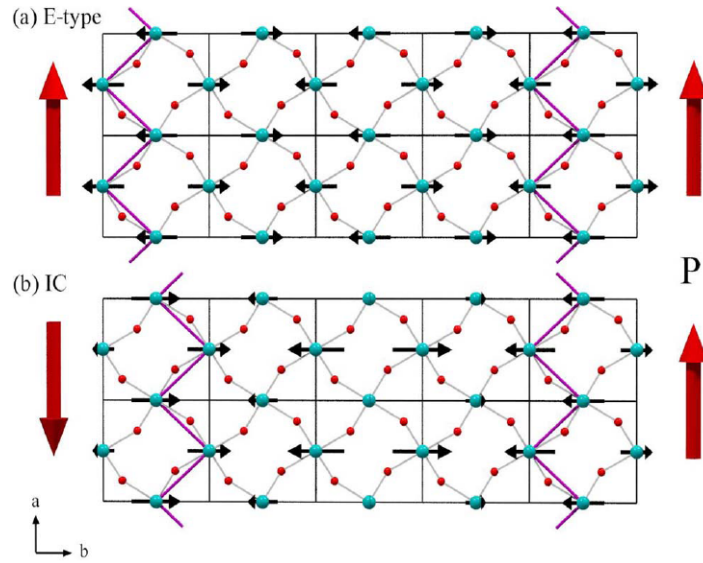


Fig. 5.1 Magnetic order and ferroelectric polarization arising from the double exchange mechanism for (a) the *E*-type commensurate structure (HoMnO_3) and (b) the sinusoidal incommensurate order proposed for YMnO_3 . (Ref. 19) Large spheres: Mn ions with spins. Small spheres: oxygen ions. The FM aligned zigzag chains are shown for the first and last unit cells and the local polarization in these chains is indicated by the large vertical arrows.

the unavailability of single crystalline samples and additional ways of preparing orientation-specific orthorhombic RMnO_3 films have received extensive attention recently [18-20]. Among them, Y^{3+} (1.06\AA) has the critical ionic size right at the boundary of structure variations. As a result, it is expected that YMnO_3 can form either the orthorhombic (*o*-YMO) or the hexagonal (*h*-YMO) phases with just a slight variation of preparation conditions. For the *h*-YMO, the ferroelectric polarization along the *c*-axis originates from the structure distortion such as tilted MnO_5 and displacement of Y^{3+} ions, which behaves similarly as the traditional ferroelectric materials, such as BaTiO_3 , and is referred as the “proper ferroelectrics”. One of the common characteristics of these class of materials is they all have much higher ferroelectric temperature (T_{FE}) than the magnetic ordering temperature. For instance, the T_{FE} of *h*-YMO is

about 920 K [21], whereas the antiferromagnetic (AFM) temperature T_N is ~ 80 K [22]. The drastic difference between T_{FE} and T_N naturally has cast serious doubt about the possibility of any coupling existing between the two orders.

On the other hand, as described above, the ionic size of Y is also situating at the point where the magnetic structures of orthorhombic $RMnO_3$ series transforms from the A-type AFM to E-type AFM and has been found to exhibit an ICM-ICM spin reorientation at a temperature below T_N [16]. It is, thus, interesting to unveil how the orthorhombic $YMnO_3$ (*o*-YMO) will behave in inducing ferroelectric ordering. In this chapter, we report an effective way of preparing *o*-YMO films with specific crystal orientations. These films allow us to further delineate any possible magnetic ordering anisotropy along the principal crystal axes by measuring the temperature dependent magnetization with field applied along the correspondent orientations. (For the sake of consistency, we will adopt the $Pbnm$ symmetry setting for discussing orthorhombic manganites mentioned in the remaining paragraphs.) Our results show that, in addition to the usual AFM transition, there exists a lower temperature magnetic ordering which exhibits significant anisotropic characteristics. The present results suggest that the magnetic ferroelectricity may be closely related to the anisotropic nature of magnetism in these materials.

5.2 Experiment

The obtained hexagonal $YMnO_3$ bulk presented in chapter 3 was used as the target for depositing YMO films respectively on $SrTiO_3$ (STO)(001), STO(110), and $LaAlO_3$ (LAO)(110) substrates by pulse laser deposition (PLD) technique [23]. As will be shown below, films with distinct crystallographic orientations were obtained when proper deposition conditions were

practiced. In order to optimizing the deposition conditions, the KrF excimer laser was operated at the repetition rate of 1~10 Hz with energy density of 2-5 Jcm⁻² and the substrate temperature (T_s) was varied between 700 °C and 880 °C with the oxygen partial pressure being controlled between background pressure (10⁻⁶ torr) to 0.3 torr during deposition. The film thickness is between 180-250 nm. The structural characteristics of the films were measured by x-ray diffraction (XRD) θ -2 θ and Φ scans. The temperature dependent magnetic susceptibility ($\chi(T)$) along various principal crystalline axes was measured in a Quantum Design® superconducting quantum interference device (SQUID) with a small applied magnetic field to delineate the possible magnetism anisotropy in this material.

5.3 Results and discussions

Fig. 5.2 shows the XRD θ -2 θ patterns of the YMO films deposited respectively on (a) STO(001), (b) STO(110), and (c) LAO(110) single crystalline substrates at various temperatures. As clearly displayed in Fig. 5.2(a) and 5.2(c), for films deposited on STO(001) and LAO(110) substrates, pure *o*-YMO(00 ℓ) and *o*-YMO(020) are respectively obtained over the whole T_s range (700-880 °C) practiced. It is also indicative that the crystalline quality is progressively improved with increasing T_s . On the other hand, for those deposited on STO(110) substrates (Fig. 5.2(b)), the film orientation appears to evolve from mainly *o*-YMO(020) at $T_s = 700$ °C to nearly pure *o*-YMO(200) at $T_s = 880$ °C. It is evident that, although orthorhombic YMO can be grown on STO(110) substrate, the growth window of obtaining purely a-axis-oriented *o*-YMO(200) thin films is much more critical than that for *o*-YMO(00 ℓ) and *o*-YMO(020) films grown on STO(001) and LAO(110) substrates. The reason for these differences presumably is resulted from the detailed lattice matching effects to be discussed below.

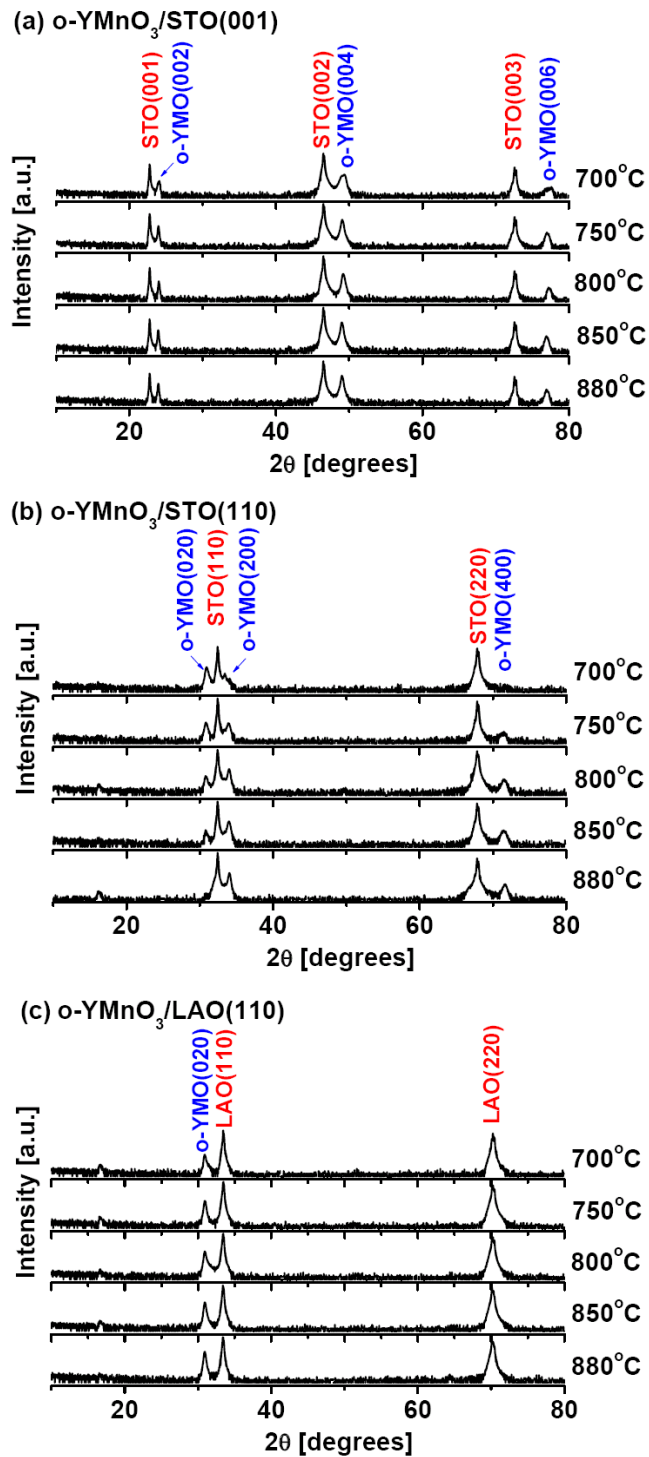


Fig. 5.2. The XRD θ - 2θ patterns of o-YMO thin films grown on (a) STO(001), (b) STO(110), and (c) LAO(110) substrates as a function of the deposition temperature. All films were controlled to have the same thickness (180 nm) and an optimum oxygen partial pressure of 0.1 torr to delineate the relation between temperature and the degree of crystallization in the deposition process.

By comparing the lattice constants among LAO (cubic: $a = b = c = 3.782 \text{ \AA}$), STO (cubic: $a = b = c = 3.905 \text{ \AA}$), and *o*-YMO (as summarized in Table 5.1), one finds that the lattice mismatches between the in-plane diagonal of STO ($\sqrt{2}a_{STO} = 5.522 \text{ \AA}$) and the *a*- and *b*-axis of *o*-YMO are -4.97% (compressive) and 5.50% (tensile), respectively. Since the resultant strain would be quite similar for either *a*-axis or *b*-axis to align with the [110] or $[1\bar{1}0]$ direction of STO (as schematically depicted in the left panel of Fig. 5.3(a)), one expects that a twin-like

Table 5.1. The fitting parameters and in-plane mismatch calculations between *o*-YMO thin films and substrates used in this study. The strain factor is defined as $(d_{\text{fitting}} - d_{\text{database}})/d_{\text{database}}$, and the “-” sign means contraction and otherwise means expansion of the respective axis of *o*-YMO.

Sample	parameter	a (Å)	b (Å)	c (Å)	V(Å ³)	a-c diagonal	b-c diagonal
Database ^[a]		5.2616	5.8444	7.3579	226.26	9.0456	9.3966
<i>o</i> -YMO(00ℓ) on STO(001)		5.245	5.768	7.435	224.93		
STO(001) substrates (in plane length)		5.522 $\sqrt{2}a$	5.522 $\sqrt{2}a$	In plane	in plane		
in-plane mismatch with substrate		4.97%	-5.50%				
Strain factor		-0.316%	-1.31%	1.05%	-0.589%		
<i>o</i> -YMO(200) on STO(110)		5.267	5.686	7.491	224.32	9.157	9.404
STO(110) substrates (in plane length)			5.522 $\sqrt{2}a$	7.810 2a		9.565 $\sqrt{6}a$ ^[b]	9.565 $\sqrt{6}a$ ^[b]
in-plane mismatch with substrate			-5.51%	6.14%		5.74%	1.80%
Strain factor		0.0945%	-2.71%	1.81%	-0.859%		
<i>o</i> -YMO(020) on LAO(110)		5.276	5.773	7.415	225.81	9.100	9.397
LAO(110) substrates (in plane length)		5.348 $\sqrt{2}a$		7.564 2a		9.264 $\sqrt{6}a$ ^[b]	9.264 $\sqrt{6}a$ ^[b]
in-plane mismatch with substrate		1.68%		2.83%		2.44%	-1.38%
Strain factor		0.264%	-1.22%	0.773%	-0.196%		

^[a] The lattice constant of *o*-YMnO₃.^[4]

^[b] Film substrate direction aligning see text for detail description.

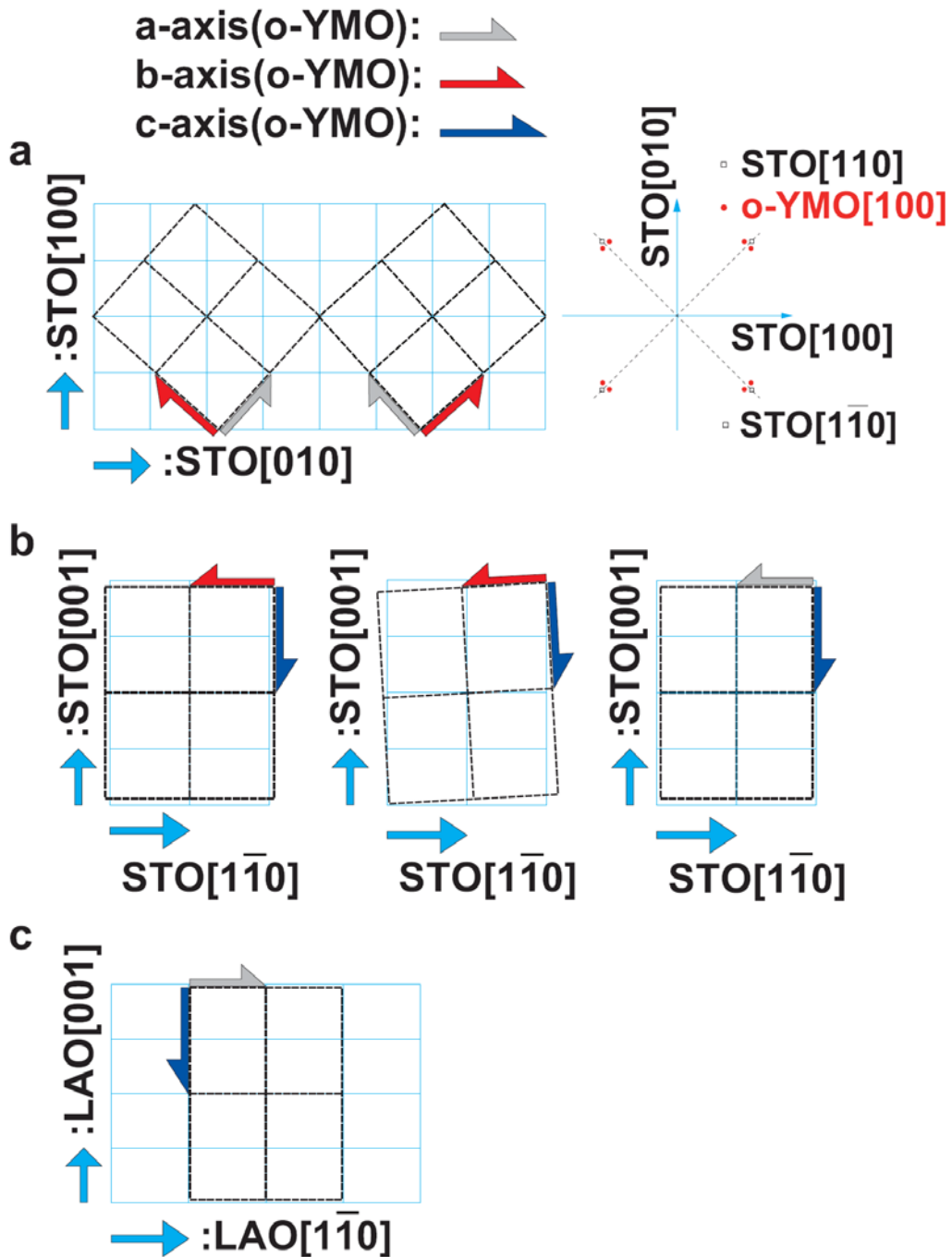


Fig. 5.3 The schematics of the in-plane arrangements between the o-YMO thin films and substrates. (a) *o*-YMO(00 l)/STO(001): *a*-axis or *b*-axis of *o*-YMO is aligned randomly with STO[110] substrate direction; (b) in-plane schemes of *o*-YMO thin films on STO(110) showing that the *c*-axis of *o*-YMO is aligned with STO[001], but the *a*-axis or *b*-axis can be randomly aligned with STO[1 $\bar{1}$ 0]; and (c) *o*-YMO(020)/LAO(110): *c*-axis and *b*-axis of *o*-YMO are aligned with LAO[001] and LAO[1 $\bar{1}$ 0] respectively.

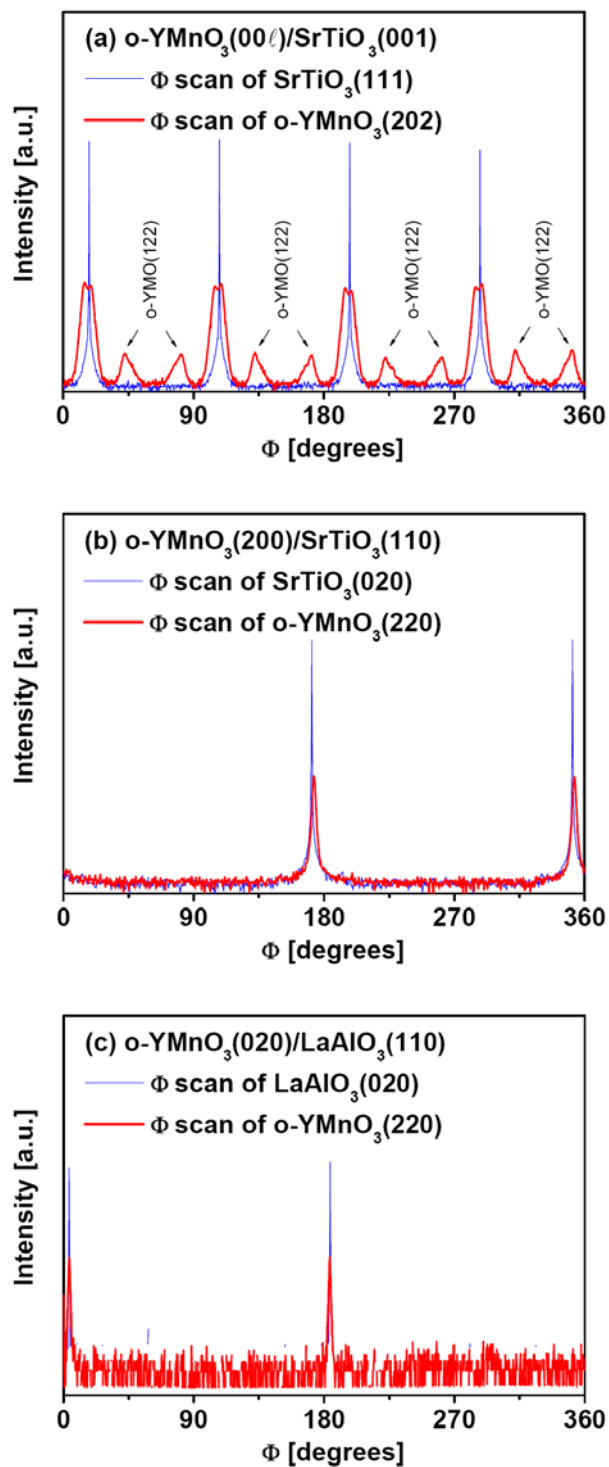


Fig. 5.4 The XRD Φ -scan patterns of $o\text{-YMO}$ thin films deposited at 880 °C on different substrates. (a) $o\text{-YMO}(00\ell)/\text{STO}(001)$; (b) $\text{STO}(110)$; and (c) $\text{LAO}(110)$. The results clearly display the intimate epitaxial relationship between film and substrate, as well as the distinct film orientation characteristics.

structure with a separation angle of about 5° (see the right panel of Fig. 5.3(a)) might occur in these *o*-YMO(00ℓ) films. Indeed, as revealed in the XRD Φ -scans shown in Fig. 5.4(a), a primary four-fold symmetry is observed. In addition to the well-alignment between the film and substrate, it is also noted that the Φ -scans of the (202) peak of the *o*-YMO films exhibits a split feature separating by about 3.9° , in good agreement with our estimation. Another feature to be noted is that the splitting of the (202) peak of *o*-YMO, though appears to be asymmetric presumably due to the slight misalignment, is in fact displaying a two-fold symmetry for each set of the twinned grains, in support of our abovementioned conjecture. We note that the weaker eight peaks appearing in the Φ -scans (Fig. 5.4(a)) are reflections from (122) planes of *o*-YMO. They are picked up in the Φ -scans presumably due to the proximate d-spacing of the two families of reflecting planes.

For the case of the *o*-YMO thin films grown on LAO(110) substrates the alignments are much simpler. By comparing the parameters listed in Table 5.1, one obtains that, with the *a*-axis and *c*-axis of *o*-YMO aligning with the $[1\bar{1}0]$ and $[001]$ directions of LAO(110) substrate (as depicted schematically in Fig. 5.3(c)), the expected in-plane mismatches between film and substrates are only about 1.7% and 2.8%, respectively. Consequently, one expects that not only the substrate will favor the growth of (0*k*0)-oriented *o*-YMO films but also will result in a nearly perfect epitaxial relationship. In addition to the evidence of *b*-axis oriented features from Fig. 5.2(c), the Φ -scans of the *o*-YMO(220) and the LAO(020) diffraction peaks (Fig. 5.4(c)) indeed clearly indicate the two-fold symmetry for pure orthorhombic structure and the excellent epitaxial relations between film and substrate. Finally, we turn to the case of the *a*-axis *o*-YMO films grown on the STO(110) substrates. As displayed in Fig. 5.2(b), the growth orientation of the films depends very much on the substrate temperature. As depicted schematically in Fig.

5.3(b), there are three most likely matching schemes that would accommodate the lattice of *o*-YMO on the STO(110) substrate. Since at the lower substrate temperatures the films appear to be of mixed orientations (Fig. 5.2(b)), we will discuss only the $T_s = 880$ °C case. From the Φ -scan results shown in Fig. 5.4(b), it is clear that the film is mainly *a*-axis oriented, albeit there is a slight misalignment between the *o*-YMO(220) and STO(020) reflections. In this case, since the film is *a*-axis-oriented, the plausible lattice matching schemes would be the two depicted in the left and the middle panels of Fig. 5.3(b). From Table 5.1, the direct match of the *b*- and *c*-axes of *o*-YMO along the $[1\bar{1}0]$ and $[001]$ directions of STO(110) substrate will result in mismatches of -5.52 % and 7.81 %, respectively. However, if instead we allow the lattice to slightly rotate around *a*-axis and matches the *bc*-diagonal with the $[\bar{2}\bar{2}1]$ direction of the substrate, the resultant mismatch could be reduced to only 1.80 %. This also explains the slight misalignment between the Φ -scans of *o*-YMO(220) and STO(020) reflections.

Since the evolution of the magnetic structure is believed to intimately relate with magnetoelectric coupling and the associated IMF [11], it is essential to delineate how the magnetic ordering behaves in more details. Fig. 5.5 shows the temperature dependence of dc magnetic susceptibility ($\chi(T)$) measured with an external field $\mathbf{H} = 500$ Oe applying along the three major crystallographic axes. It is evident that, regardless of the direction of the applied field and the film growth orientation, all films exhibit an AFM transition with the Neél temperature $T_N \sim 44$ K (see also the field-cooled (FC) and zero-field-cooled (ZFC) $\chi(T)$'s displaying in the inset of each panel in Fig. 5.5), which is consistent with previous results. However, a second reordering of magnetic structure, which appears to be very much dependent on film and crystal orientations, is observed. For instance, in *o*-YMO(001)/STO(001) film (Fig. 5.5(a)), the reordering temperature is $T_{SR} \sim 28$ K for $\mathbf{H} // ab$ -plane and at $T_{SR} \sim 18$ K for $\mathbf{H} //$

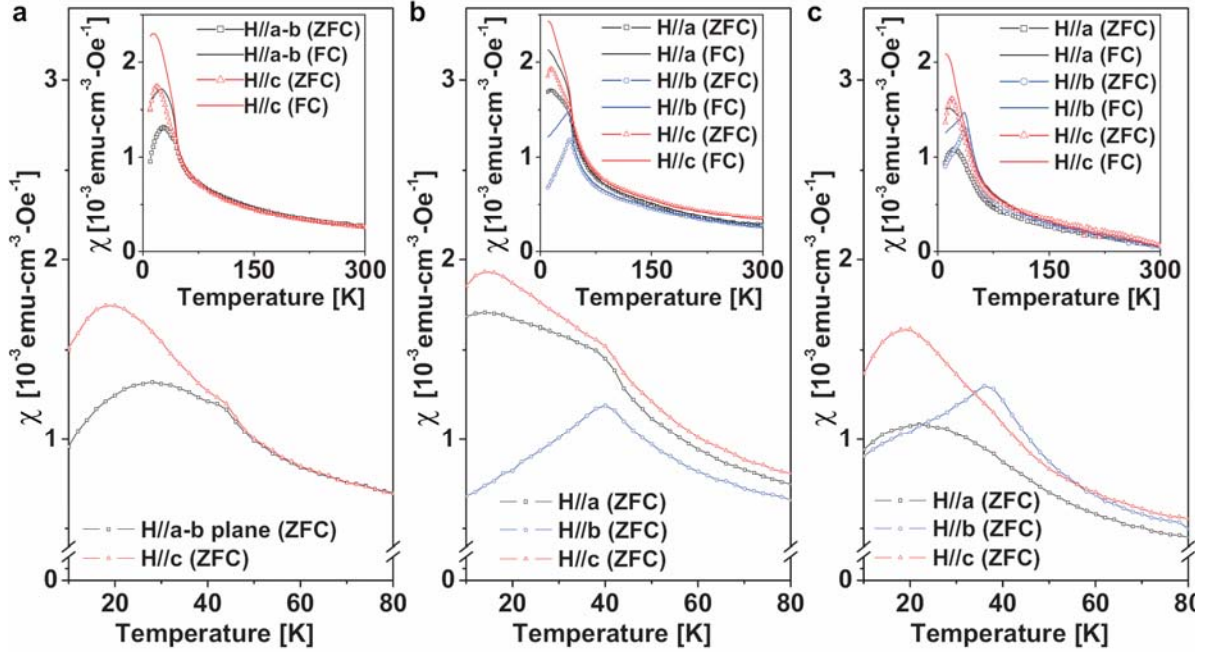


Figure 5.5: Temperature dependent magnetization along respective crystallographic orientations of (a) o -YMO(00 l)/STO(001); (b) o -YMO(020)/LAO(110); and (c) o -YMO/STO(110). The insets in each panel display the field-cooled (solid lines) and zero-field-cooled (symbols) magnetization measured over the entire temperature range in an applied field 500 Oe.

c -axis, respectively. For o -YMO(020)/LAO(110) (Fig. 5.5(b)) and o -YMO(200)/STO(110) (Fig. 5.5(c)) films, while both T_N (~ 40 K) and T_{SR} (~ 16 -18 K) are observed for $\mathbf{H} // a$ -axis and $\mathbf{H} // c$ -axis, the second reordering is completely absent for $\mathbf{H} // b$ -axis. It clearly demonstrates that, whatever its nature might be, the second reordering is orientation dependent.

The possible origin of the second spin reordering at temperature below T_N for o -YMO has been discussed previously. Quezel et al. [24] pointed out in their early neutron scattering experiment that, at the Neél temperature ($T_N \sim 42$ K) of o -YMO, the Mn moments form an antiparallel spin order in the a - c plane and can be characterized as a spin density wave with a helical angle ($\phi = 14^\circ$) propagating along b -axis. The propagation vector $k = [0, k_y, 0]$

subsequently experiences a magnetic reordering transition at some lower temperature (~ 26 K) and locks into a magnetic incommensurate structure with a relative small $k_y = 0.0786$, which becomes temperature independent afterwards. More recently, Muñoz et al. [16] argued that for *o*-YMO the magnetic structure below T_N (44.4 K) is a sinusoidal spin density wave propagating along *b*-axis with a relative large $k_y = 0.42$. With decreasing temperature, k_y increases to 0.43 and remains constant below the incommensurate lock-in temperature (28K). In their study of high-pressure synthesized polycrystalline *o*-YMO powders, Lorenz et al. [12] identified a second magnetic transition at $T_L \sim 28$ K and attributed it to the ICM-ICM transition revealed by the earlier neutron scattering data [16]. However, in their more recent ferroelectricity results on the same materials, Lorentz et al. [11] found it is difficult to reconcile their polarization results of *o*-YMO with the proposed magnetic structure evolution and suggested that reconsideration of magnetic structure seems to be necessary. On the other hand, Kim et al. [13] reported a ferroelectric temperature at $T_{FE} \sim 31$ K in their specific heat and dielectric measurements performed on *o*-YMO samples. Although whether or not the T_{FE} correlates with T_L or any magnetic structure change directly remains to be clarified, it does suggest a second reordering in the system occurring below the Néel's temperature. Finally, Martí et al. [14] found in their *c*-axis oriented epitaxial *o*-YMO films, in addition to an apparent splitting between the FC and ZFC $\chi(T)$'s which signifying T_N around 45 K, there is also a broad maximum in the ZFC- $\chi(T)$ near 25 K. However, instead of attributing it to the ICM lock-in transition revealed in the neutron experiments [16, 24], they suggested it might be more relevant to the strain induced by the Nb-doped STO substrate. It appears that questions such as: "Is the second reordering revealed in the magnetization measurements the manifestation of the ICM-ICM lock-in transition? And how would it affect the subsequent magnetism-induced IMF expected in

orthorhombic rare-earth manganites?” remain unsettled.

We try to address the abovementioned questions by examining the magnetic structure anisotropies displayed in Fig. 5.5 in more details. Firstly, we note that, when the crystalline orientations are distinctively discernible, only the AFM transition is seen and the low temperature magnetic reordering is not detectable when $\mathbf{H} // b$ -axis (Figs. 5.5(b) and 5.5(c)). Within the context of both helical and sinusoidal incommensurate AFM ordering scenarios, the lock-in transition involves only a change in the propagation vector of some kind of spin density wave. Since the dc magnetization is a measure of the collective contribution from Mn^{3+} spin moments which when form a strong AFM order along the b -axis of o -YMO might remain so even subject to the propagation vector change observed in neutron scattering. This is consistent with the $\mathbf{H} // b$ -axis results displayed in Figs. 5.5(b) and 5.5(c) and also implies that the second reordering may not be associated with the ICM-ICM lock-in transition directly. In fact, Muñoz et al. [16] also reported the neutron diffraction peaks other than b -axis ordering developing substantially at temperature around 20 K, indicating magnetic structures other than the b -axis AFM order might actually happen in o -YMO.

Then the question to follow immediately will be what gives rise to the second reordering manifesting in the $\chi(T)$'s obtained when the field is applied along the a - and c -axis? We note that, except for the case in-plane $\chi(T)$ in Fig. 5.5(a) where the broad peak appears around 28 K similar to most of reported results for polycrystalline o -YMO, the second reordering probed along the a - and c -axis seems to be generic and may be reflecting some intrinsic magnetic ordering. Namely, in all three sets of o -YMO films T_{SR} all occurs around 16-18 K with the c -axis magnetization being larger than that of the a -axis, albeit some subtle differences between the o -YMO films grown on different substrates might still exist due to epitaxial strain. For example,

T_N and T_{SR} measured along the c -axis are about 44 K and 18 K for o -YMO(00 ℓ) film grown on STO(001) substrate while that for o -YMO(020) film grown on LAO(110) substrate are 40 K and 16 K, respectively. The Ω -scans (rocking curves, not shown here) of the primary diffraction peaks of the o -YMO(00 ℓ)/STO(001) and o -YMO(020)/LAO(110) films give a full width at half maximum (FWHM) of 0.056° for the former and 0.6° for the latter. These preliminary comparisons do indicate that the magnetic ordering temperatures are susceptible to the structure disorders. In order to further elaborate this conjecture is indeed consistently reconciling all the films investigated in this study, we compare the “strain factor” (defined as $\varepsilon \equiv (d_{\text{film}} - d_{\text{bulk}}) / d_{\text{bulk}}$) of each films. Here d_{film} and d_{bulk} are lattice constants of respective crystallographic axis obtained from present films with the aids of four-circle XRD analyses as well as those cited from the polycrystalline bulk powders, respectively. The results give (*see* Table 5.1) $\varepsilon_a \approx 0.26\%$, $\varepsilon_b \approx -1.22\%$, and $\varepsilon_c \approx 0.77\%$ for the (020)- o -YMO film on LAO(110). On the other hand, $\varepsilon_a \approx -0.32\%$, $\varepsilon_b \approx -1.31\%$, and $\varepsilon_c \approx 1.05\%$ for (00 ℓ)- o -YMO film on STO(001), albeit the lattice mismatch suggests that, in this film, the a -axis of the film should be in compression while the b -axis is in tension. Finally, for the o -YMO(200)/STO(110) film, $\varepsilon_a \approx 0.095\%$, $\varepsilon_b \approx -2.71\%$, and $\varepsilon_c \approx 1.81\%$. From the above comparisons, it is suggestive that for o -YMO, whether it is under compression or tension from the substrate strain, the a -axis appears to be the most robust axis while the b -axis is most susceptible to the external strain and is easily deformed. We believe that, during the process of stabilizing the orthorhombic structure, the substrate not only helps to change the MnO_5 bi-pyramid into MnO_6 octahedron but also accommodate the films with specific growth orientations. This, in turn, should have some influences on the detailed magnetic properties unveiled here. Indeed, the noticeable compressive strain along the b -axis in all films may have buckled the Mn-O bonding and changed the planar (ac -plane) AFM structure

conceived in both helical [24] and sinusoidal [16] scenarios into some canted-AFM state. This also explains why the magnetic second reordering seems to be intrinsic to all films as described above. As for the subtle differences mentioned above such as the broadening of transition and down-shift of T_N found in the (200)-*o*-YMO films, it is also consistent with the significantly larger lattice distortions, and hence greater crystalline disorder, exhibited in these particular films. In addition, as has been discussed in Fig. 5.2(b), the *a*-axis oriented films are in fact containing some trace amount of *b*-axis oriented grains even at the optimal deposition conditions practiced in this study. Finally, we turn to the case shown in Fig. 5.5(a). In this case, the broad peak occurring around 28 K, as most of the results obtained from polycrystalline *o*-YMO, could be due primarily to the nature of in-plane *ab*-mixing specific in these (00 ℓ)-films.

Although the establishment of the “canting” scenario has to wait for direct supportive evidence from other independent measurements, it is, nevertheless, physically plausible. By comparing with the phase diagram for the family $RMnO_3$, [3] it can be concluded that the change of phase transition temperature is mainly caused by the Jahn-Teller distortion originated from the variation of the size of rare-earth ions. The Mn-O-Mn bond angle in the *ab*-plane and along the *c*-axis was found to decrease with decreasing the rare-earth ionic size. Simultaneously, the lattice constants of $RMnO_3$ are also changed by the Jahn-Teller distortion. For instance it was found that not only the lattice parameters of *a* and *c* decrease with the decreasing rare-earth ionic size of rare earth, but the AF magnetic structure also varies from A-type AFM for $R = Gd$, Tb to E-type AFM for $R = Ho$ through an intermediate spin spiral phase for $R = Y$. It is indicative that the chemical pressure induced by replacing La with smaller *R* is playing the essential role behind the rich magnetic structures exhibited in these multiferroic manganites via the manifestations of the Jahn-Teller effect and associated internal lattice strain. We believe that

the external strain effects originated from film/substrate epitaxial relations may also have similar effects on altering the magnetic properties of the materials. It would be interesting to see how these strain-induced magnetic ordering will affect the subsequent magnetic order-induced IMF, in addition to the ones expected from the ICM-ICM magnetic transitions. The current results, nevertheless, indicate that whatever such mechanism might turn out to be, it can be manipulated by choosing the proper substrates for thin film deposition.

On the other side, according to the further discussion in transforming hexagonal YMnO_3 to orthorhombic structure, we have realized the strain force played an ultra important role in stabilizing the perovskite structure. The strain force could support much higher force than 30kbar which was estimated from the experiments of M. N. Iliev et al, and the processing temperature could be reduced to much lower one ($1010^\circ\text{C} \rightarrow 700^\circ\text{C}$) [4]. HoMnO_3 was also a Goup II compound revealed hexagonal structure thermodynamically, and the ionic size of Y^{3+} and Ho^{3+} had similar value 1.06 and 1.05, respectively. In the RMnO_3 phase diagram, perovskite YMnO_3 and HoMnO_3 located at neighborhood and HoMnO_3 had been revealed incommensurate to commensurate E-type magnetic structure in the neutron scattering data [1, 17]. LAO(110) is one of the best substrates in stabilizing orthorhombic structure with the less lattice constant mismatch. With the similarity between YMO_3 and HoMnO_3 , we also deposited the $o\text{-HoMnO}_3(020)$ thin film on LAO(110) substrates [18]. It had highly oriented crystallized structure and the in-plane arrangement was consistent with to our conclusion in stabilizing $o\text{-YMO}$.

Fig. 5.6 showed the temperature dependent susceptibility of $o\text{-HoMnO}_3(020)/\text{LAO}(110)$ thin film, it had AFM ordering at Neel temperature 42.2K with the applied field parallel to all three crystalline axes which was similar to $o\text{-YMO}$. But the spin reordering phenomenon at

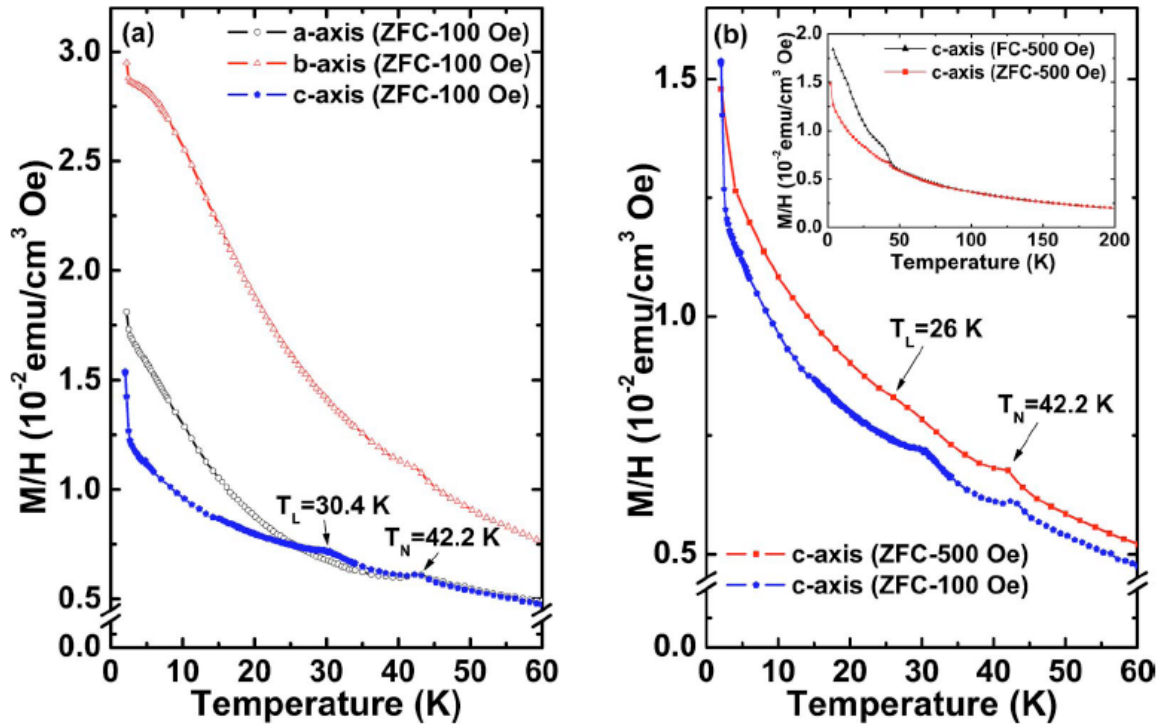


Figure 5.6: (a) The zero-field-cooled temperature dependent magnetizations [ZFC- $M(T)$] for o -HoMnO₃ film probed along the different crystal orientations with an applied magnetic field of 100 Oe. (b) The [ZFC- $M(T)$] along the c axis measured at 100 and 500 Oe. The inset in (b) shows full temperature range of the FC- and ZFC- $M(T)$ measured at 500 Oe. Notice the 30 K anomalous ordering along the c axis and the significant suppression of it by applying merely 500 Oe.

30.4K was only available along c-axis. This was quite different from the o -YMO/LAO(110) thin film. This may also described this thin was not a E-type one. In considering these two neutron diffraction data of o -YMO referred above, they derived different conclusions helical spin and temperature independent sinusoidal spin orders. Back to consider the phase diagram in Fig. 5.7, the ionic size of Y^{3+} was smaller than Dy^{3+} but larger than Ho^{3+} . We could not identify the real location in the phase diagram exactly for YMnO_3 because it is sitting right at the ambiguous rim between spin spiral and E-type phase. A little difference of the sample preparing processes may

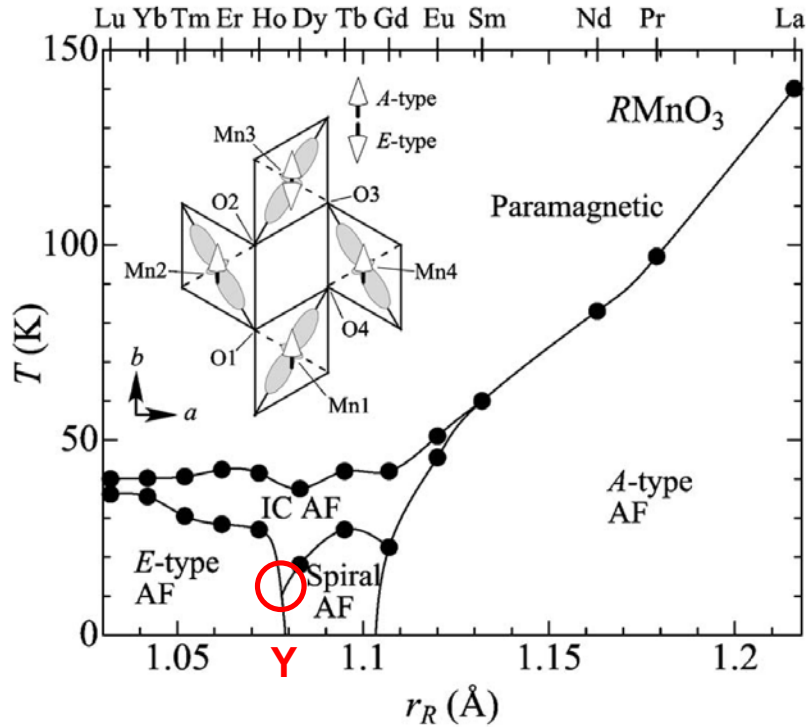


Figure 5.7: Magnetic phase diagram for $RMnO_3$ as a function of the ionic radius of R [3].

change the in-plane Mn-O-Mn bond angle and even involve the Jahn-Teller effect. Owing to this, the magnetic structure of o -YMO could be very sample dependent. In our thin films, LAO(110) substrates provide the necessary strain in stabilizing the orthorhombic structure. However, the strain may also support superfluous stabilizing force and substantially alter the intrinsic characteristics of o -YMO compounds. In Table 5.1, we see that the lattice constant is increased in a and decreased in b , suggesting that it has the tendency of pushing o -YMO forward to right side in Fig. 5.7 like $DyMnO_3$ and make it as a Group I compound. In this case, the scenario of the similar helical spin could also be applied to $YMnO_3$.

5.4 Summary

In summary, we have deposited the orthorhombic YMO films with distinct a -, b -, and c -axis orientating normal to the surface of STO(110), LAO(110), and STO(001) substrates, respectively. For the first two cases, nearly perfect in-plane alignments were also obtained. These films allow us to delineate the anisotropic nature of magnetic ordering in these intriguing multiferroic materials. For the o -YMO(020)/LAO(110) and o -YMO(200)/STO(110) films, an AFM transition around 40K (T_N) is observed regardless the orientation of the applied field. However, the magnetic reordering observed at $T_{SR} \sim 16$ -18 K is evident only when the field is applied in the a - and c -axes and is absent when probed along the b -axis. The magnetization behaves somewhat differently, however, in o -YMO(00 ℓ)/STO(001) films with the AFM occurring at $T_N \sim 44$ K and $T_{SR} \sim 28$ K (a - b plane) ~ 18 K (c -axis). The current results, though cannot be reconciled completely with magnetic structures revealed by the earlier neutron diffraction results, unveil some distinct features of the magnetic ordering that were not disclosed before due to the unavailability of single crystal samples. We argue that the additional features of the second magnetic reordering found at lower temperatures along the a - and c -axis may have originated strain-induced lattice buckling and associated canting of Mn moments. It is anticipated that, by taking the refined magnetic structure and its anisotropic nature into account, the intriguing physics prevailing in these magnetism-induced multiferroics can be better understood. Direct measurements of magnetoelectric coupling along respective crystallographic axis to test the theoretical predictions are relying on successful film growth on suitable conductive substrates and will be the priority topics of future researches.

References

- [1] T. Kimura, S. Ishihara, H. Shintani, T. Arima, K.T. Takahashi, K. Ishizaka, Y. Tokura, *Physical Review B*. 68 (2003) 060403.
- [2] T. Goto, T. Kimura, G. Lawes, A.P. Ramirez, Y. Tokura, *Physical Review Letters*. 92 (2004) 257201.
- [3] M. Tachibana, T. Shimoyama, H. Kawaji, T. Atake, E. Takayama-Muromachi, *Physical Review B*. 75 (2007) 144425.
- [4] M.N. Iliev, M.V. Abrashev, H.G. Lee, V.N. Popov, Y.Y. Sun, C. Thomsen, R.L. Meng, C.W. Chu, *Physical Review B*. 57 (1998) 2872.
- [5] N. Hur, S. Park, P.A. Sharma, J.S. Ahn, S. Guha, S.W. Cheong, *Nature*. 429 (2004) 392.
- [6] H. Katsura, N. Nagaosa, A.V. Balatsky, *Physical Review Letters*. 95 (2005) 057205.
- [7] H. Katsura, A.V. Balatsky, N. Nagaosa, *Physical Review Letters*. 98 (2007) 027203.
- [8] M. Mostovoy, *Physical Review Letters*. 96 (2006) 067601.
- [9] I.A. Sergienko, C. Sen, E. Dagotto, *Physical Review Letters*. 97 (2006) 227204.
- [10] S. Picozzi, K. Yamauchi, B. Sanyal, I.A. Sergienko, E. Dagotto, *Physical Review Letters*. 99 (2007) 227201.
- [11] B. Lorenz, Y.Q. Wang, C.W. Chu, *Physical Review B*. 76 (2007) 104405.
- [12] B. Lorenz, Y.Q. Wang, Y.Y. Sun, C.W. Chu, *Physical Review B*. 70 (2004) 212412.
- [13] J. Kim, S. Jung, M.S. Park, S.I. Lee, H.D. Drew, H. Cheong, K.H. Kim, E.J. Choi, *Physical Review B*. 74 (2006) 052406.
- [14] X. Marti, V. Skumryev, V. Laukhin, F. Sanchez, M.V. Garcia-Cuenca, C. Ferrater, M. Varela, J. Fontcuberta, *Journal of Materials Research*. 22 (2007) 2096.
- [15] N. Fujimura, T. Ishida, T. Yoshimura, T. Ito, *Applied Physics Letters*. 69 (1996) 1011.
- [16] A. Munoz, J.A. Alonso, M.T. Casais, M.J. Martinez-Lope, J.L. Martinez, M.T. Fernandez-Diaz, *Journal of Physics-Condensed Matter*. 14 (2002) 3285.
- [17] A. Munoz, M.T. Casais, J.A. Alonso, M.J. Martinez-Lope, J.L. Martinez, M.T. Fernandez-Diaz, *Inorganic Chemistry*. 40 (2001) 1020-1028.
- [18] T.H. Lin, C.C. Hsieh, H.C. Shih, C.W. Luo, T.M. Uen, K.H. Wu, J.Y. Juang, J.Y. Lin, C.H. Hsu, S.J. Liu, *Applied Physics Letters*. 92 (2008) 132503.

- [19] P.A. Salvador, T.D. Doan, B. Mercey, B. Raveau, *Chemistry of Materials*. 10 (1998) 2592.
- [20] X. Marti, F. Sanchez, J. Fontcuberta, M.V. Garcia-Cuenca, C. Ferrater, M. Varela, *Journal of Applied Physics*. 99 (2006) 08p302.
- [21] T. Lonkai, D.G. Tomuta, U. Amann, J. Ihringer, R.W.A. Hendrikx, D.M. Tobbens, J.A. Mydosh, *Physical Review B*. 69 (2004) 134108.
- [22] Z.J. Huang, Y. Cao, Y.Y. Sun, Y.Y. Xue, C.W. Chu, *Physical Review B*. 56 (1997) 2623.
- [23] K.H. Wu, J.Y. Juang, C.L. Lee, T.C. Lai, T.M. Uen, Y.S. Gou, S.L. Tu, S.J. Yang, S.E. Hsu, *Physica C*. 195 (1992) 241.
- [24] S. Quezel, J. Rossat-Mignod, E.F. Bertraut, *Solid State Communication* 14 (1974) 941.



Chapter 6

Anisotropic electronic structure in hexagonal and orthorhombic structured YMnO₃ thin films

In the previous chapters, we have described how to stabilize the orthorhombic structure in RMnO₃ Group II compounds and how the magnetic ordering behaviors changed with the crystal structure changes. With the doping effect, larger A-site ions or smaller B-site ions tend to modify the MnO₅ bipyramids into MnO₆ octahedrons. On the other hand, suitable substrate can also provide tremendous strain force in stabilizing the hexagonal Group II RMnO₃ into the orthorhombic structure. In chapter 4 and 5, we have respectively investigated the anisotropic magnetic behaviors exhibited by the hexagonal and orthorhombic YMnO₃ thin films. According to the mechanism of the magnetism-induced polarization, the dipole moment was induced by the relative displacements of cations and anions (oxygen for ABO₃ structure) in the crystal structure. The relative displacements, in turn, are expected to induce variations in the bond angle and bond distance between positive and negative ions. Thus, there must be differences in the electronic structure when the system is either in the paraelectric or in the ferroelectric state. In this chapter, we will present anisotropic bonding behavior revealed in the x-ray absorption spectroscopy and try to establish the interrelations between the electronic structure, the Jahn-Teller distortion, and the mechanism of spin induced polarization.

6.1 Introduction

In recent years, perovskite manganites RMnO_3 ($R = \text{rare earth and Y}$) had been widely investigated owing to the rich and interesting physical properties involved in these materials [1-5]. Extensive researches have already indicated the intimate interplays involving spin, orbital and charge orderings in the hole-doped LaMnO_3 manganites in giving rise to the colossal magnetoresistance (CMR) [8-13]. With further reduced rare-earth ionic size, the RMnO_3 compounds have revealed even richer and interesting physical behaviors. For instance, with the ionic size reducing from 1.22\AA ($R = \text{La}$) to 0.94\AA ($R = \text{Lu}$) the magnetic phase diagram has implicated complicated competitions involving the Jahn-Teller distortion, ferromagnetic and antiferromagnetic interactions. Since, as already discussed in previous chapters, we have been able to prepare both the hexagonal and orthorhombic phases of the same Group II manganite thin films, we will focus on the electronic structure properties of these materials here. As pointed out by Filipetti and [7], the energy level diagram of RMnO_3 in cubic, orthorhombic, and hexagonal structure can be illustrated schematically as those shown in Fig. 6.1. The mechanism of energy level splitting

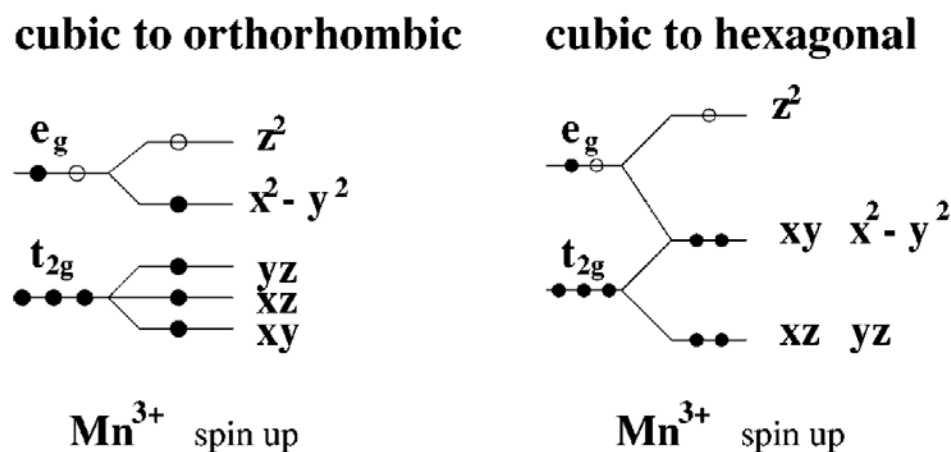


Figure 6.1: Schematic orbital splitting for the majority d states of Mn^{3+} ion within orthorhombic and hexagonal crystal field [7].

involves complicated crystal field and Jahn-Teller effect and the resultant effects in turn dominate the magnetic and ferroelectric behaviors of these compounds. In the group II RMnO₃ compounds, the MnO₆ structure originally favored in the perovskite structure is distorted and converted into MnO₅ in the AB stacking layer with the hexagonal structure. As a result, for YMnO₃, the Mn³⁺ and Y³⁺ ions are having the MnO₅ and YO₈ local structures with D_{3h} and D_{3d} symmetry, respectively [14].

On the other hand, the d⁴ electronic configuration of Mn³⁺ in LaMnO₃ compounds is denoted as e_g¹t_{2g}³, which as a first approximation is determined by using the Hund's rule. In these notations, e_g is a doublet state with higher energy level and t_{2g} is a lower energy triplet state. The two states are split by crystal field. At temperatures above the orbital ordering temperature, the Jahn-Teller distortion remains dynamic [11], and the orbital ordering temperature increases with the decreasing rare earth's ionic size (T = 747 K to ~1130 K for R = La to Nd) [1]. However, as the temperature is below the orbit ordering temperature, the orbital orders in the *a-b* plane as $3d_{3x^2-r^2}/3d_{3y^2-r^2}$ stagger with *Pbnm* space group [10, 11].

For the spin ordering, the in-plane orbital ordering leads the LaMnO₃ to exhibit ferromagnetic (FM) interaction within the *a-b* plane and antiferromagnetic (AFM) interaction along the *c*-axis, resulting in the so-called A-type AFM below the Néel temperature (T_N). With the decreasing of the ionic size of rare earth, the A-type AFM spin ordering behavior no longer is the stable ordering in the phase diagram. As can be seen in the phase diagram shown in Fig. 6.2, T_N decreases continuously with the decreasing ionic size of rare earth for R = La to Gd and the decreasing T_N was regarded as being influenced by the Jahn-Teller distortion [1]. For R = Eu and Gd which was different from LaMnO₃, the spin order enters an extra sinusoidal incommensurate magnetic ordering with a temperature dependent vector (0, *q*, 0) and

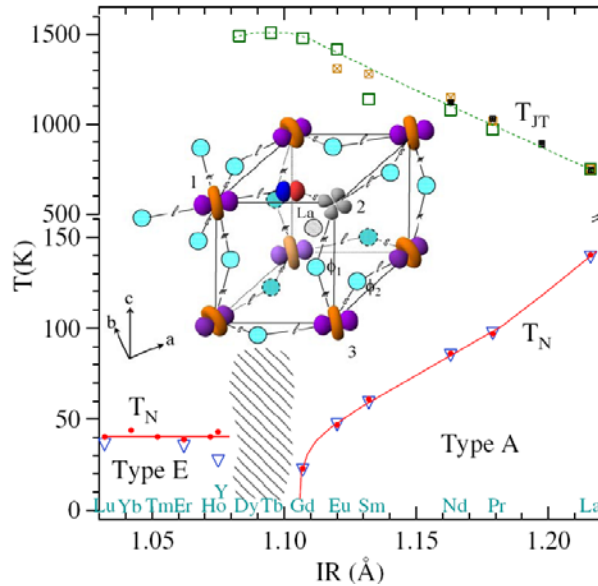


Figure 6.2: Transition temperatures versus R^{3+} -ion radius (IR) in the perovskite $RMnO_3$ family. The T_N values shown by solid circles were obtained from magnetization measurements in a magnetic field of 20 Oe. Open triangles mark the temperature where the thermal conductivity $\kappa(T)$ shows an anomaly. [4]

then exhibits A-type AFM orders with decreasing temperature. For smaller ions $R = Tb$ and Dy , a temperature dependent IC magnetic orders remains for higher q , and then the A-type magnetic orders was replaced by a spin spiral phase when the temperature is further decreased. The neutron diffraction data indeed showed that for $HoMnO_3$ the q value of the IC AFM spin orders increases gradually with decreasing temperature and then remains at $q = 0.5$ for temperature below the “lock-in” temperature ($T_L \approx 25$ K) and the magnetic ordering becomes as E-type AFM [15, 16]. For the remaining rare-earth elements with even relatively smaller ionic size (namely, $R = Er$ to Lu), the phase diagram constructed from temperature dependent heat capacity measurements indicated the similar IC-AFM followed by E-type AFM ordering magnetic structure changes upon cooling [4, 5]. These phenomena though seemed quite complicated but are believed to be markedly influenced by the Jahn–Teller distortions associated with coordination changes of Mn-O polyhedrons.

For instance, with decreasing ionic size of the rare-earth elements the Mn-O-Mn bond angle decreases from 155° (LaMnO₃) to 140° (LuMnO₃) and the Mn-O bond length also varies accordingly. Kimura et al. discussed these phenomena via the competition between nearest-neighbor (NN) FM interaction and next-nearest-neighbor (NNN) AFM interaction in the *a-b* plane for R = La to Ho. Zhou et al. pointed out the in-plane FM e_g-O-e_g and AFM t_{2g}-O-t_{2g} interactions play a much more important role than the NNN AFM interaction for R = Ho to Lu [4]. Finally, Tachibana et al. provide the detail relation between the NNN interaction and the Jahn-Teller distortion with various ionic sizes in RMnO₃ by synchrotron x-ray powder diffraction [5].

However, understanding the correlations between the electronic structure and the Jahn-Teller distortion is still an important topic. The Jahn-Teller distortion plays an important role in variation of Mn-O-Mn bond angle and Mn-O bond length in the MnO₆ perovskite structure. According to Tachibana et al., the variation of lattice constant and bond length by Jahn-Teller distortion can also be anisotropic along different crystalline axes of orthorhombic RMnO₃ [5]. This may also infer the anisotropic bonding behavior with small ionic size of rare earth in RMnO₃. Unfortunately the single crystal RMnO₃ (for R = Y and smaller rare earth Ho to Lu) with orthorhombic structure are not available at present and current results concerning the electronic structures of the orthorhombic RMnO₃ (with R = Y to Lu) are all obtained from samples fabricated via high temperature, high pressure synthesis [3, 17-20], thus there are still some outstanding issues remaining to be clarified. In this chapter, we use thin films with hexagonal and orthorhombic structure respectively grown on YSZ(111) and LAO(110) substrates to probe the anisotropic bonding behavior along each crystalline axis. The results will also be discussed in terms of how the crystal field and the Jahn-Teller effect act differently to give rise to the differences between the MnO₅ and MnO₆ electronic structures.

6.2 Experiment

The thin films discussed in this chapter were prepared by the same pulsed laser deposition processes described in Chapter 4 and 5. As has been discussed in detail previously, these films were all highly oriented epitaxial films with excellent crystalline quality both in-plane and out of plane. For hexagonal YMO films we used the YSZ(111) substrates, while the orthorhombic YMO films were mostly grown on the LAO(110) substrates. Indeed, the XRD Φ -scan data revealed the characteristic six-fold symmetry for the *h*-YMO(00 ℓ)/YSZ(111) films and two-fold symmetry for the *o*-YMO(020)/LAO(110) films, respectively. The magnetic behavior was probed by Quantum Design® superconducting quantum interference device (SQUID) and revealed distinct anisotropies in both hexagonal and orthorhombic structured thin films (*see* Chap. 4 & Chap. 5). Here, we will use the X-ray absorption near edge spectroscopy (XANES) to delineate the anisotropies in the electronic structure. The data are collected by both the fluorescence electron yield (FY) mode and total electron yield (TEY) mode with an energy resolution of ~ 0.15 eV. Nonlinear polarized X-ray of 90% polarization was also taken into consideration.

6.3 Results and Discussions

6.3.1 Electronic structure of the MnO_5 bipyramids in hexagonal YMnO_3 thin films

With the aids of polarized X-ray, we were able to use the linear polarized electric field to probe the electronic structure along each crystalline axis. Fig. 6.3(a) showed the Mn L edge spectra for $\text{LaMnO}_3(001)/\text{STO}(001)$ ($E//a-b$ plane) and $h\text{-YMO}/\text{YSZ}(111)$ ($E//a-b$ plane and $E//c$ -axis) thin films. The data of $\text{LaMnO}_3(001)/\text{STO}(001)$ thin came from the master thesis of L. C. Liu [21]. By comparing with LaMnO_3 and $h\text{-YMO}$, the data showed both Mn L_3 and L_2 peaks. It revealed different spectra in detail which was originated from the difference between octahedral MnO_6 and bipyramidal MnO_5 structure. To check the Mn L-edge spectra in distorted perovskite, we compared the patterns of single crystalline sample in the report of D. Y. Cho et al and shoed in Fig. 6.3(b). [14] Our spectra were similar to the report and showed alike to the theoretical calculation.

In Fig. 6.4, we probed the O-K edge XANES spectra of $E// a-b$ plane and c -axis of $h\text{-YMO}$ thin films. With the cubic to hexagonal splitting level in Fig. 6.1, we could available a singlet and two doublet energy level. In the report of D. Y. Cho, they used the polarization dependent spectra with hexagonal YMnO_3 single crystal to structuralized electronic structure of Mn-O and Y-O bonding of O K-edge. They also analyzed with cluster model calculation including the configuration interaction in theoretical. [14] In their assignment, there were first four leading features at the beginning O K-edge around 528~532 eV, they were attributed by $a_{1g}(z^2\uparrow)$, $e_{1g}(yz\downarrow/zx\downarrow)$, $e_{2g}(xy\downarrow/x^2-y^2\downarrow)$, and $a_{1g}(z^2\downarrow)$ with the increasing energy, and these bands

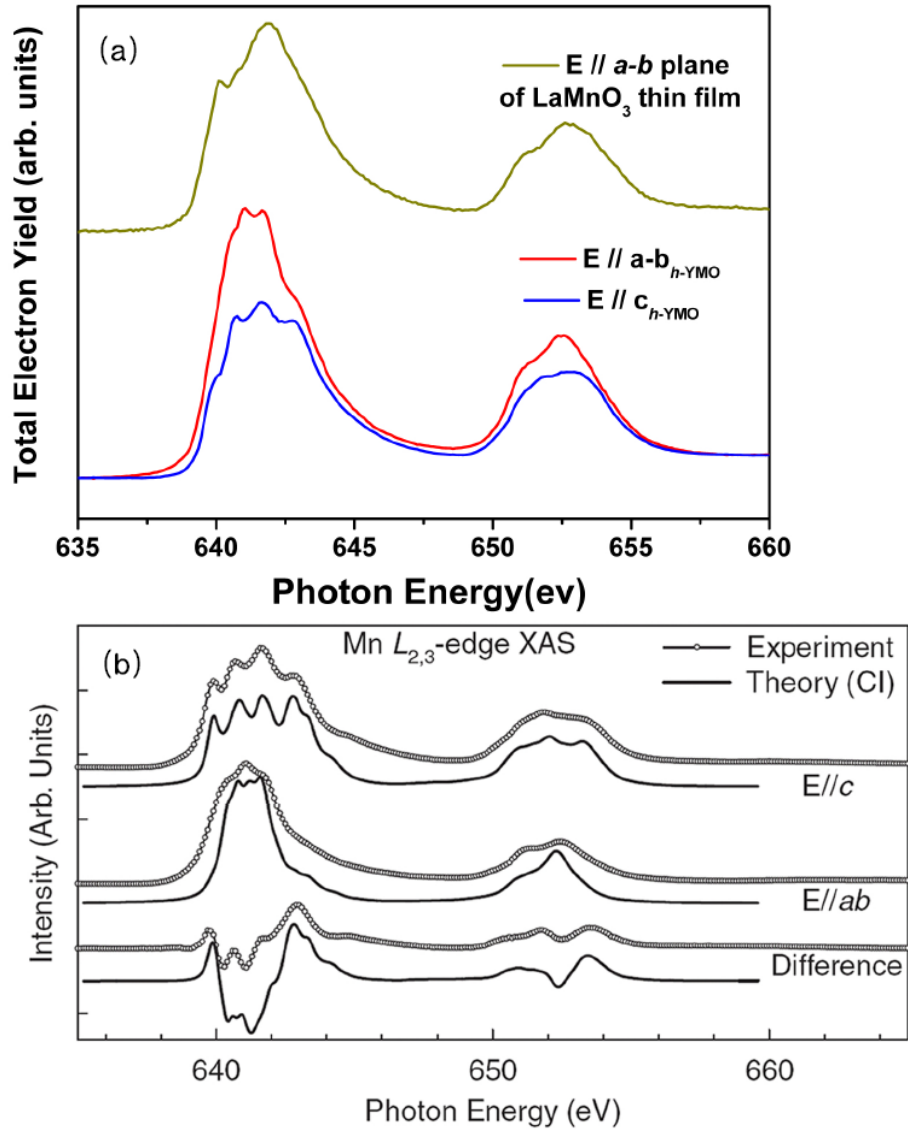


Figure 6.3: (a) The Mn L edge XANES spectra for LaMnO₃(001)/STO(001) and *h*-YMO(00 l)/YSZ(111) thin films from top to bottom. The thin film samples are measured with polarized X-ray and the electric field are parallel to the each crystalline axis. The data are collected with the relations E//*a-b* plane for LaMnO₃ thin film and E//*a-b* plane and E//*c*-axis for *h*-YMO thin film. (b) Reference data of single crystal YMnO₃ with hexagonal structure showed the polarized spectra E//*a-b* plane and E//*c*-axis. [13]

were ascribed to Mn 3d-O 2p hybridized states in MnO₅ bipyramidal structure. The followed three features around 532~539eV were ascribed to the contribution of Y 4d-O 2p hybridized states and they were assigned to a doublet e_g^π , singlet a_{1g} , and a doublet e_g^σ orbital. Finally, the features in the range of 539~548 eV were contributed

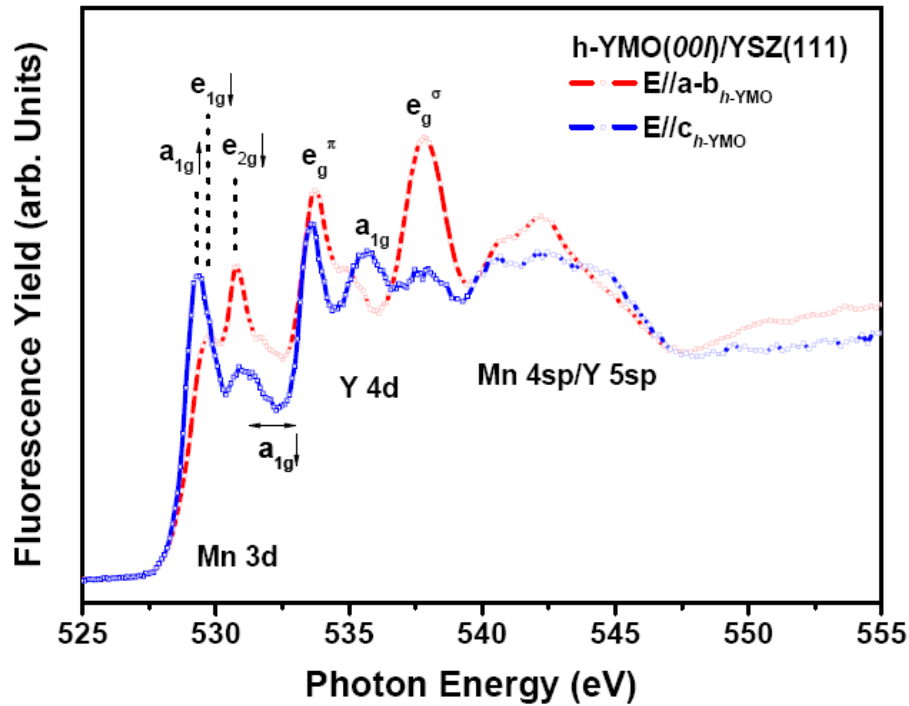


Figure 6.4: The O K edge XANES spectra for h -YMO(00 ℓ)/YSZ(111) thin film. The thin film samples are measured with polarized X-ray and the electric field are parallel to the each crystalline axis. The data are collected with the relations $E//a$ - b plane and $E//c$ -axis for h -YMO thin film.

by oxygen hybridized Mn 4sp/Y 5sp state. By comparison with our XANES spectra, it revealed similar behavior. It also showed the high quality which could compared to the single crystalline samples.

6.3.2 MnO_6 octahedral electronic structure in hexagonal YMnO_3 thin films

After the measurements of h -YMO thin films, we could find the polarization dependent spectra were sensitivity to the anisotropic electronic structure. But it was doubt whether the corrections at the last of the report. In the report, it showed the

nearly isotropic bonding behavior of LaMnO₃ and DyMnO₃ thin film with orthorhombic structures. It was well known that anisotropic behavior was originated from the Jahn-Teller distortion. With the ionic size variation of rare earth, the Mn-O bonding length and Mn-O-Mn bonding angle was changed with Jahn-Teller distortion. In the report of M. Tachibana, [6] the Mn-O bond distance in MnO₆ octahedrons were varied by Jahn-Teller effect. Fig. 6.5 showed the Mn-O bond distance had three different values: the larger one (l) and smaller one (s) in the a-b plane, and the medium one (m) was along the c-axis. The difference between the larger one and smaller one would be increased with the smaller ionic size of rare earth. With the further prepared thin film of o-YMO(020)/LAO(110), we could probe the anisotropic electronic structure with the powerful tool and realized the exactly splitting energy level in o-YMO compounds.

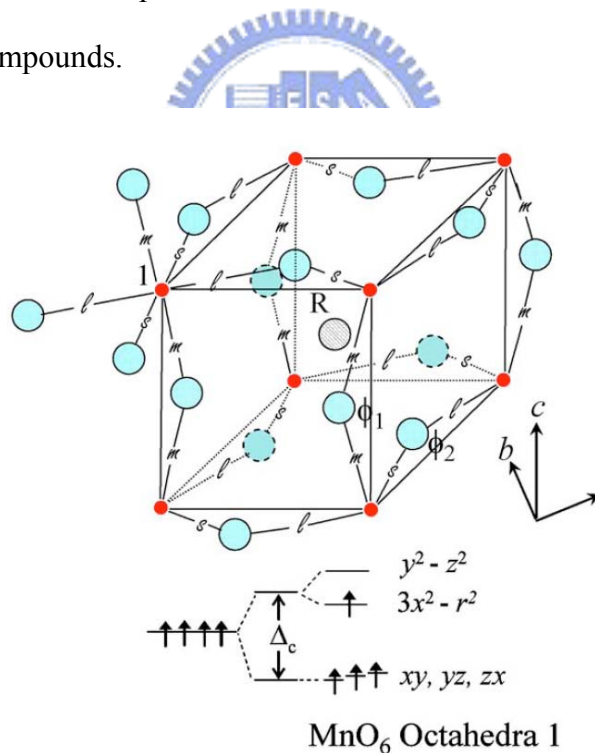


Figure 6.5: Schematic drawing of the crystal structure and the 3d orbitals in the MnO₆ octahedrons for orthorhombic RMnO₃. [6]

The Mn L edge XANES spectra of standard powders MnO, Mn₂O₃, and MnO₂ standard was showed in Fig. 6.6(a) and the data were showed with TEY mode. All of

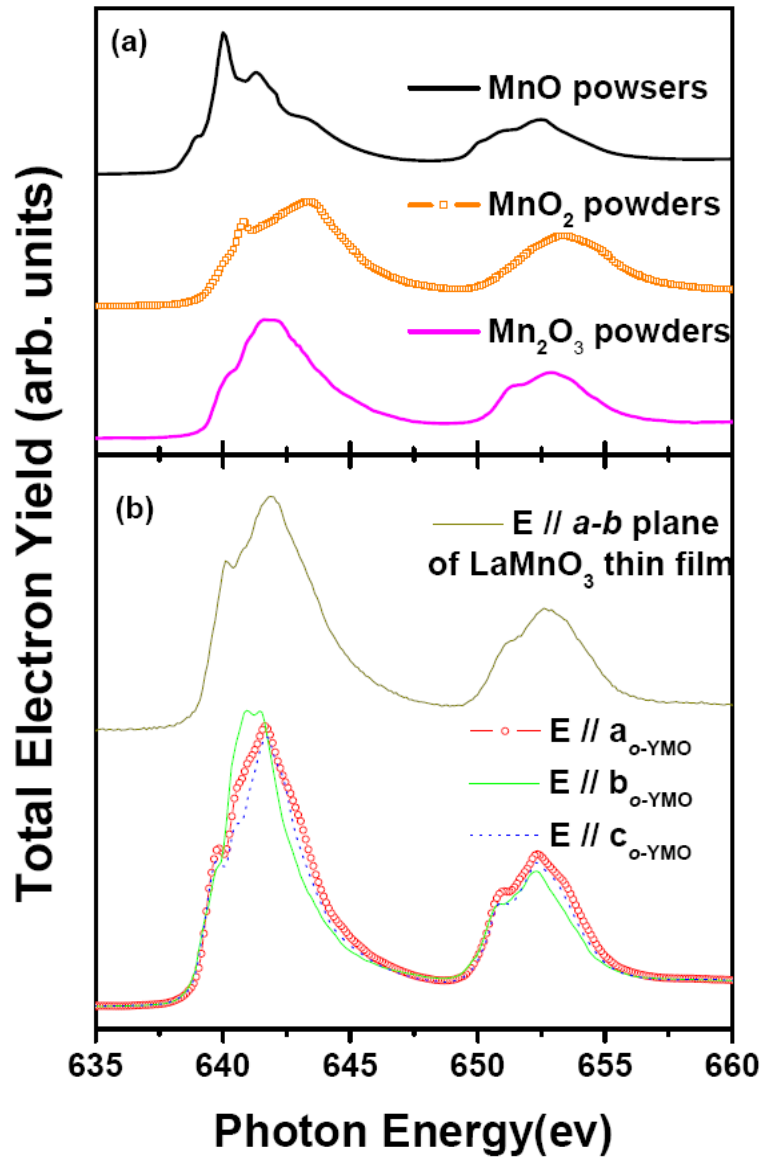


Figure 6.6: The Mn L edge XANES spectra for (a) MnO (standard powder), MnO₂ (standard powder), and Mn₂O₃ (standard powder) from top to bottom. (b) LaMnO₃(001)/STO(001) and *o*-YMO(020)/LAO(110) thin films from top to bottom. The thin film samples are measured with polarized X-ray and the electric field are parallel to the each crystalline axis. The data are collected with the relations E//*a-b* plane for LaMnO₃ thin film and E//*a*-axis, E//*b*-axis, and E//*c*-axis for *o*-YMO thin film.

these standard powders showed two broad multiplet L₂ and L₃ peak for the main behaviors, and the Mn-L₃ and Mn-L₂ located in the range of 640~650eV and 650~660eV which was separated by spin-orbital interaction respectively. There was a

little difference in the Mn-L₃ peak between these powders. By comparing with trivalent manganese, the main peak shifts to lower energy and thicker for the divalent manganese, it shifts to higher energy for the quadrivalent manganese. Owing to this scenario, we could easily clarify the valence in the RMnO₃ compounds. Fig. 6.6(b) showed Mn L edge XANES spectra for and thin film sample LaMnO₃(001)/STO(001) and o-YMO(020)/LAO(110) and it was probed with linear polarized x-ray. The electric field was set parallel to *a-b* plane in LaMnO₃ and E//*a*-axis, E//*b*-axis, and E//*c*-axis in o-YMO thin films. By comparison with the *a-b* plane in LaMnO₃ and similar partial weight (E//*a* and E//*b*) in o-YMO, we could find the Mn-L₃ peak shift to left about 0.3 eV and revealed sharper. When the electric field parallel to *c*-axis, there were two peaks at the top of Mn-L₃ and separated about 0.5 eV.

In the MnO₆ structure, the energy level diagram in perovskite structure was split into a high lying doublet e_g and low lying trialet t_{2g} with crystal field effect, and Jahn-Teller effect would split the energy level further. With the theoretical calculation

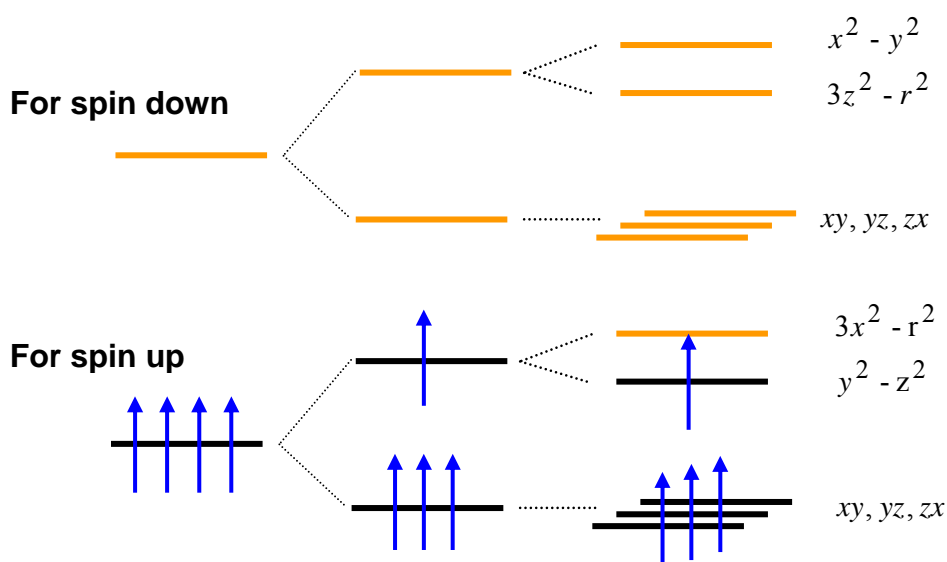


Figure 6.7: Schematic orbital splitting for the majority *d* states of Mn³⁺ ion within RMnO₃ and orange bars show the unoccupied state in MnO₆ structure. [22]

and XAS spectra in TbMnO_3 and DyMnO_3 , [22] the energy splitting level were different from the energy level splitting diagram in 6.1. The in-plane strong bonding anisotropy needs to be considered and the further energy level schematics show in Fig. 6.7. We probed the O-K edge XANES spectra of $E // a$ -axis, $E // b$ -axis and $E // c$ -axis

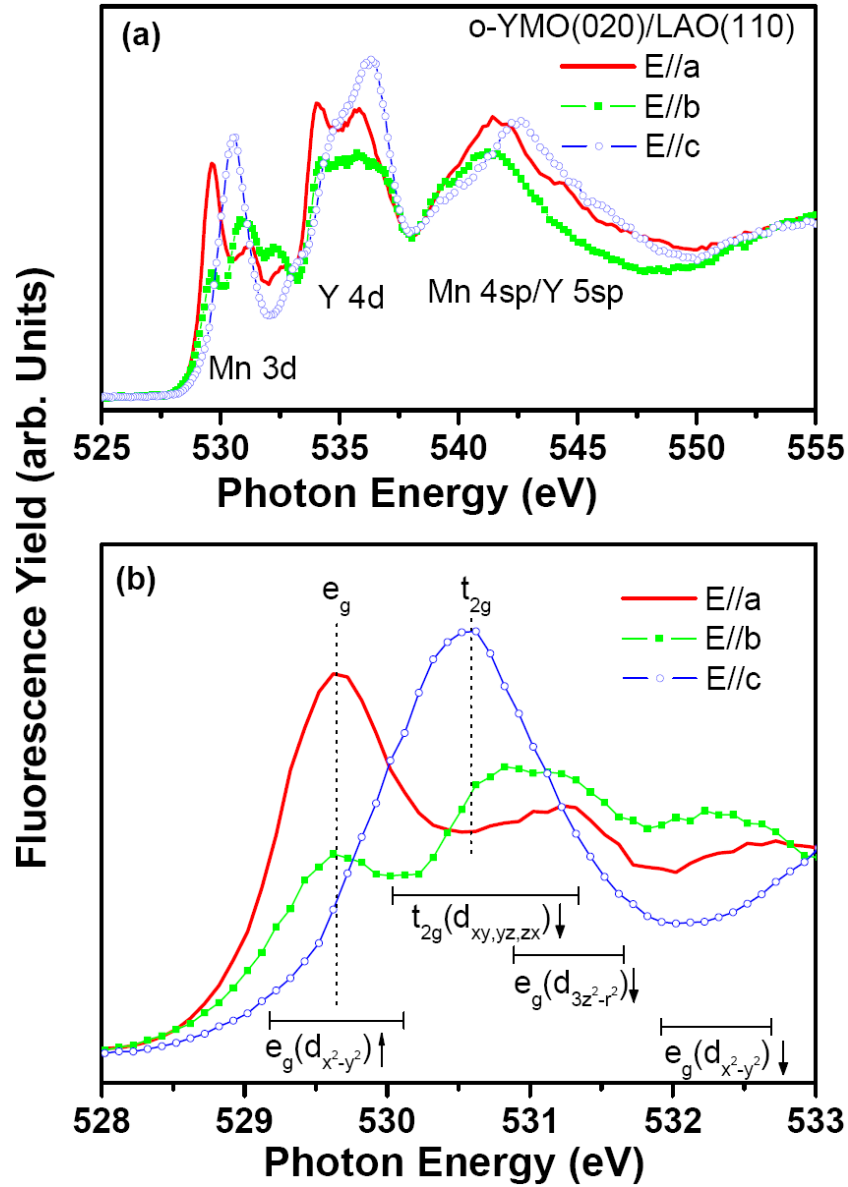


Figure 6.8: The O K edge XANES spectra for o -YMO(00ℓ)/LAO(110) thin film. The thin film samples are measured with polarized X-ray and the electric field are parallel to the each crystalline axis. The data are collected with the relations $E//a$ -axis, $E//b$ -axis, and $E//c$ -axis for o -YMO thin film. (a) Diagram of the full range O K edge spectra, (b) Diagram of O-2p and Mn-3d rehybridization range O K edge spectra

c-axis of o-YMO thin films and showed similar behaviors in Fig. 6.8. S. Picozzi et al. [23] reported the band structure of o-YMO with the first principle calculation in considering the o-YMO as a AFM-E type ordering. It showed an energy splitting about 2~3 eV above Fermi level. By considering the calculation with the report of J. M. Chen, [22] they used the single crystalline sample for TbMnO₃ and DyMnO₃ with orthorhombic structure and probed the anisotropic bonding behaviors. They also derive the density of state with LDA+U calculation. With the similarity of TbMnO₃ and DyMnO₃ and YMnO₃ with orthorhombic structure, we could also realize the characteristics in O K edge spectra of our o-YMO thin film. In Fig. 6.8(a), the spectra could divide into three parts of the spectra. The first leading group of O K edge around 528~533 eV was contributed by the rehybridization between Mn³⁺ and O²⁻ ions. The followed features around 532~539eV were ascribed to the contribution of Y 4d-O 2p hybridized states. Finally, the features in the range of 539~548 eV were contributed by oxygen hybridized Mn 4sp/Y 5sp state. We would focus on the Mn-3d O-2p hybridized region showed in Fig. 6.8(b) which played the key role in magnetic orders and magnetoelectric effect. For O 1s core hole in the first leading group of O K edge around 528~533 eV, it could be assigned as $e_g \uparrow (3d_{3x^2-r^2})$, $t_{2g} \downarrow (3d_{xy,yz,zx})$, $e_g \downarrow (3d_{3z^2-r^2})$, and $e_g \downarrow (3d_{x^2-y^2})$, and it was contributed by the rehybridization between Mn³⁺ and O²⁻ ions. Both the magnetic behavior and electronic structure both showed anisotropy along each crystalline axis. The Jahn-Teller effect affects the magnetic orders through in-plane e_g -O- e_g and t_{2g} -O- t_{2g} orbital.

Finally, the polarized spectra strongly showed the anisotropic bonding behavior in o-YMO thin films but it still couldn't give us the direct evidence of spin induced polarizations. Go back to consider the E-type magnetic orders in Fig. 6.9. In the report of I. A. Sergienko, [24] they pointed out that the polarization was induced by the

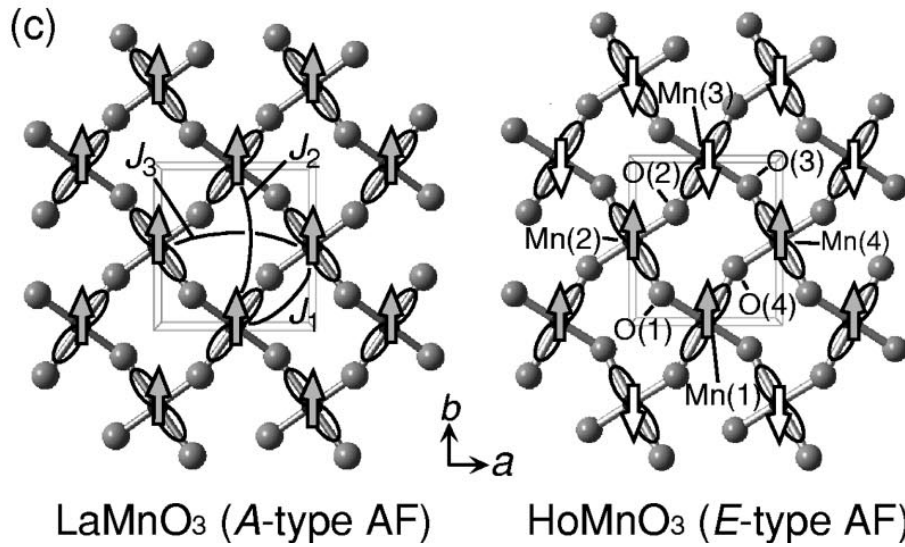


Figure 6.9: Crystal structures of LaMnO₃ and HoMnO₃. Spin (arrows) and orbital (lobes) ordered features are also illustrated. The stack of spin and orbital order along the *c* axis is staggered and uniform order, respectively, for both the compounds.

competence of in-plane elastic energy and hopping energy in Fig. 1.7. The elastic energy remains the same and the hopping energy decreases in the E-type spin orders. The Mn-O-Mn bond angle (Mn(2)-O(1)-Mn(1) and Mn(1)-O(4)-Mn(4)) would increase along a-axis in the FM zigzag chain below the lock-in transition temperature. With these scenario, the bond distance of (*s*) and (*ℓ*) showed in Fig. 6.4 would shorten with the increasing Mn-O-Mn bond angle along the FM zigzag chain. The energy level of $e_g(3d_{3x^2-r^2})$ configuration would increase with Jahn-Teller effect and the XANES spectra of E//a would reveal spectral weight shift to higher at room temperature in the lock-in transition state.

6.4 Summary

Thin films of h-YMO(00ℓ)/YSZ(111) and o-YMO(020)/LAO(110) were used in probing the detail electronic structure and anisotropic bonding behaviors in both

hexagonal and orthorhombic structure. The electronic structure appears to be dominated by the differences between MnO_5 bipyramids and MnO_6 octahedrons. Polarization dependent behaviors are observed with electric field parallel each crystalline axis in both hexagonal and orthorhombic structures. The polarized O K edge and Mn L edge x-ray absorption spectra reveal strong polarization dependent characteristics. It has been known that the magnetic and spin induced polarization was affected by Jahn-Teller effect and induced variation of Mn-O bond distance and Mn-O-Mn bond angle. We also estimated the spectral shift along a-axis in the magnetoelectric states.



References

- [1] T. Kimura, S. Ishihara, H. Shintani, T. Arima, K.T. Takahashi, K. Ishizaka, Y. Tokura, *Physical Review B*. 68 (2003) 060403.
- [2] T. Goto, T. Kimura, G. Lawes, A.P. Ramirez, Y. Tokura, *Physical Review Letters*. 92 (2004) 257201.
- [3] W. Prellier, M.P. Singh, P. Murugavel, *Journal of Physics-Condensed Matter*. 17 (2005) R803.
- [4] J.S. Zhou, J.B. Goodenough, *Physical Review Letters*. 96 (2006) 247202.
- [5] M. Tachibana, T. Shimoyama, H. Kawaji, T. Atake, E. Takayama-Muromachi, *Physical Review B*. 75 (2007) 144425.
- [6] J.S. Zhou, J.B. Goodenough, J.M. Gallardo-Amores, E. Moran, M.A. Alario-Franco, R. Caudillo, *Physical Review B*. 74 (2006) 014422.
- [7] A. Filippetti, N.A. Hill, *Physical Review B*. 65 (2002) 195120.
- [8] T. Mizokawa, A. Fujimori, *Physical Review B*. 51 (1995) 12880.
- [9] S. Ishihara, J. Inoue, S. Maekawa, *Physical Review B*. 55 (1997) 8280.
- [10] Y. Murakami, J.P. Hill, D. Gibbs, M. Blume, I. Koyama, M. Tanaka, H. Kawata, T. Arima, Y. Tokura, K. Hirota, Y. Endoh, *Physical Review Letters*. 81 (1998) 582.
- [11] M.C. Sánchez, G. Subías, J. García, J. Blasco, *Physical Review Letters*. 90 (2003) 045503.
- [12] S.F. Chen, W.J. Chang, C.C. Hsieh, S.J. Liu, J.Y. Juang, K.H. Wu, T.M. Uen, J.Y. Lin, Y.S. Gou, *Journal of Applied Physics*. 100 (2006) 113906.
- [13] W.J. Chang, C.C. Hsieh, J.Y. Juang, K.H. Wu, T.M. Uen, Y.S. Gou, C.H. Hsu, J.Y. Lin, *Journal of Applied Physics*. 96 (2004) 4357-4361.
- [14] D.Y. Cho, J.Y. Kim, B.G. Park, K.J. Rho, J.H. Park, H.J. Noh, B.J. Kim, S.J. Oh, H.M. Park, J.S. Ahn, H. Ishibashi, S.W. Cheong, J.H. Lee, P. Murugavel, T.W. Noh, A. Tanaka, T. Jo, *Physical Review Letters*. 98 (2007) 217601.

- [15] J.A. Alonso, M.J. Martinez-Lope, M.T. Casais, M.T. Fernandez-Diaz, *Inorganic Chemistry*. 39 (2000) 917-923.
- [16] A. Munoz, J.A. Alonso, M.T. Casais, M.J. Martinez-Lope, J.L. Martinez, M.T. Fernandez, *Journal of Alloys and Compounds*. 323 (2001) 486-489.
- [17] M.N. Iliev, M.V. Abrashev, H.G. Lee, V.N. Popov, Y.Y. Sun, C. Thomsen, R.L. Meng, C.W. Chu, *Physical Review B*. 57 (1998) 2872.
- [18] B. Lorenz, Y.Q. Wang, Y.Y. Sun, C.W. Chu, *Physical Review B*. 70 (2004) 212412.
- [19] J. Kim, S. Jung, M.S. Park, S.I. Lee, H.D. Drew, H. Cheong, K.H. Kim, E.J. Choi, *Physical Review B*. 74 (2006) 052406.
- [20] B. Lorenz, Y.Q. Wang, C.W. Chu, *Physical Review B*. 76 (2007) 104405.
- [21] L.-C. Liu, The surface and bulk electronic structure of CMR manganites, National Chiao Tung University, Hsinchu, master thesis 2004.
- [22] J.M. Chen, J.M. Lee, S.W. Huang, H.T. Jeng, C.K. Chen, C.C. Shen, I. Jarrige, Y. Cai, K.T. Lu, J.Y. Lin, T.J. Yang, R.S. Liu, K.S. Liang, Z. Hu, private communication (2008).
- [23] S. Picozzi, K. Yamauchi, G. Bihlmayer, S. Blugel, *Physical Review B*. 74 (2006) 094402.
- [24] I.A. Sergienko, C. Sen, E. Dagotto, *Physical Review Letters*. 97 (2006) 227204.

Chapter 7

Summary and future work

7.1 Summary

In this dissertation, we have used two methods to stabilize the Group II RMnO₃ compounds in the form of orthorhombic structure, which would be otherwise thermodynamically favorable to form the hexagonal structure. The inner strain originated from substituting ions with different size and the epitaxial strain resulted from the lattice mismatch between film and substrate is believed to play the key role in stabilizing an otherwise unfavorable crystalline structure.

A series of doped multiferroic samples Y_{1-x}A_xMnO₃ (A = Ca, Sr; x = 0, 0.1, 0.3, 0.5) were prepared by solid state reactions. It was found that, for the Y_{1-x}Ca_xMnO₃ (x = 0, 0.1, 0.3, 0.5) series, the crystal structure evolved from hexagonal to orthorhombic structure with increasing x, while for Y_{1-x}Sr_xMnO₃ (x = 0, 0.1, 0.3, 0.5) it remained hexagonal for all doping levels. For the Ca-doped samples, the antiferromagnetic (AFM) phase transition appears to take place at a much lower temperature (30.4 K) as compared to that of the undoped one (42.5 K). On the other hand, when doped with larger Sr-ions, the AFM temperature decreased only slightly to 38 K. Nevertheless, the AFM transition was significantly smeared, indicating that strain may have come into play. The x-ray absorption spectra of the YMnO₃ powders exhibit the dominant Mn³⁺ characteristics similar to that obtained from the standard Mn₂O₃ powder. With the increasing doping level of Ca and Sr, the Mn³⁺/Mn⁴⁺ mixed valence was observed in Mn L edge spectra. It was quite interesting in Ca-doped samples the O K edge spectra

revealed MnO_6 octahedral electronic structure which was drastically different from that of the MnO_5 bipyramids. High quality and highly orientated hexagonal $\text{YMnO}_3(00\ell)$ thin films were obtained by pulsed laser deposition on $\text{YSZ}(111)$ substrates. The in-plane arrangement obtained from the XRD Φ -scan patterns is consistent with the expected correspondences. The films also exhibited six-fold symmetry and confirmed the hexagonal structured characteristics. The thin film revealed an AFM transition around 70K and an additional spinglass-like behavior occurred at 40K.

Orthorhombic YMnO_3 thin films with (200)-, (020)-, and (001)-orientations were respectively obtained by pulsed laser deposition on $\text{SrTiO}_3(110)$, $\text{LaAlO}_3(110)$ and $\text{SrTiO}_3(001)$ substrates. The results demonstrate that the strain between film and substrate can serve as an alternative in transforming the thermodynamically stable hexagonal YMnO_3 into the orthorhombic phase, which previously could only be obtained with high-pressure and high temperature syntheses. More importantly, these films allow us, for the first time, to unambiguously disclose the intrinsic magnetic property along different crystallographic orientations. Our results show that, although the antiferromagnetic ordering remains the same, there is an additional spin reordering transition which is very much dependent on the crystallographic orientation along which the measuring field was applied and on the in-plane crystallographic alignment of the films. Detailed analyses indicate that the origin of the observed second reordering may be due to some strain-induced canted AFM state instead of the incommensurated lock-in transition conceived previously. The x-ray absorption near edge spectroscopy exhibited the strongly anisotropic bonding relation along each crystalline axis in both hexagonal and orthorhombic structure, indicating the characteristics of strong orbital-ordering of these materials. Between these different structures, the electronic structure was dominated by the difference between MnO_5 bipyramids and MnO_6 octahedrons. Polarization dependent behaviors are observed with electric field parallel each crystalline axis

in both hexagonal and orthorhombic structures.

7.2 Future work

Based on the success in stabilizing specific structures with the in-plane strain, we compare in Fig. 7.1 the in-plane mismatch between the commonly used single crystalline perovskite substrates and the orthorhombic $RMnO_3$ compounds. It is evident that LAO substrate is a more suitable choice in sustaining the structure of the orthorhombic $RMnO_3$ than STO substrate. The mismatch between the LAO(110) substrate provides enough strain and the in-plane alignment to give rise to the orientation-specific o - $RMnO_3$ films. We have successfully deposited orthorhombic $RMnO_3$ (with $R = Y$ and $Ho^{[18]}$) thin films on LAO and

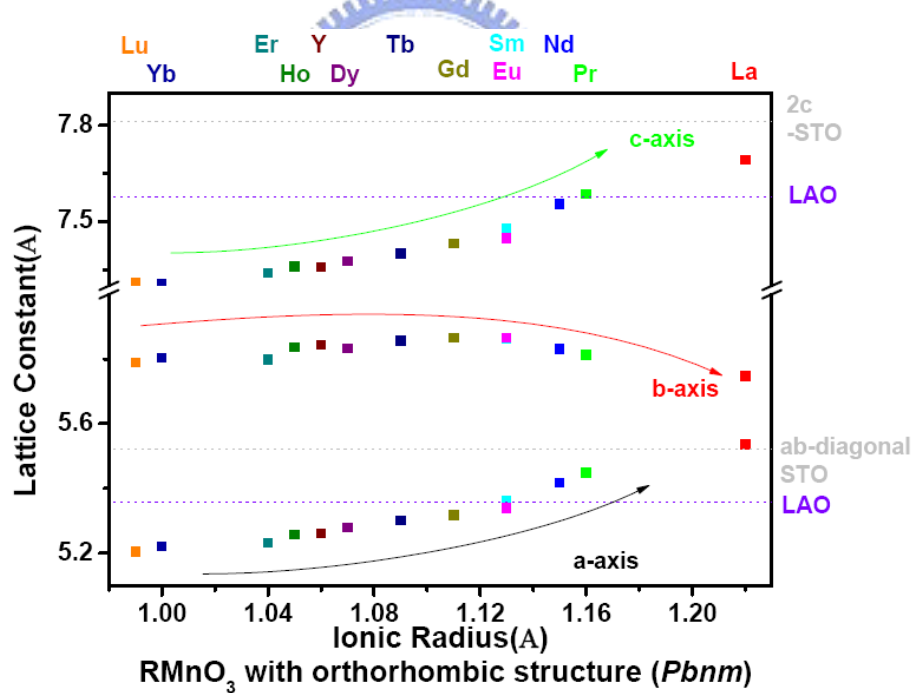


Figure 7.1: Summary of the in-plane mismatch between the orthorhombic $RMnO_3$ with $Pbnm$ space group setting and the two commonly used perovskite substrates.

Notice the tendency that $d_a/\sqrt{2}$, $d_b/\sqrt{2}$, and $d_c/2$ become equal gradually with the increasing ionic size to La^{+3} (1.22 Å) for the idealized pseudo cubic settings.

STO substrates. We anticipate that for ionic size smaller than Ho such as Eu, Yb, Lu can also be grown on these substrates with similar method described in this thesis. Since it is almost impossible to synthesize the single crystals of orthorhombic $RMnO_3$ compounds with R smaller than Y, the present method should serve as a plausible alternative to delineate the magnetic anisotropy which is the key to understand the magnetoelastic coupling and associated ferroelectric polarization in these so-called spin spiral or *E*-type improper multiferroic materials. Furthermore, in order to directly access the magnetism-induced polarization in *E*-type magnetic structures, conductive substrates with appropriate in-plane mismatch strain should play an important role.



Biographical notes

Personal Data:

Name: Hsieh, Chih-Chang

Sex: Male

Date of Birth: April 13, 1976

Education:

1995/09 ~ 1999/07 National Sun Yat-Sen University, Kaohsiung, Taiwan BS. degree in
Electrophysics.

1999/09 ~ 2001/07 National Chiao-Tung University, Hsinchu, Taiwan MS. degree in
Electrophysics.

2001/09 ~ 2008/07 National Chiao-Tung University, Hsinchu, Taiwan Ph. D degree in
Electrophysics.



Publication List:

1. Hsieh CC, Lin TH, Shih HC, Hsu C-H, Luo CW, Lin J-YW, K. H., Uen TM, Juang JY: **Magnetic ordering anisotropy in epitaxial orthorhombic multiferroic YMnO₃ films.** *Revised with Journal of Applied Physics* 2008.
2. Lin TH, Hsieh CC, Shih HC, Luo CW, Uen TM, Wu KH, Juang JY, Lin JY, Hsu CH, Liu SJ: **Anomalous magnetic ordering in b-axis-oriented orthorhombic HoMnO₃ thin films.** *Applied Physics Letters* 2008, **92**(13):132503.
3. Shih HC, Lin TH, Hsieh CC, Luo CW, Lin J-Y, Her JL, Yang HD, Hsu C-H, Wu KH, Uen TM *et al*: **Strain-induced canted antiferromagnetic ordering and magnetocapacitance in orthorhombic HoMnO₃ thin films.** *submit to Journal of Physics-Condensed Matter* 2008.

4. Chang WJ, Hsieh CC, Chung TY, Hsu SY, Wu KH, Uen TM, Lin JY, Lin JJ, Hsu CH, Kuo YK *et al*: **Fabrication and low temperature thermoelectric properties of Na_xCoO_2 ($x=0.68$ and 0.75) epitaxial films by the reactive solid-phase epitaxy.** *Applied Physics Letters* 2007, **90**(6):061917.
5. Luo CW, Hsieh CC, Chen YJ, Shih PT, Chen MH, Wu KH, Juang JY, Lin JY, Uen TM, Gou YS: **Spatial dichotomy of quasiparticle dynamics in underdoped thin-film $\text{YBa}_2\text{Cu}_3\text{O}_{7-\delta}$ superconductors.** *Physical Review B* 2006, **74**(18):184525.
6. Chen SF, Chang WJ, Hsieh CC, Liu SJ, Juang JY, Wu KH, Uen TM, Lin JY, Gou YS: **Anisotropic magnetoresistance of $\text{La}_{0.7}\text{Ca}_{0.3}\text{MnO}_3$ thin film biepitaxial step junctions.** *Journal of Applied Physics* 2006, **100**(11):113906.
7. Wang TC, Lee JY, Hsieh CC, Juang JY, Wu KH, Uen TM, Gou YS: **Activated kinetics of room-temperature-deposited SrTiO_3 thin films investigated by reflection-high-energy-electron-diffraction-monitored annealing at different heating rates.** *Japanese Journal of Applied Physics Part 1-Regular Papers Brief Communications & Review Papers* 2005, **44**(2):1067-1068.
8. Cheng TY, Hsieh CC, Juang JY, Lin JY, Wu KH, Uen TM, Gou YS, Hsu CH: **The magneto-transport properties of epitaxial $\text{La}_{0.7}\text{Sn}_{0.3}\text{MnO}_3$ manganite thin films.** *Physica B-Condensed Matter* 2005, **365**(1-4):141-146.
9. Wang TC, Lee JY, Hsieh CC, Juang JY, Wu KH, Uen TM, Gou YS: **RHEED in-situ monitored step edge diffusion during interrupted laser ablation epitaxy growth of SrTiO_3 .** *Chinese Journal of Physics* 2004, **42**(6):710-716.
10. Chang WJ, Hsieh CC, Juang JY, Wu KH, Uen TM, Gou YS, Hsu CH, Lin JY: **Effects of compressive epitaxial strain on the magnetotransport properties of single-phase electron-doped $\text{La}_{0.7}\text{Ce}_{0.3}\text{MnO}_3$ films.** *Journal of Applied Physics* 2004, **96**(8):4357-4361.
11. Hsieh CC, Wu KH, Juang JY, Uen TM, Lin JY, Gou YS: **Monophasic TiO_2 films deposited on $\text{SrTiO}_3(100)$ by pulsed laser ablation.** *Journal of Applied Physics* 2002, **92**(5):2518-2523.

12. Wu KH, Lin PI, Hsieh CC, Liu SJ, Juang JY, Uen TM, Lin JY, Gou YS:
Superconducting YBa₂Cu₃O₇ films grown on TiO₂ buffer layers derived from various processes. *Physica C* 2001, **363**(2):119-129.
13. Lin PL, Liu CW, Hsieh CC, Wu KH, Juang JY, Uen TM, Lin JY, Gou YS:
Characteristics of YBa₂Cu₃O₇ thin films deposited on substrates buffered by various TiO₂ layers. *Japanese Journal of Applied Physics Part 2-Letters* 2001, **40**(4B):L377-L379.

